

MARIANA BENITES

Morphology and chemical composition of polymetallic nodules from the Clarion-Clippertone Zone, the Indian Ocean and Rio Grande Rise, a comparative study

Thesis submitted to *Instituto Oceanográfico, Universidade de São Paulo*, in partial fulfilment of the requirements for the degree of Master of Sciences in Oceanography, with emphasis in Geological Oceanography.

Advisor: Prof. Dr. Luigi Jovane

Sao Paulo

2017

Benites, Mariana

B415m Morphology and chemical composition of polymetallic nodules from the Clarion-Clippertone Zone, the Indian Ocean and Rio Grande Rise, a comparative study / Mariana Benites. - 2017

89 f. ; 31 cm

Thesis (Master) – Instituto Oceanográfico at Universidade de São Paulo.

Advisor : Prof. Dr. Luigi Jovane

1. Polymetallic nodules 2. Morphology 3. Geochemistry 4. Genesis of nodules I. Jovane, Luigi (advisor) . Title.

UNIVERSIDADE DE SÃO PAULO
INSTITUTO OCEANOGRÁFICO

Morphology and chemical composition of polymetallic nodules from the
Clarion-Clipperton Zone, the Indian Ocean and Rio Grande Rise, a comparative
study

Reviewed Version

By

Mariana Benites

Thesis submitted to *Instituto Oceanográfico, Universidade de São Paulo*, in
partial fulfillment of the requirements for the degree of Master of Sciences in
Oceanography, with emphasis in Geological Oceanography.

Evaluated in ___/___/_____

Prof. Dr.

Grade

Prof. Dr.

Grade

Prof. Dr.

Grade

ACKNOWLEDGEMENTS

This work was only viable due to the kind efforts from researchers Bramley Murton (NOC, Southampton, UK) and Bejugam Nagender Nath (NIO, Goa, India) in sending the nodules samples to Sao Paulo. In addition, I thank Professor Paulo Sumida (IO-USP) for giving us the single sample from the Rio Grande Rise. FAPESP is acknowledged for financial support through project “Marine Ferromanganese Deposits, a Major Resource of E-Tech Elements” (2014/50820-7). I also thank CAPES for financial support via scholarship.

I wouldn't be able to conduct this work without the expertise from Jim Hein (USGS, Santa Cruz, USA) and Bram Murton who gave us many insights to delineate the investigation.

I cannot be thankful enough to Bramley by enabling my participation at the cruise JC142 and by assisting my visit to the NOC even being so occupied. I am thankful to Christopher Pearce and Amaya Menendez by making it possible to run LA-ICP-MS analyses at the NOC and assisting me with logistical and practical aspects. I also thank Andy Milton by helpful assistance running the analyses.

Of fundamental importance was the support from many technicians whose specialized knowledge contributed for the quality of this work. Daniel Uliana and Renato Contessoto from the LCT Poli-USP for the CT tomography scans; Paulinho from IGc-USP for the thin sections preparation; Jordana Zampelli from LabPetro IGc-USP for the microscope photos; Isaac Sayeg from LabMEV IGc-USP for SEM analyses; Carlos Perez and Douglas Galante from the XRF beamline at the Synchrotron laboratory (LNLS) for the XRF experiments; and Francesco Iacoviello (UCL, London, UK) by receiving me at London and insistent tests on the tomography data segmentation.

Special thanks to the IO-USP library staff Wagner Pinheiro for help with bibliographical tools and standards. Also, to the post-graduation office staff Ana Paula, Letícia and Daniel for so many helps.

This journey would be solitary without the lab colleagues Celine, Eric, Igor, Simone, Flaminia and Martino. To Daniel Rodelli and Patricia Cedraz I thank for sleep hours robbed in favour of my experiment at LNLS. Mascimiliano Maly and Natascha Bergo special thanks for being part of all my 45 days at the Cook.

I am thankful to Christian Millo for incomparable dedication on a not formal co-supervision whose tireless disposition in teaching and learning with me about a new study field was so important for my personal development.

Finally, all my Master degree experience would never be a possibility without the enthusiasm and trust of my supervisor Luigi Jovane, to who I owe incessant motivation and endless patience.

From now, I would like to address a few personal thanks in my maternal language.

Nesses quase dois anos e meio de empreitada, foram muitos os abraços amigos que me ajudaram a manter positiva e confiante a despeito das dificuldades. Crucial presença intermitente de pessoas tão queridas ao meu redor. Aos meus velhos amigos do IO, agradeço por encontrar sempre sorrisos e abraços familiares e por manterem este prédio um lugar aconchegante. Aos amigos da pós do IGc agradeço por me adotarem (uma oceanógrafa no ninho!) e se tornarem minha outra família na USP, por passar este momento de conclusão do mestrado e incertezas do futuro de tão perto, e por fazerem este lugar me ser tão receptivo (e divertido!). Por fim, à galera da LiGEA, por trazerem tanta coisa nova na minha vida, renovando as energias para seguir e concluir este trabalho.

Não podia deixar de dedicar esta vitória a ela, pois sei que o meu sentimento de sucesso vale no coração dela três vezes mais.

Por fim, agradeço ao que existe de mais sutil e etéreo por acreditar.

'It is a queer thing, but imaginary troubles are harder to bear than actual ones.'

Dorothea Dix

*'Mesmo quando tudo parece desabar,
Cabe a mim decidir entre rir ou chorar,
Ir ou ficar, desistir ou lutar;
Por que descobri, no caminho incerto da vida,
Que o mais importante é o decidir.'*

Cora Coralina

RESUMO

BENITES, Mariana. **Morphology and chemical composition of polymetallic nodules from the Clarion-Clippertone Zone, the Indian Ocean and Rio Grande Rise, a comparative study.** 2017. 94 p. Dissertação (Mestrado) – Instituto Oceanográfico, Universidade de São Paulo, São Paulo, 2017.

Nódulos polimetálicos de mar profundo são concreções de óxidos de manganês e de ferro ao redor de um núcleo. Os nódulos crescem através da precipitação hidrogenética – precipitação de metais da água do mar – ou diagenética – precipitação de metais da água intersticial do sedimento. O processo de acreção reflete na morfologia e geoquímica dos nódulos. Neste trabalho, quatorze nódulos polimetálicos provenientes de quatro regiões oceânicas – Clarion-Clippertone Zone (Oceano Pacífico Nordeste), Bacia Central do Índico (Oceano Índico Central), Bacia Mascarene (Oceano Índico Oeste) e Elevação de Rio Grande (Oceano Atlântico Sudoeste) – foram usados a fim de se comparar os aspectos morfológicos e geoquímicos dos nódulos entre regiões diferentes. A estrutura interna dos nódulos foi avaliada através da Tomografia Computadorizada por Raios-X (CT). Microscopia Eletrônica de Varredura (SEM) foi usada para descrever as micro camadas. A composição química foi determinada por Micro Fluorescência de Raios-X (μ -XRF) e por ablação a laser acoplada a espectrometria de massa com plasma indutivamente acoplado (LA-ICP-MS). Por fim, a Espectroscopia de Absorção de Raios-X próximo à borda (XANES) foi realizada a fim de se determinar a especiação (i.e., o número de oxidação) do Mn e do Fe. Os nódulos polimetálicos da Bacia Central do Índico são diagenéticos e os da Bacia Mascarene e Elevação do Rio Grande são hidrogênicos, enquanto que os da Clarion-Clippertone Zone são do tipo misto. Entretanto, o processo de acreção varia ao longo dos nódulos, resultando em textura das camadas e composição química heterogênea. Forte fracionamento entre Mn e Fe ocorre nos nódulos diagenéticos e do tipo misto, assim como entre os metais traço Ni, Cu, Co e Ti. O Mn e o Fe estão presentes nos nódulos principalmente na forma de espécies oxidadas Mn^{4+} e Fe^{3+} , independentemente do efeito de fracionamento entre eles. Modelos esquemáticos do ambiente de formação dos nódulos são propostos e sugere-se que variações da profundidade da frente redox no sedimento ao longo do tempo são responsáveis pelo efeito de fracionamento entre o Mn e o Fe.

Palavras-chave: Nódulos polimetálicos; Morfologia; Geoquímica; Gênese de nódulos.

ABSTRACT

BENITES, M. **Morphology and chemical composition of polymetallic nodules from the Clarion-Clippertone Zone, the Indian Ocean and Rio Grande Rise, a comparative study.** 2017. 94 p. Dissertation (Master) – Oceanographic Institute, University of Sao Paulo, Sao Paulo, 2017.

Deep sea polymetallic nodules are concretions of manganese and iron oxides formed around a nucleus. They accrete either hydrogenetically – metals precipitate from the seawater – or diagenetically – metals precipitate from the sediment pore water. The accretion process affects both the nodules morphology and geochemistry. In this study, fourteen polymetallic nodules from four ocean regions, namely the Clarion-Clippertone Zone (Northeast Pacific Ocean), the Central Indian Basin (Central Indian Ocean), the Mascarene Basin (West Indian Ocean), and the Rio Grande Rise (Southwest Atlantic Ocean), were used to compare morphological and geochemical aspects between the different oceanic regions. Computed Tomography (CT) was applied to study the nodules internal structure. Scanning Electron Microscopy (SEM) was used to describe the micro layers within the nodules. Chemical composition of growth layers and nuclei was determined by both Micro X-ray Fluorescence (μ -XRF) and Laser Ablation Inductively Coupled Plasma Mass Spectroscopy (LA-ICP-MS). Finally, X-ray Absorption Near Edge Spectroscopy (XANES) was performed in order to determine the speciation (i.e., the oxidation state) of Mn and Fe. Polymetallic nodules from the Central Indian Basin are diagenetic and the ones from the Mascarene Basin and the Rio Grande Rise are hydrogenetic, while nodules from the Clarion-Clippertone Zone are of mixed type. However, the dominant accretion process varies across the nodules resulting in inhomogeneous layer textures and chemical composition. Strong Mn and Fe fractionation occurs in the diagenetic and mixed type nodules accompanied by fractionation of the trace elements Ni, Cu, Co and Ti. Mn and Fe are present in the nodules mainly as oxidized species Mn^{4+} and Fe^{3+} , independently of the degree of fractionation. Schematic models of the nodules environment of formation are proposed, in which and the fractionation of Mn and Fe is possibly the result of the variation of the redox front depth through time.

Key-words: Polymetallic nodules; Morphology; Geochemistry; Genesis of nodules.

FIGURES

Figure 1 Formation environments of polymetallic nodules, from hard rock at seamounts to porous sediment at deep ocean basins. From Hein and Petersen (2013).	15
Figure 2 General map (A) with locations of samples from the Clarion-Clippertone Zone (B), Central Indian Basin and Mascarene Basin in the Indian Ocean (C), and Rio Grande Rise in the Southwest Atlantic Ocean (D). The maps were made using the Ocean Data View free.	22
Figure 3 Nodules from the Clarion-Clippertone Zone.	29
Figure 4 Surface texture of nodules from the Clarion-Clippertone Zone. (A) top and (B) bottom side and hard organisms attached to (C) top and (D) bottom side of nodule JC120-104B.	30
Figure 5 Tomography of nodules from the Clarion-Clippertone Zone in three dimensions.....	31
Figure 6 Polished section of nodule JC120-104B and Scanning Electron Microscopy – Secondary Electron micrographs showing the layers texture: (A) Botryoidal texture on the external portion, (B) dendritic and (C) massive textures in the internal portion. Yellow lines mark the difference in thickness of the recent oxide layer at the top and bottom side.....	32
Figure 7 Scanning Electron Microscopy (SEM) micrograph and Energy Dispersive X-ray Spectroscopy maps of chemical elements on the edge of nodule JC120-104D from the Clarion-Clippertone Zone, Pacific Ocean.	33
Figure 8 (a) Sample JC120-104B from the Clarion-Clippertone Zone, Northeast Pacific Ocean, (b) μ -XRF measurements of elemental composition along the transects on the outer part and on the inner part of the nodule. (c) Color map of Mn (red) and Fe (green).....	35
Figure 9 LA-ICP-MS elemental composition along the transects (a) A-A' and C-C' on the outer part of the nodule and (b) B-B' on the inner part of the nodule JC120-104B from the Clarion-Clippertone Zone, Northeast Pacific Ocean.....	36
Figure 10 XANES measurements of Mn and Fe in standards and in four points in nodule JC120-104B (the points analyzed are numbered from 1 to 4). The dashed line marks the absorption edge for the four points.	38
Figure 11 Nodules from the Central Indian Basin.....	39
Figure 12 Surface texture of nodule AAS21-17 from the Central Indian Basin.....	40
Figure 13 CT tomography of nodules from the Central Indian Basin.....	40
Figure 14 Polished sections of nodules AAS21-19 and SS4-280 with their layer textures viewed under SEM – Secondary Electron.....	41
Figure 15 (a) Sample AAS21-19 from the Central Indian Ocean, (b) μ -XRF measurements of elemental composition along the transect (A-A'). (c) Color map of Mn (red), Fe (green) and K (blue).	43
Figure 16 (a) Sample SS4-280 from the Central Indian Ocean, (b) μ -XRF measurements of elemental composition along the transect (A-A'). (c) Color map of Mn (red) and Fe (green).....	44

Figure 17 LA-ICP-MS elemental composition along the transect (A-A') in nodule AAS21-19 (Central Indian Basin, Indian Ocean).....	45
Figure 18 LA-ICP-MS elemental composition along the transect (A-A') in nodule SS4-280 (Central Indian Basin, Indian Ocean).....	45
Figure 19 Location of the X-ray Absorption Near Edge Spectroscopy (XANES) measurements on sample SS4-280 and the curves for standards and sample SS4-280 points for (A) Mn and (B) Fe.....	46
Figure 20 Nodules from the Mascarene Basin.	47
Figure 21 Surface texture of nodules SK35-24 and SK35-26 from the Mascarene Basin.....	47
Figure 22 CT Tomography of the exterior and internal parts of nodules from the Mascarene Basin.	48
Figure 23 Polished section of nodules SK35-24 and SK35-26 and layers texture viewed by SEM – Secondary Electron.....	49
Figure 24 Sample SK35-24 from the Mascarene Basin, western Indian Ocean. (b) μ -XRF measurements of elemental composition along the transect (A-A'). (c) Color map of Mn (red), Fe (green) and K (blue).	52
Figure 25 Sample SK35-26 from the Mascarene Basin, western Indian Ocean. (b) μ -XRF measurements of elemental composition along the transect (A-A' and B-B'). (c) Color map of Mn (red), Fe (green) and K (blue).	52
Figure 26 LA-ICP-MS elemental composition along the transect (A-A') in nodule SK35-24 from the Mascarene Basin, western Indian Ocean.	53
Figure 27 LA-ICP-MS elemental composition along the transects (A-A' and B-B') in nodule SK35-26 from the Mascarene Basin, western Indian Ocean.....	53
Figure 28 Location of the X-ray Absorption Near Edge Spectroscopy (XANES) measurements and the curves for Mn and Fe standards and points on sample SK35-26.....	54
Figure 29 Coated pebble from Rio Grande Rise (RGR); (A) bottom side and (B) top side; (C) surface texture on opposite sides; (D) foraminifer attached to the nodule surface.....	55
Figure 30 Tomography of nodules from the Mascarene Basin from the exterior and slices on three dimensions.....	56
Figure 31 Polished section of RGR and micrographs of Scanning Electron Microscopy – Secondary Electron showing the layers texture. The Dashed lines mark the nucleus – oxides transition.....	56
Figure 32 (a) Sample RGR from the Rio Grande Rise, southwest Atlantic Ocean. (b) μ -XRF measurements of elemental composition along the transect (A-A'). (c) Color map of Mn (red), Fe (green) and K (blue).....	58
Figure 33 LA-ICP-MS elemental composition along the transects (A-A' and B-B') in sample RGR from the Rio Grande Rise, southwest Atlantic Ocean.	59
Figure 34 Location of the X-ray Absorption Near Edge Spectroscopy (XANES) measurements and the curves for Mn and Fe standards and points on sample RGR.....	60

Figure 35 Principal Component Analysis calculated for the average values of the chemical elements for the μ -XRF data with the scores of each Principal Component. Total variance explained by the two components together is 97.8%.	61
Figure 36 Principal Component Analysis calculated for the average values of the chemical elements for the LA-ICP-MS data with the scores of each Principal Component. Total variance explained by the two components together is 98.8%.	62
Figure 37 Hierarchical clustering of the nodules studied using the LA-ICP-MS data mean of chemical elements for each nodule.....	66
Figure 38 scheme of the mixed-type nodules from the Clarion-Clippertone Zone environment of formation.	68
Figure 39 Condition of formation of oxic-diagenetic nodules from the Central Indian Basin conditions of formation. (A) in the case of low sedimentation of organic matter and (B) in the case of high sedimentation of organic matter.	70
Figure 40 scheme of the hydrogenetic nodules from the Mascarene Basin environment of formation. (A) before and (B) after the nodules become attached.	72

TABLES

Table 1 Polymetallic nodules geographic coordinates and depth.....	23
Table 2 Parameters used for LA-ICP-MS measurements.	27
Table 3 Summary of the morphological aspects of nodules from the Clarion-Clippertone Zone, Pacific Ocean.	32
Table 4 Mean and standard deviation of chemical elements measured by μ -XRF in counts and LA-ICP-MS in % and ppm for JC120-104B.	34
Table 5 Summary of the morphological features of nodules from the Central Indian Basin, Indian Ocean.....	42
Table 6 Mean and standard deviation of chemical elements measured by μ -XRF in counts and LA-ICP-MS in % and ppm in sample AAS21-19.....	42
Table 7 Mean and standard deviation of chemical elements measured by μ -XRF in counts and LA-ICP-MS in % and ppm in sample SS4-280.	43
Table 8 Morphological features of nodules from the Mascarene Basin, western Indian Ocean.	50
Table 9 Mean and standard deviation of chemical elements measured by μ -XRF in counts and LA-ICP-MS in % and ppm in sample SK35-24.	50
Table 10 Mean and standard deviation of chemical elements measured by μ -XRF in counts and LA-ICP-MS in % and ppm in sample SK35-26.	51
Table 11 Morphological features of nodules from the Mascarene Basin, western Indian Ocean.	57
Table 12 Mean and standard deviation of chemical elements measured by μ -XRF in counts and LA-ICP-MS in % or ppm for RGR.	57
Table 13 Polymetallic nodules morphological aspects summary.....	65

CONTENTS

1. INTRODUCTION	13
2. OBJECTIVES	18
3. STUDY AREAS AND CORRESPONDING NODULES DEPOSITS	19
4. MATERIAL AND METHODS.....	23
4.1. Samples and methods summary	23
4.2. X-ray Computed Tomography	24
4.3. Preparation of thin sections and polished sections	25
4.4. Scanning Electron Microscopy	25
4.5. Synchrotron Radiation Analyses	26
4.6. Laser Ablation - Inductively Coupled Plasma – Mass Spectroscopy	27
4.7. Statistical analysis	28
5. RESULTS	29
5.1. Clarion-Clippertone Zone, Northeast Pacific Ocean.....	29
5.2. Central Indian Basin	39
5.3. Mascarene Basin	47
5.4. Rio Grande Rise.....	55
5.5. Statistical analysis	60
6. DISCUSSION	63
6.1. Mechanisms of formation of polymetallic nodules	63
6.2. Characterization of the formation process in the different ocean basins	65
7. CONCLUSIONS	74
REFERENCES.....	75
APPENDIX	80

1. INTRODUCTION

Marine polymetallic nodules, also known as manganese nodules or ferromanganese nodules, are mineral concretions of manganese and iron oxides that form upon the seafloor about a nucleus at a rate of the order of 1 mm per 10^4 to 10^6 years (CRONAN, 1977; HEIN; KOSCHINSKY, 2014). Because of this extremely low growth rate, polymetallic nodules absorb high quantity of rare earth elements and trace elements of relevant economic interest (CRONAN, 1978; GLASBY, 2002; HEIN et al., 2013; HEIN; PETERSEN, 2013). Together with the marine cobalt-rich crusts, the nodules compose the so-called marine ferromanganese deposits (HEIN and KOCHICNKY 2014).

Deep sea polymetallic nodules were early reported by Murray and Irvine (1895), who described the first nodules dredged from the seafloor in the Pacific during the Challenger Deep Sea Exploring Expedition (1872-1876). Since then, the marine polymetallic nodules deposits passed to be more systematically studied only in the 70s and 80s, when a more in deep scientific investigation, driven by economic interests, addressed the question on how they are formed (CRONAN; TOOMS, 1969; BONATTI; KRAEMER; RYDELL, 1972; GLASBY, 1977; CRONAN, 1978; BATURIN, 1988).

Although the polymetallic nodules have been reported from a variety of marine environments, namely abyssal plains, seamounts, plateaus, mid-ocean ridges and continental margins (CRONAN, 1977), they are more concentrated in deep ocean basins. The largest polymetallic nodules fields known to date are located in the Pacific abyssal plains (up to 5000 m depth) of the Clarion-Clippertone Zone (CCZ), in the Peru Basin (PB) and in the Central Indian Basin (CIB). The CCZ hosts the largest and more extensively studied deposit, where nodules density is about 15 kg per m^2 and reaches 75 kg per m^2 in some areas (HEIN; PETERSEN, 2013).

Polymetallic nodules are more concentrated in abyssal plains where the sedimentation rate is low, of the order of a few mm per 10^3 years (GLASBY, 2006). Where sedimentation is inhibited by bottom currents, oxygenation at the sea floor is constant, which promotes oxidation of Mn and Fe (PUTEANUS; HALBACH, 1988; HEIN; PETERSEN, 2013). Deep ocean basins are mostly washed by deep water masses enriched in dissolved oxygen, for example the Antarctic Bottom Water (AABW) bathing the nodules deposits in the Pacific Ocean (GLASBY, 2006), in the Indian Ocean (VINEESH et al., 2009) and in the Atlantic Ocean (KASTEN et al., 1998).

The main mechanisms of nodules growth are hydrogenetic accretion and diagenetic accretion of Mn and Fe layers, well described by many authors (GLASBY, 1977; HALBACH; MARCHIG; SCHERHAG, 1980; HALBACH et al., 1981; DYMOND et al., 1984; HALBACH, 1986; BATURIN, 1988; HEIN et al., 1997). The prevailing growth mechanism is linked to the environment of formation.

Hydrogenetic accretion occurs by oxidation and precipitation of colloidal metals from seawater at a rate of 1 to 10 mm Myr⁻¹ (HEIN; PETERSEN, 2013). On the other hand, diagenetic growth occurs by oxidation and precipitation of metals from sediment pore water, which became remobilized due to the decay of sedimentary organic matter. Diagenetic accretion takes place at rates of the order of 100 mm Myr⁻¹ or more (DYMOND et al., 1984; HEIN; PETERSEN, 2013). During hydrogenetic precipitation, Mn and Fe form respectively δ -MnO₂ (vernadite) and FeOOH. Both compounds incorporate trace elements, such as Co, Pb, Ti and rare earth elements (REE), by surface sorption. The Mn/Fe ratio is about 1 and Mn, Cu, and Ni concentrations are relatively low (HALBACH et al., 1981; VERLAAN; CRONAN; MORGAN, 2004; GLASBY; LI; SUN, 2013).

Diagenetic precipitation is characterized by enrichment in Mn, Cu and Ni – metals released by diagenesis of sedimentary organic matter – and Mn/Fe ratios >5. Mn precipitates as phyllophanates, which exhibit lattice vacancies in which divalent cations like Ni²⁺, Cu²⁺ and Zn²⁺ are incorporated (BURNS; BURNS, 1977).

The morphology and geochemistry of polymetallic nodules are extremely dependent on their genetic process. A classification of polymetallic nodules in terms of their genetic mechanism was proposed by Halbach et al. (1981) and is still widely used. This classification divides nodules into type A (diagenetic), type B (hydrogenetic) and type AB (mixed-type). Most of polymetallic nodules are classified as type AB and form at intermediate grow rates of tenths of mm Myr⁻¹ (HEIN; PETERSEN, 2013). This is the case of the nodules from the CCZ and the Central Indian Basin (HEIN et al., 1997; VINEESH et al., 2009; GONZÁLEZ et al., 2010; MAYUMY AMPARO et al., 2013). Type A nodules are found in the Peru Basin (WEGORZEWSKI; KUHN, 2014), while type B nodules are found in the Cook Islands (HEIN et al., 2015).

Bacterial activity may play a role in the mineralization process of nodules, as suggested by the finding of Mn-cycling bacteria within nodules layers (WANG et al., 2009; WANG; GAN; MÜLLER, 2009; BLÖTHE et al., 2015). However, the details about bacterially-induced mineralization are still to be understood.

Environmental conditions determine which genetic type is dominant in a given polymetallic deposit (figure 1) (HEIN; PETERSEN, 2013). Upon consolidated sediment and even on hard rock substrate polymetallic nodules grow on total exposure to seawater. In these conditions nodule accretion is dominantly hydrogenetic. In contrast, diagenetic accretion dominates in unconsolidated and porous sediment, where metal are remobilized in interstitial water. Mixed-type nodules, formed by a combination of hydrogenetic and diagenetic growth, are more common on seamounts and in deep sedimentary basins.

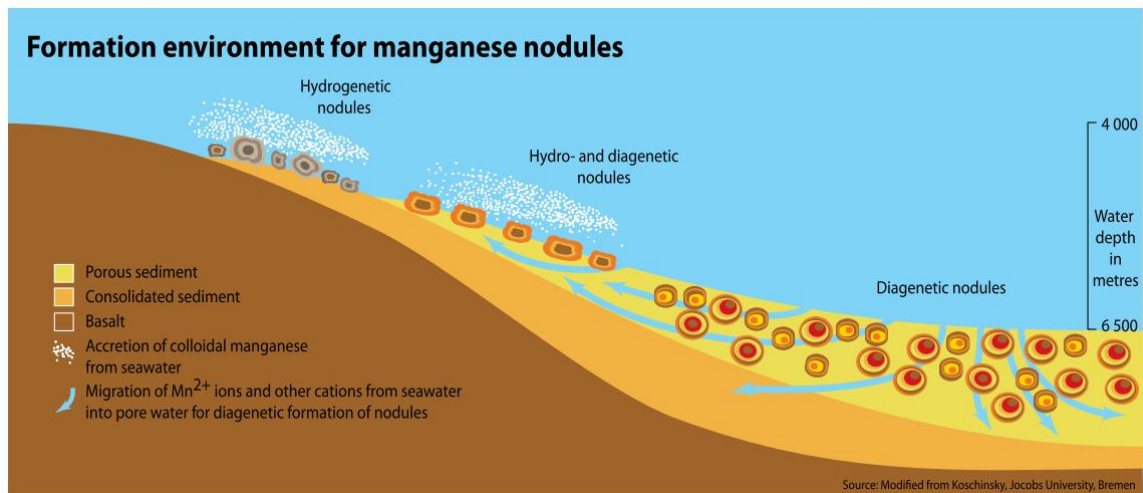


Figure 1 Formation environments of polymetallic nodules, from hard rock at seamounts to porous sediment at deep ocean basins. From Hein and Petersen (2013).

The type of substrate is not the only factor to govern the accretion process of nodules. The availability of nuclei and the sediment composition, together with the organic matter input to the sediments, are fundamental in determining which accretion process prevail. Typical nuclei for nodule accretion are shells, shark's teeth, whale's ear-bones, weathered volcanic rocks, pumice, hardened sediment, and fragments of nodules formed previously (GLASBY, 2006).

The main factor controlling the intensity of diagenesis is the sedimentation rate of organic matter, which in turns is a result of biological productivity in surface waters (HALBACH, 1986). Regions of the ocean where the surface primary productivity is higher correspond to the ones in which the seafloor hosts diagenetic polymetallic nodules, as for example the Peru Basin (DYMOND et al., 1984) and the eastern South Atlantic (KASTEN et al., 1998). Low productivity surface waters, on the other hand, correspond to those

settings where hydrogenetic nodules are found, like in the southwestern Pacific Basin (GLASBY, 2006) and in the Brazilian Basin (KASTEN et al., 1998).

Regarding the polymetallic nodules composition, nodules tend to be enriched in Mn, Fe, Ti, Mg, P, Ni, Cu, Mo, Zn, Co, Pb, Sr, V, Y, Li and REEs relative to the surrounding sediments, while they tend to be in Si, Al and Ba, indicating that these elements have a terrigenous origin (PATTAN; PARTHIBAN, 2011).

The morphology of nodules reflects the conditions of their formation (BATURIN, 1988). Morphological aspects have been used to classify polymetallic deposits, in that a relationship exists between nodules size, abundancy, distribution, Mn/Fe ratio and tonnage of elements of economic interest (MAYUMY AMPARO et al., 2013; VALSANGKAR; REBELLO, 2015). According to (VINEESH et al., 2009), characteristics such as size, shape and surficial texture depend on oceanographic variables of the basin where the nodules are formed, namely topography, currents, bottom water masses and sediment type. Smooth surficial texture has been related to dominantly hydrogenetic growth (MAYUMY AMPARO et al., 2013).

Morphological studies relying on a high number of samples have been performed (VINEESH et al., 2009; MAYUMY AMPARO et al., 2013; VALSANGKAR; REBELLO, 2015). Nevertheless, none of them considered in detail the internal structure of the nodules. Nowadays, thanks to the CT X-ray tomography, it is possible to obtain a high resolution imaging of the interior of the nodules in a non-destructive way, without the need of cutting the nodules, as performed in this study.

Regarding their internal structure, polymetallic nodules present individual concentric layers which may be inhomogeneous in composition and texture. This heterogeneity is considered to be due to changes in environmental conditions during nodules accretion. Hydrogenetic and diagenetic growth have been found to be alternate between individual nodule layers (WEGORZEWSKI; KUHN, 2014), revealing that nodule growth is not in a steady-state and does record changes in environmental conditions during nodule formation.

Despite the extensive literature on the genesis of deep sea polymetallic nodules, the link between formation mechanisms, internal structure, external morphology and geochemical composition of nodules is still poorly documented.

Moreover, even though the occurrence of polymetallic nodules on the flank of the Rio Grande Rise was reported by Milliman and Amaral (1974), no scientific work exists about their morphological and geochemical characterization, or about how these deposits

were formed. This is the first study in which the morphology and the geochemical composition of a nodule from this region are studied in detail, which is of great importance for marine research in Brazil.

This Master Thesis aims to test the hypothesis that polymetallic nodules from different ocean regions may exhibit distinct morphology and chemical compositions, although they were formed by the same process (diagenetic or hydrogenetic).

2. OBJECTIVES

The main goal of this work is to link the mechanisms of nodules formation with their morphology and chemical composition in four ocean regions. For this purpose, polymetallic nodules from the Clarion-Clipperton Zone (Northeast Pacific Ocean), the Central Indian Basin (Central Indian Ocean), the Mascarene Basin (Western Indian Ocean) and the Rio Grande Rise (Southwest Atlantic) were studied aiming to attain the following objectives:

- Describe and compare nodules from different locations, focusing on their external morphology (size, shape and surficial texture);
- Describe and compare nodules from different locations, focusing on their internal structure (thickness and texture of layers and nuclei);
- Determine the major, trace and rare elements composition across the nodules;
- Reveal the geochemical processes that might have acted in the different ocean basins.

The fundamental questions that this work addresses are the following:

- Do the samples used in this work match the genetic type classification described in the literature for the regions under study?
- Does Mn/Fe ratio vary in the same way in all the basins?
- Why does this variation happen? And why does it not?

3. STUDY AREAS AND CORRESPONDING NODULES DEPOSITS

The Clarion-Clipperton Zone (CCZ) corresponds to the ocean basin comprised between the Clarion Fracture Zone and the Clipperton Fracture Zone (figure 2B). The ocean floor at the site is 4000-4500 m deep, punctuated by volcanic seamounts rising up to 2500 m. Deep-sea plains alternated with elongated, approximately N-S oriented horsts and grabens of several kilometres length and height of 100-300 m.

The flat, sediment-covered seafloor is composed by pelagic clay and siliceous ooze (diatoms and radiolaria), deposited at a rate of 0.35-0.5 cm kyr⁻¹ (MEWES et al., 2014). Sediment lacks carbonates as the site is slightly below the carbonate compensation depth. Ferromanganese nodules abundance is on average 10 to 30 kg m⁻² (RUHLEMANN et al., 2011).

Dissolved oxygen is detectable in the sediment pore water until 2-3 m below sea floor (MEWES et al. 2014). Oxygen measurements in pore water suggest that hydrogenetic and oxic-diagenetic processes control the present-day growth of nodules at the study area, since Mn from deeper anoxic sediments is does not reach the sediment surface (MEWES et al. 2014; RUHLEMANN et al. 2011).

The equatorial high bioproductivity zone is located south of the CCZ and produces one of the broader oxygen minimum zones in the global ocean, as a result of upwelling in the eastern Pacific (STRAMMA et al., 2008). The oxygen minimum zone (OMZ) is broad, with a thickness of 400 – 1000 m, which is more pronounced off Mexico and gradually weakens to the north and west (ZHENG et al., 2000).

The carbonate compensation depth (CCD) in the Clarion-Clipperton Zone is between 4200 and 4500 m water depth (INTERNATIONAL SEABED AUTHORITY - ISA, 2010). Sediment distribution is influenced by the Antarctic Bottom Water (AABW) low bottom-current velocities, which is less than 10 cm s⁻¹ predominantly north-westward and highly oxygenated (JOHNSON, 1972).

The Central Indian Basin (CIB) is an isolated basin bounded by three ridge systems on its western (Central Indian Ridge), eastern (Ninety Ridge System) and southern (Mid-Indian Ridge) limits (figure 2C). These ridges act as barrier to strong bottom water currents and terrigenous sediments from all around with exception of the northern boundary. Consequently, the CIB is covered by terrigenous sediments in the northern part (from

Ganges and Bhramaputra rivers) (up to 5°S latitude). The rest of the basin is covered by siliceous radiolarian ooze with sporadic calcareous patches (central part) and red clay (southern part) (BANERJEE; MIURA, 2001). Sedimentation rates in the CIB are between 2.7 and 3.4 mm kyr⁻¹ (BANAKAR; GUPTA; PADMAVATHI, 1991) and the bottom morphology varies between abyssal hills and seamounts.

The CIB's physical characteristics provide a favourable environment for the polymetallic nodules to grow, being this the basin richest in nodules in the whole Indian Ocean. Dominant parameters controlling nodules in the CIB are topography, bottom water current and water depth (VINEESH et al., 2009). Nodules from the central deep basin are large, older and rough, while they are small and smooth in the southeastern part, where the Antarctic Bottom Water (AABW) enters through deep saddles in the Ninety Ridge System. Also, small and smooth nodules dominate locally on the top of seamounts. Older nodules from the protected deeper basins are of diagenetic origin and less influenced by strong water current, while bottom water currents lead to Fe-rich small and smooth nodules in the eastern part of the basin affected by the AABW (VINEESH et al., 2009).

The Mascarene basin (MB) is comprised between Madagascar Island and the Mascarene Plateau and is located to the north of Mauritius Island (figure 2C), formed by basic volcanic rocks, extruded as lava flows. The sediment type of the basin is mostly calcareous clay/ooze. The sediment composition varies from sand to silt in shallower areas to mostly silt clay in deep water. The sediment coarse fraction is composed by preserved planktonic foraminifera, as the basin is above the CCD and the effect of dissolution is not pronounced. Clay minerals are composed mostly of montmorillonite, kaolinite and chlorite, which are indicative of tropical weathering of basic volcanic rocks. Sedimentation rate in the Mascarene Basin is low, especially in the northern part, between 1.4 and 11.3 m kyr⁻¹ (NATH; PRASAD, 1991).

Polymetallic nodules from the Mascarene Basin have been studied and found to be of hydrogenetic origin based on their internal structures and on morphological, chemical, and mineralogical characteristics. Their surficial texture is mostly smooth, growth layers are dominantly columnar, with vernadite as the main Mn mineral phase, enriched in Fe, Co, REE (Ce in particular) and depleted in Mn, Ni and Cu. These nodules originate from an oxygenated environment, due to the presence of Antarctic Bottom Water with low sedimentation rates (NATH; PRASAD, 1991).

The Rio Grande Rise (RGR) is an elevation of more than 4000 m from the surrounding abyssal basin in the Brazilian Basin, western South Atlantic (figure 2D). The

sediments at the crest of RGR are dominantly calcareous ooze (nannofossils and planktonic foraminifera) with a siliceous component (FLORINDO et al., 2015). The area is characterized by a strong northward flow of the AABW, which causes erosion of the bottom sediments (EMELYANOV, 2015). The RGR bottom environment and its polymetallic deposits are yet to be described and understood.

Polymetallic nodules from the west South Atlantic Ocean have been found to be mostly hydrogenetic in origin compared to the mostly diagenetic nodules from the eastern South Atlantic (KASTEN et al., 1998). Moreover, the sediments from the North Brazilian Basin have been described as hydrogenetic polymetallic deposits enriched in hydrothermal Fe and Mn oxyhydroxides relative to other basins in the Atlantic Ocean (DUBININ; RIMSKAYA-KORSAKOVA, 2011).

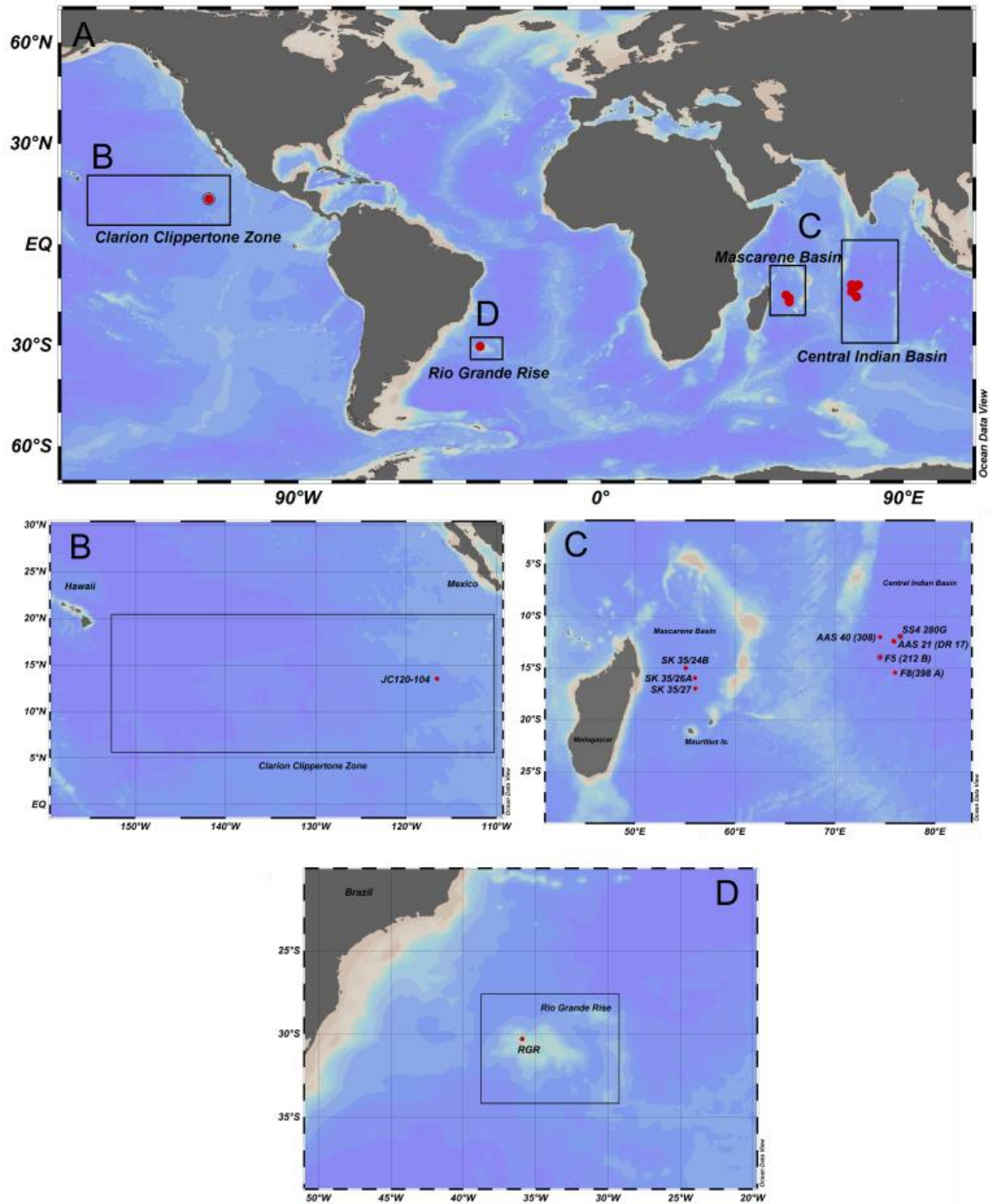


Figure 2 General map (A) with locations of samples from the Clarion-Clippertone Zone (B), Central Indian Basin and Mascarene Basin in the Indian Ocean (C), and Rio Grande Rise in the Southwest Atlantic Ocean (D). The maps were made using the Ocean Data View free.

4. MATERIAL AND METHODS

4.1. Samples and methods summary

Polymetallic nodules used in this work are from the CCZ (4 nodules) in the Pacific Ocean, from the CIB (5 nodules), from the MB (3 nodules) in the Indian Ocean and from RGR (1 Fe-Mn coated pebble) in the southwestern Atlantic.

The samples from the CCZ are identified as JC120-104 and were collected during the oceanographic cruise JC120 on board of the RRV James Cook by Agassiz trawl on 14/5/2015 at 21:20:00 GMT at the location 13° 30.42'N, 116° 35.1295'W and 4130 m depth (figure 1). The nodules from the CIB were collected during different cruises: AAS21 and AAS40 on board of RV Akademik Alexander Sidorenko (Galenzik, Russia) by Okean Grab.

Nodules from the MB were collected during the oceanographic cruise SK35 on board of the ORV Sagar Kanya (Ministry of Earth Sciences [MoES; formerly Department of Ocean Development (DOD)], Government of India) during October-November 1987 by Dredge, Vann Grab and Freefall Grab (table 1). The Fe-Mn coated pebble from the RGR was collected by accident together with material dredged from the bottom during the oceanographic cruise Iatá-Piuna on board of the R/V Yokosuka.

Table 1 Polymetallic nodules geographic coordinates and depth.

	Latitude	Longitude	Depth	Method
Central Indian Basin				
AAS 40 (308)	-12° 3.642'	74° 29.844'	5060	Okean Grab
AAS 21 (DR 17)	-12° 30.204'	75° 54.936'	5410	-
AAS 21(DR 19)	-12° 25.098'	75° 50.178'	5350	-
SS4 280G	-12° 0.000'	76° 30.540'	5400	-
F8(398 A)	-15° 29.040'	75° 59.460'	5150	-
F5 (212 B)	-13° 59.880'	74° 30.000'	5255	-
Mascarene Basin (Western Indian Ocean)				
SK 35/24B	-15° 2.400'	55° 4.000'	4420	Dredge
SK 35/27	-17° 0.400'	56° 1.500'	4528	Vann Grab
SK 35/26A	-16° 0.000'	55° 59.500'	4130	Freefall Grab
Clarion-Clippertone Zone				
JC120-104A	13° 30.420'	-116° 35.100'	4130	Agassiz Trawl
JC120-104B	13° 30.420'	-116° 35.100'	4130	Agassiz Trawl

JC120-104C	13°	30.420'	-116°	35.100'	4130	Agassiz Trawl
JC120-104D	13°	30.420'	-116°	35.100'	4130	Agassiz Trawl
Rio Grande Rise						
RGR	-	-	-	-	-	Dredge

The nodules were photographed, measured and finally scanned by three dimensions X-Ray Computed Tomography (CT). The shape and surface texture were classified following the nomenclature used by Glasby (1977) and Vineesh et al. (2009), in which the shape is: (1) spheroidal; (2) ellipsoidal; (3) discoidal; (4) tabular; (5) polynodules (6) biomorphic –when it reflects the shape of a biological material; or (7) faceted – when it follows the angular shape of a clastic nucleus. In this classification, the surface texture is defined as: (1) rough; (2) smooth or (3) botryoidal. The layers textures were classified according to Halbach et al. (1981) as: (1) massive; (2) dendritic; (3) laminar; or (4) columnar.

Next, thin sections with approximately 100 µm thickness were prepared from the nodules JC120-104B, AAS21-DR19, SS4-280G, SK35/24B and SK35/26A. These thin sections were used for Scanning Electron Microcopy and for two kinds of Synchrotron analyses, namely Micro X-ray Fluorescence and X-ray Absorption Near Edge. Polished sections 7 – 8 mm thick were also prepared for Laser Ablation – Inductively Coupled Plasma Mass Spectroscopy (LA-ICP-MS) analysis at the National Oceanographic Centre, Southampton, UK.

4.2. X-ray Computed Tomography

Three dimensions Computed Tomography (CT) were run using a Versa XRM-510 Xradia equipment from Zeiss at the Technological Characterization Laboratory from Escola Politécnica, University of Sao Paulo.

All the nodules were scanned for 2 hours while turning under a 160 kV 10 W X-rays source. Pixel size was 55 µm and detector resolution of 1024 x 1024 pixels, transmission of 8 – 19%.

4.3. Preparation of thin sections and polished sections

Thin sections (100 μm thick) were prepared at the Institute of Geoscience of the University of Sao Paulo. Firstly, the nodules were embedded in a 6:1 solution of epoxy resin and hardener and kept under vacuum (-25 mPa) for six hours in order to ensure resin penetration. Samples were then dried in an oven for two days.

Once the resin was completely dried, the nodules were cut in two halves. A second cut was made parallel to the first one, in order to get a slab approximately 5 mm thick. The first cut was done using a metal jaw and the second one was done using a diamond wire, both using water cooling.

The surface of the slabs was impregnated with epoxy resin to avoid material loss during grinding. To do this, the slabs were placed onto a hot plate where a solution of epoxy resin, hardener and acetone was poured onto the slab surface.

Once the resin was dried, the slabs were grinded on a diamond wheel 320 with SiC 600 grit. Then, the slabs were placed on glass slides and cut into 100 μm sections. Next, they were polished using a polish cloth 8" DiaMat from Allied High Tech Products under 180 RPM rotation adding a mixture of alumina 1 μm and Ethane Diol oil. Finally, the thin sections were coated with carbon to give them the electric conductivity necessary for SEM analysis.

Polished sections were also prepared for LA-ICP-MS analyses at the National Oceanographic Centre. The nodules sections embedded in resin were cut into a 7 – 8 mm thick slab and their surface was grinded using a 37 μm fixed diamond wheel, making sure to keep the sample flat. Then, the samples were lapped using 9 μm SiC on flat glass to remove any grinding marks and to prepare the surface for polishing. Polishing of the samples was done on a flat wheel with 15 μm , 9 μm , 3 μm , and finally 1 μm diamond at 80 rpm for around 10 minutes each. The samples were cleaned between each stage and were polished in different orientations to prevent striations.

4.4. Scanning Electron Microscopy

Scanning Electron Microscopy (SEM) micrographs were performed using a Leo 440i from Leo Electron Microscopy Ltd at the Laboratory of Scanning Electron Microscopy (LabMEV), Institute of Geosciences of the University of Sao Paulo.

Secondary Electron (SE) and Backscatter Electron (BSE) micrographs were taken from selected points previously observed by optical microscopy. The control of the positions of each point was possible due to a XY coordination system standardized between the optical microscope and the SEM. Analyses were performed at high vacuum condition with Electron High Tension (EHT) of 20 keV, Work Distance (WD) of 25 mm and I_{probe} of 1.0 - 2.0 nA (probe current).

Energy Dispersive Spectroscopy was performed in a Si (Li) solid state detector with INCA 300 software from Oxford Microanalysis group.

4.5. Synchrotron Radiation Analyses

Synchrotron Radiation analyses applied in this work included micro X-ray Fluorescence (μ -XRF) and X-ray Absorption Near Edge Spectroscopy (XANES) and were performed at the Brazilian Synchrotron Light Laboratory (LNLS), XRF Beamline, from 19th – 23th September 2016 and from 14th – 18th February 2017. Thin sections of the samples JC120-104B, AAS21-19, SS4-280G, SK35-26 and SK35-24 were analyzed in order to map the distribution of elements and to gather information on the oxidation state of Fe and Mn present in the nodules.

Micro-XRF punctual measurements were performed in triplicate at selected points in all nodules in order to obtain the elemental composition. Afterwards, 0.1 mm thick transects across the nodules were performed to get profiles of elemental composition variability. Those transects were obtained on steps of 0.02 mm and count time per point of 600 ms, with a velocity of $0.0328 \text{ mm}\cdot\text{s}^{-1}$.

Both punctual analysis and maps, including transects, were acquired at 10 keV. Filters of Fe 3 mm plus Fe 6 mm were used because of the high content of Fe in the samples, what caused dead time of nearly 100%. After adding the filters, the dead time dropped to less than 10%.

The spectrograms were then processed using the open software PyMCA Software Version 5.1.2, downloaded from <http://pymca.sourceforge.net/download.html>, where the curves were calibrated, Excel files were generated and color maps were obtained. From the Excel files, curves of relative elemental concentration were plotted and the Mn/Fe ratio was calculated.

XANES measurements were realized focusing on the absorption spectra of Fe and Mn for samples JC120-104B, SS4-280, SK35-26, and RGR, thus one nodule analyzed for each ocean basin considered. XANES scans were performed three times for each point, in order to increase analytical precision. Metal foils of Mn and Fe were used for beam calibration. Internal standards of FeOOH, FeO, Fe₂O₃, MnO, MnO₂ and Mn₃O₄ were also scanned. XANES curves were processed using the Athena Software from the Demeter XAS package, available at <https://bruceravel.github.io/demeter/>. XANES data processing included pre-edge and post-edge normalization. Each XANES datum results from the average of the triplicate measurements. Self-absorption correction was not performed because no stoichiometric formula of the sample matrix is available. However, this correction is not critical for the purpose of this study, because self-absorption affects only the height of the peaks but not their position on the energy axis. The identification of the Mn and Fe species were done by comparing the energy position of the first derivative of the samples curve with the patterns curves using the Athena Software.

4.6. Laser Ablation - Inductively Coupled Plasma – Mass Spectroscopy

Elemental analyses were performed by LA-ICP-MS at the National Oceanographic Centre, Southampton using a New Wave UP213 laser ablation system coupled to a Thermo X-Series II quadrupole ICP-MS.

Polished section of nodules JC120-104B, AAS21-19, SS4-280, SK35-26, SK35-24 and the coated pebble RGR were loaded into the laser's sample holder along with polished chips of NIST 610, NIST 612, BHVO-2G and BCG-2G reference glass standards. The tranference of ablated material into the ICP-MS occurs through He flow via a three port mixing bulb. All ICP-MS and laser settings were optimized for optimal sensivity and stability.

The New Wave laser system software was used to map across each sample and standard and to set the shot positions, which were aligned along a transect across the nodule sample with shot interval space of 0.25 mm.

Table 2 Parameters used for LA-ICP-MS measurements.

Spot size	Pulse rate	Energy	He flow	Ar flow	Acquisition Time	Wash time between shots
-----------	------------	--------	---------	---------	------------------	-------------------------

25 um	5 Hz	25%	1000 mL.min ⁻¹	400-600 mL.min ⁻¹	20 s	40 s
-------	------	-----	------------------------------	---------------------------------	------	------

A set of multiple measurements of the standards was performed every one hour. Each of the four standards was measured 10 times under the same parameters used for the sample material.

Data calibration was carried out by producing a 5-point calibration line using the values of: (1) gas blank; (2) average NIST 610; (3) average NIST 612; (4) average BHVO-2G; and (5) average BCR-2G.

Reference concentration values for the analytes of interest are the “preferred” values extracted from the GeoReM database [see: georem.mpch-mainz.gwdg.de].

Calibration factors were determined for each element by comparing the measured Counts per Second (CPS) values of the standards with their certified concentration. These factors were then applied to calibrate all unknown shots (external calibration). The element Fe (⁵⁶Fe) could not be determined due to the mass interference of Ar and O (⁴⁰Ar¹⁶O).

4.7. Statistical analysis

Principal Component Analyses of chemical composition data from μ -XRF and LA-ICP-MS were performed using the R language and the RStudio Software Version 0.99.903, downloaded from <https://www.rstudio.com/products/rstudio/download/>.

5. RESULTS

5.1. Clarion-Clippertone Zone, Northeast Pacific Ocean

Nodules from the CCZ (JC120-104A, JC120-104B, JC120-104C and JC120-104D) are 8 cm average long, discoidal and exhibit rough surface textures (figure 3 A-D). The surface texture is more botryoidal than rough on the top side (figure 4A) and purely rough on the bottom side (figure 4B), where the nodule surface is more friable. The CCZ nodules present also a pronounced rim marking the transition between rough and rough-botryoidal texture. This rim corresponds to the limit between the buried and exposed portion of the nodules (i.e., the sediment-water interface). Biological structure like whitish-beige worm tubes and radiolaria tests are found attached to the nodules surface on both sides, but dominantly on the botryoidal one (figure 4C and D).

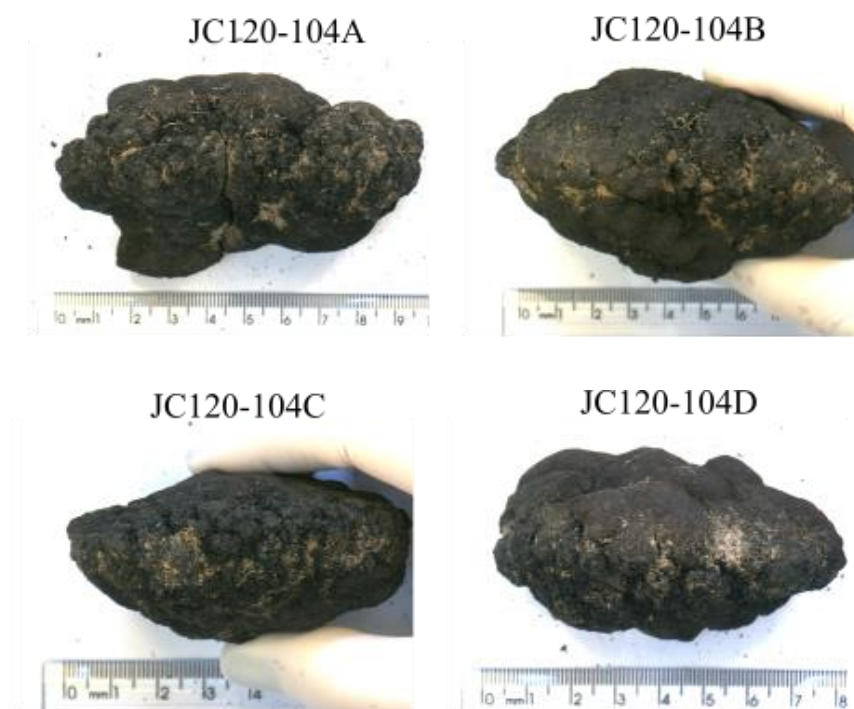


Figure 3 Nodules from the Clarion-Clippertone Zone.

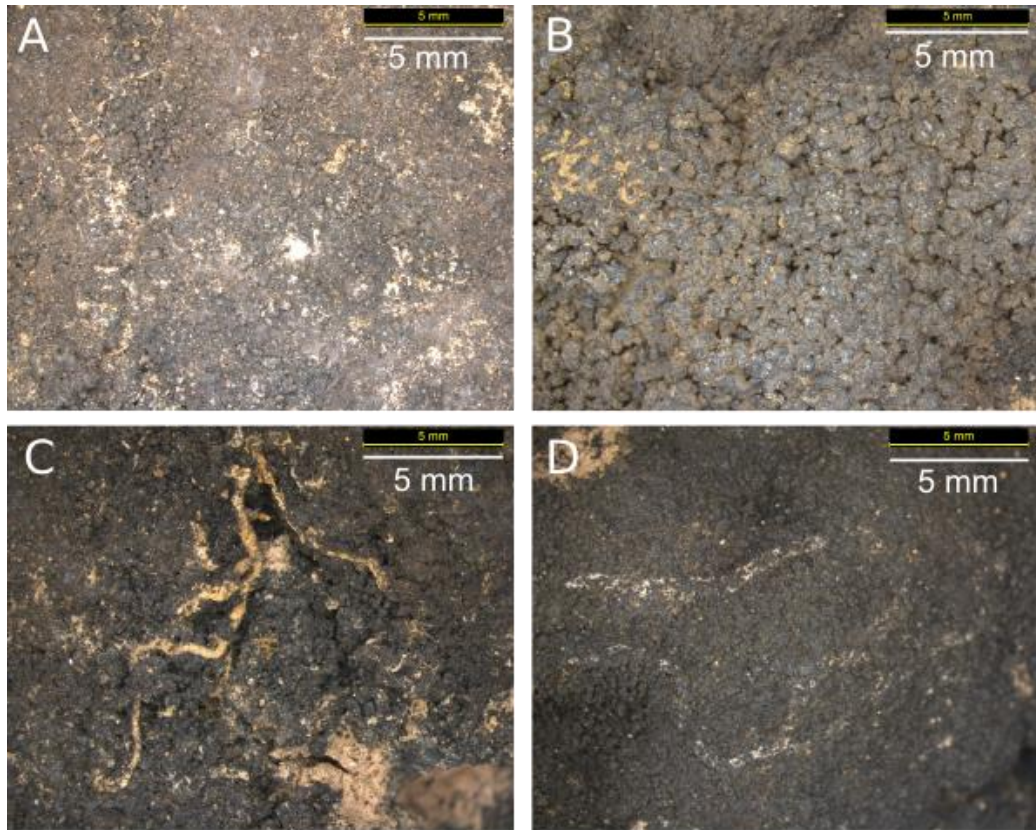


Figure 4 Surface texture of nodules from the Clarion-Clipperton Zone. (A) top and (B) bottom side and hard organisms attached to (C) top and (D) bottom side of nodule JC120-104B.

Regarding the internal structure, nodules from the CCZ present no apparent nucleus and two distinct structure patterns: (1) an internal and (2) an external one. Both of them show a variable layering (figure 5). The internal portion shows alternation of porous and massive thick (1-3 mm) layers. The high-density contrast between these layers can be visualized by the variability of grey tones on the tomography images (figure 5). This portion of nodule apparently grew in a preferential direction, resulting in a conic geometry indicated by the yellow arrow in figure 5. The external portion, however, presents alternation between thin (50-200 μm) bright and dark layers which grew all around the internal portion. This fact suggests that the internal portion of the nodule likely served as nucleus for the external portion. Thus, the internal portions of the CCZ nodules likely correspond to a former deposit that experienced different environmental conditions in comparison to the recent deposit, as reflected by their distinct morphological aspects. This former deposit comprises 60 – 80% of the nodules size. Still, the recent oxide layer is thicker on the one side relatively to the opposite one (figure 6). The morphological features of the nodules from the CCZ in the Pacific Ocean are summarized by table 3.

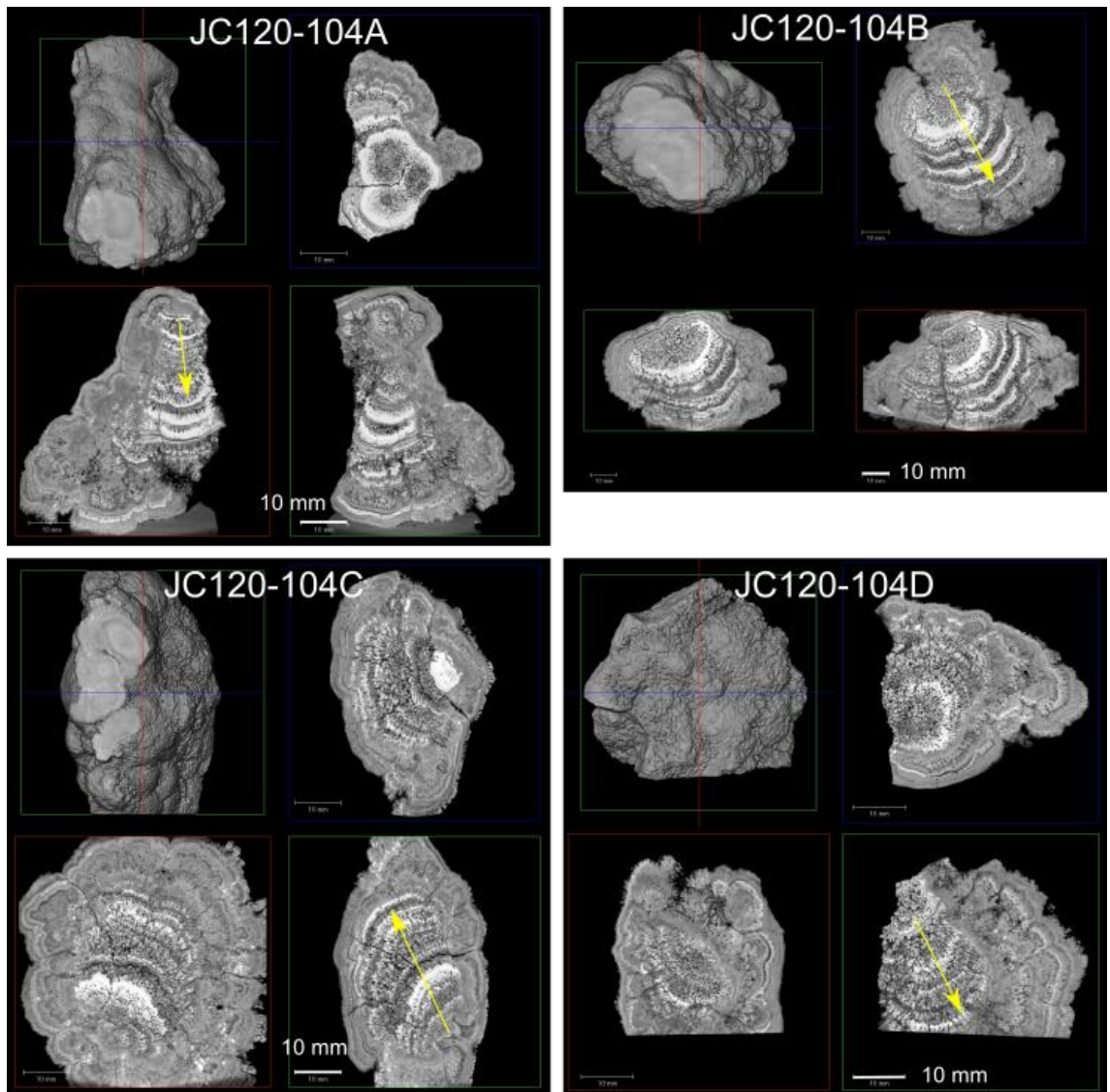


Figure 5 Tomography of nodules from the Clarion-Clippertone Zone in three dimensions.

The SEM micrographs revealed in detail the texture of layers inside the nodules. The thin layers encountered within the external portion are mostly botryoidal, with variable grey tone and variable thickness, much thinner than the layers from the internal portion (figure 6A). The micrographs confirm that the bright thick layers are massive and alternate with the porous layers in which the rock grew following a cauliflower – dendritic pattern, as described by Halbach et al. (1981) (figure 6B and 6C).

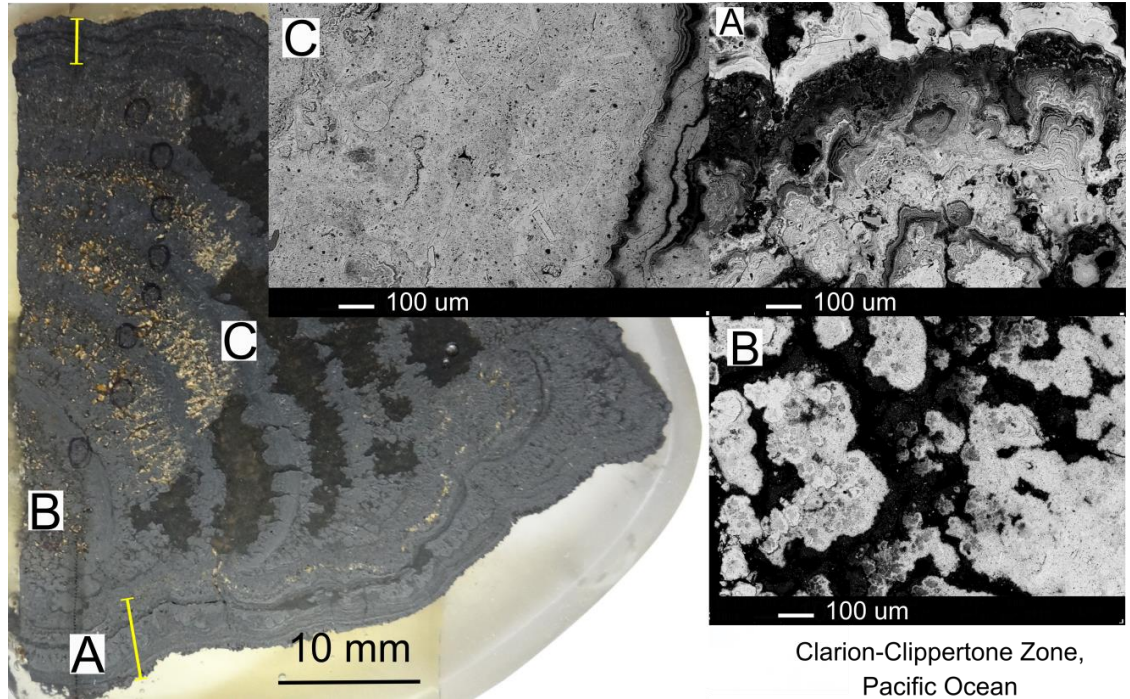


Figure 6 Polished section of nodule JC120-104B and Scanning Electron Microscopy – Secondary Electron micrographs showing the layers texture: (A) Botryoidal texture on the external portion, (B) dendritic and (C) massive textures in the internal portion. Yellow lines mark the difference in thickness of the recent oxide layer at the top and bottom side.

Table 3 Summary of the morphological aspects of nodules from the Clarion-Clippertone Zone, Pacific Ocean.

	JC120-104A	JC120-104B	JC120-104C	JC120-104D
Nodule dimensions	9 x 6.5 x 5 cm	8.5 x 7.3 x 5.5 cm	7 x 6 x 4 cm	8 x 6 x 4.5 cm
Shape	discoidal	discoidal	discoidal	discoidal
Surface texture	botryoidal top side and rough bottom side			
Nucleus	possibly a former deposit			
Nucleus/Nodules size ratio	not applied	not applied	not applied	not applied
Internal layering	yes, highly variable	yes, highly variable	yes, highly variable	yes, highly variable
Thickness of layers	external part: 50-200 µm ; internal part: 1-3 mm	external part: 50-200 µm ; internal part: 1-3 mm	external part: 50-200 µm ; internal part: 1-3 mm	external part: 50-200 µm ; internal part: 1-3 mm
Texture of layers	alternation between botryoidal, massive and dendritic			

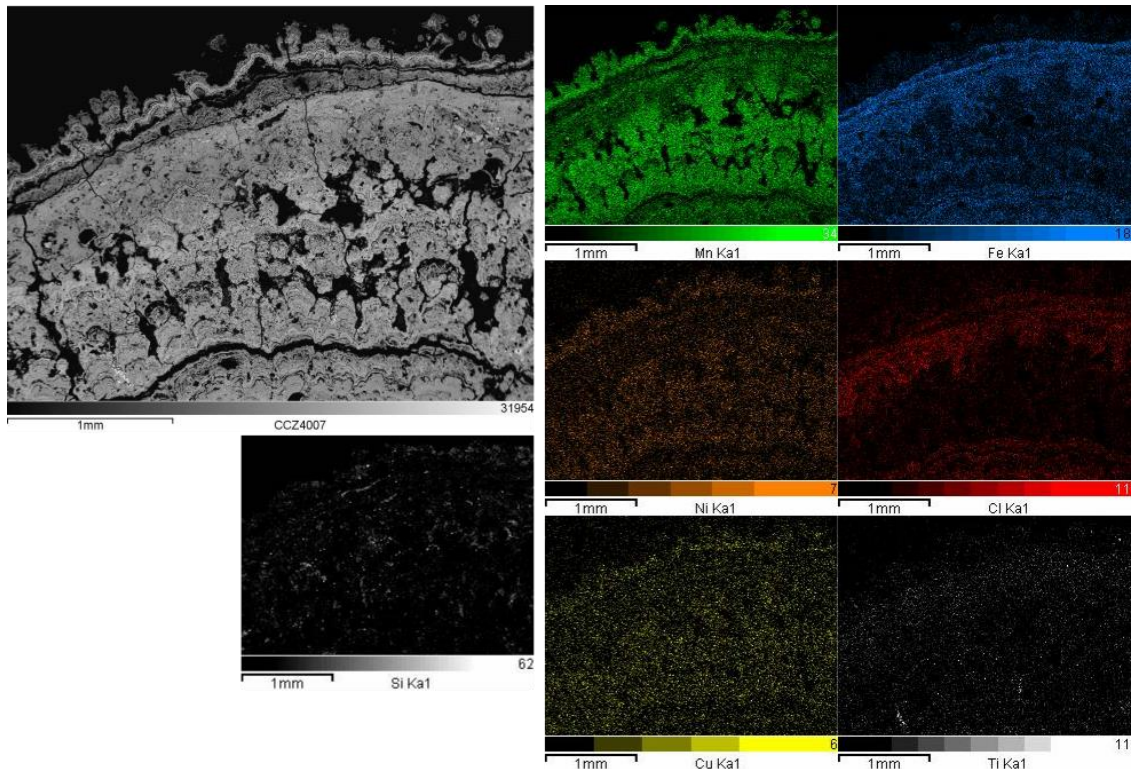


Figure 7 Scanning Electron Microscopy (SEM) micrograph and Energy Dispersive X-ray Spectroscopy maps of chemical elements on the edge of nodule JC120-104D from the Clarion-Clippertone Zone, Pacific Ocean.

SEM-EDS maps of the sample JC120-104D showed a clear relation between the texture of the layer and the concentration of major elements (figure 7). Mn and Fe alternate in a way in that Mn-rich layers correspond to the more porous ones, while the Fe-rich layers correspond to the more massive ones. Mn is accompanied by Ni, and at a lower degree by Cu. Fe, on the other hand, is accompanied by Cl and Ti to a lesser degree. Si is highly concentrated at some spots, where detrital material is probably present.

Micro-XRF analyses reveal that the elemental composition of nodules consists mainly of Mn, Fe, Cu, Ni, Zn, Ce, Ca, Ti, Co, Sr and K (table 4). The most noticeable fact is the high standard deviation of the values, showing the high compositional variability inside each nodule.

LA-ICP-MS data show that the most dominant elements are Mn, Si, Ca and K, which concentration is given in %. All the other elements are expressed in ppm and present the following order of magnitude: (1) 10000 ppm for Ti, Ni and Cu; (2) 1000 ppm for Co, Zn, Sr, Ba, Pb and the total REY; (3) 100 ppm for V, Y, Zr, Nb, Mo, La, Ce and Nd; (4) 10 ppm for Sc, Cr, Pr, Sm, Eu, Gd, Dy, Er, Yb, Hf, Th and U; (5) 1 ppm for Cs,

Tb, Ho, Tm and Lu; and (6) 0.1 ppm for Ta and Pt (Appendix A table 1). Like for the μ -XRF data, the element concentrations obtained by LA-ICP-MS are highly variable, with generally high standard deviations (table 4).

Table 4 Mean and standard deviation of chemical elements measured by μ -XRF in counts and LA-ICP-MS in % and ppm for JC120-104B.

μ -XRF	Mean	Std deviation	LA-ICP-MS	n=124	Mean	Std deviation
Mn	23903.72	15164	Mn	%	42.68	19.23
Fe	2795.14	1638.99	Si	%	5	2.79
Cu	665.64	354.78	Ca	%	1.58	0.75
Ni	542.24	282.6	K	%	1.31	0.46
Zn	186.22	179.78	Ni	ppm	12298.91	7654.93
Ce	87.57	54.32	Cu	ppm	11658.03	6731.24
Ca	37.9	38.26	Zn	ppm	3578.35	2687.49
Ti	30.9	34.99	Ti	ppm	2542.8	2599.83
Co	25.42	46	Co	ppm	1395.26	1693.19
Sr	3.14	4.58	Sr	ppm	595.47	405.06
K	2.16	7.52	REY	ppm	521.39	473.7
Mn/Fe	10.68	8.86	Ce	ppm	289.55	372.47

When looking at the element concentration profile obtained by μ -XRF across the nodule JC120-104B, it is possible to see that CCZ nodules present a distinct alternation between Mn enriched and Fe enriched layers, both on the external and the internal sample as evidenced by the μ -XRF maps and the curves (figure 8). In these elemental composition maps, Mn and Fe signal intensities are represented by red and green color scales, respectively. Metal composition diagrams also show that Ni and Cu follow the behavior of Mn, while Co and Ti follow the behavior of Fe. The Mn/Fe ratio varies between 2 and 40 with mean value of 10. The highest Mn/Fe ratios (up to 40) are found in the massive layers in the internal portion of the nodule. A correspondence between thick and massive layers to high Mn content and porous texture to high Fe content is observed.

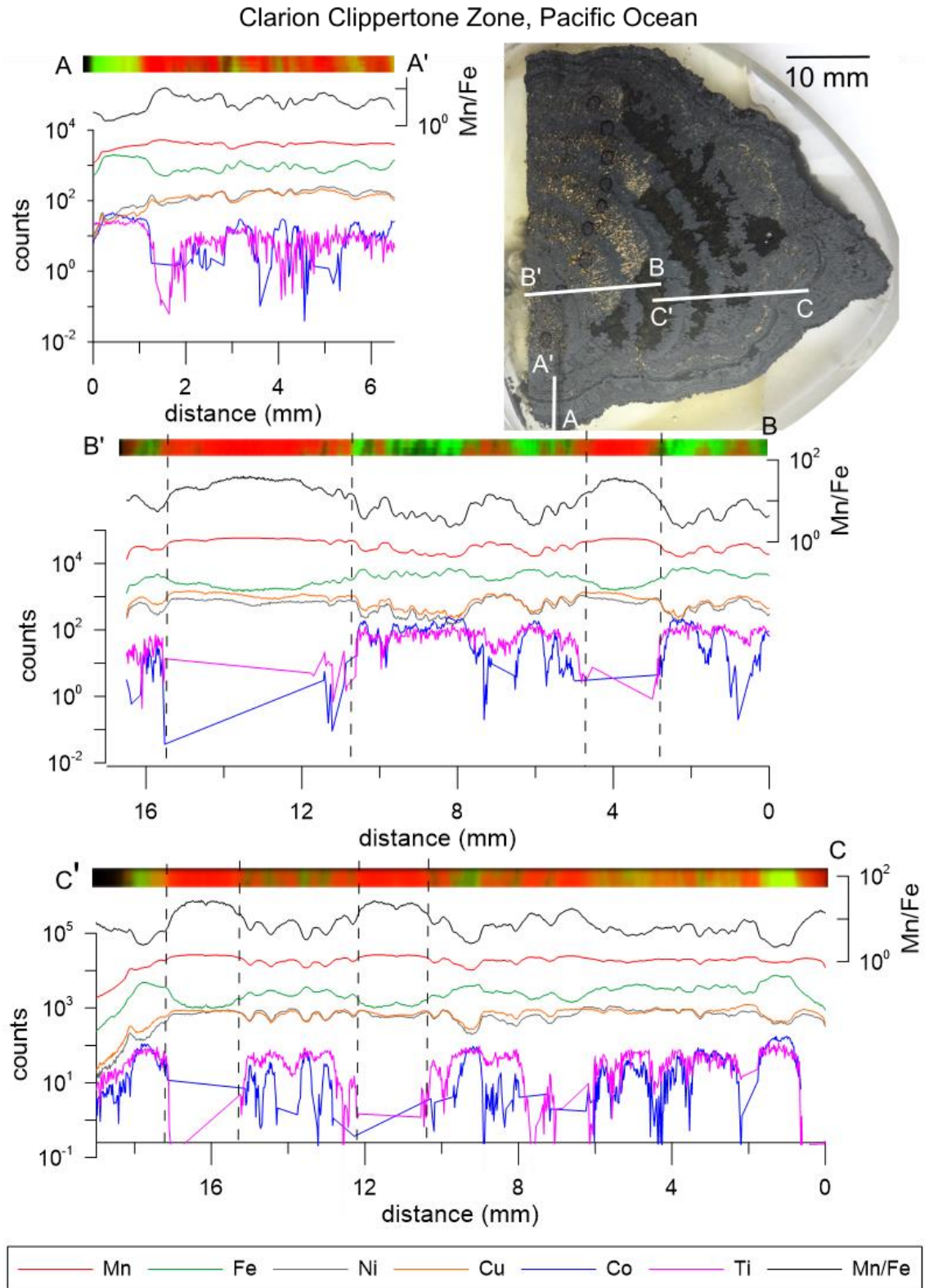


Figure 8 (a) Sample JC120-104B from the Clarion-Clippertone Zone, Northeast Pacific Ocean, (b) μ -XRF measurements of elemental composition along the transects on the outer part and on the inner part of the nodule. (c) Color map of Mn (red) and Fe (green).

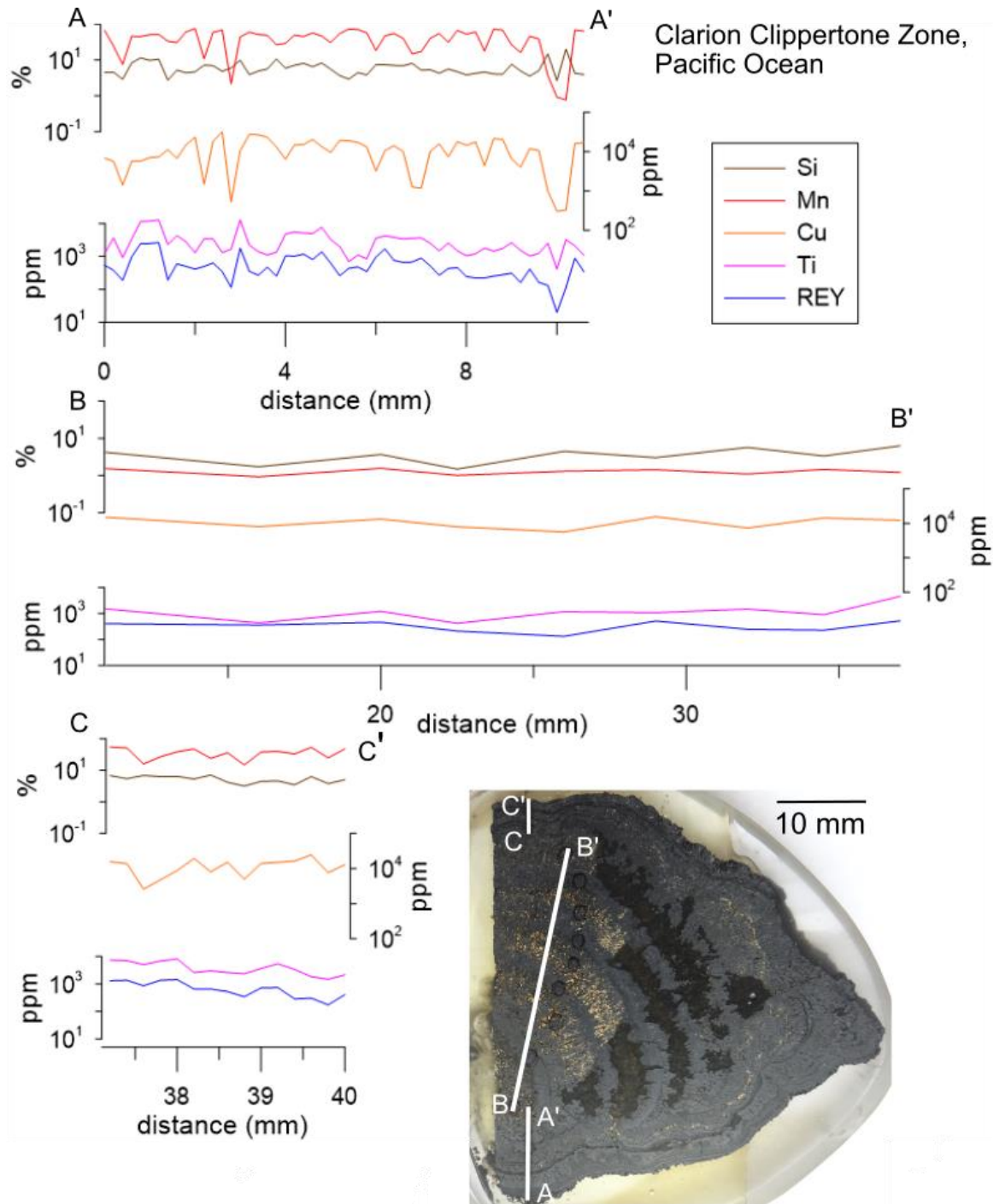


Figure 9 LA-ICP-MS elemental composition along the transects (a) A-A' and C-C' on the outer part of the nodule and (b) B-B' on the inner part of the nodule JC120-104B from the Clarion-Clippertone Zone, Northeast Pacific Ocean.

Results of LA-ICP-MS measurements across the JC120-104B sample show that on the bottom side of the nodule (transect A-A') Cu varies in harmony with Mn, while Ti and the REE show an opposite behavior (figure 9). However, on the top side of the

nodule (transect C-C') the opposite behavior of the groups Cu-Mn and Ti-REE is not observed, nor is it observed across the first half of the points analyzed in the internal portion. Still, REE are less concentrated in the bottom side. It is relevant to remember that the external layers at the top side are thinner than the bottom one.

The alternation between Mn-rich and Mn-poor layers exists. Fe could not be measured by this analytical technique, but relying on the fact that the Mn pattern is the same as the one obtained by μ -XRF, the Fe pattern is predicted to be similar as well. In the internal portion, the Mn concentration obtained by LA-ICP-MS seems not to agree with the μ -XRF data, since the highest Mn concentration does not always correspond to the massive layers, as it was found based on μ -XRF data.

XANES spectra of the four points measured in nodule JC120-104B showed the first derivative closest to the energy of the standards Mn_3O_4 and MnO_2 (on the X axis) (figure 10). The height of the curve (on the Y axis) is meaningless, since it is disturbed by a self-absorption effect that could not be corrected for. In the same way, the spectra of Fe absorption showed the first derivative closest to Fe_2O_3 and FeOOH . These results indicate that both the Mn and the Fe present in the nodule are present in the oxidized form.

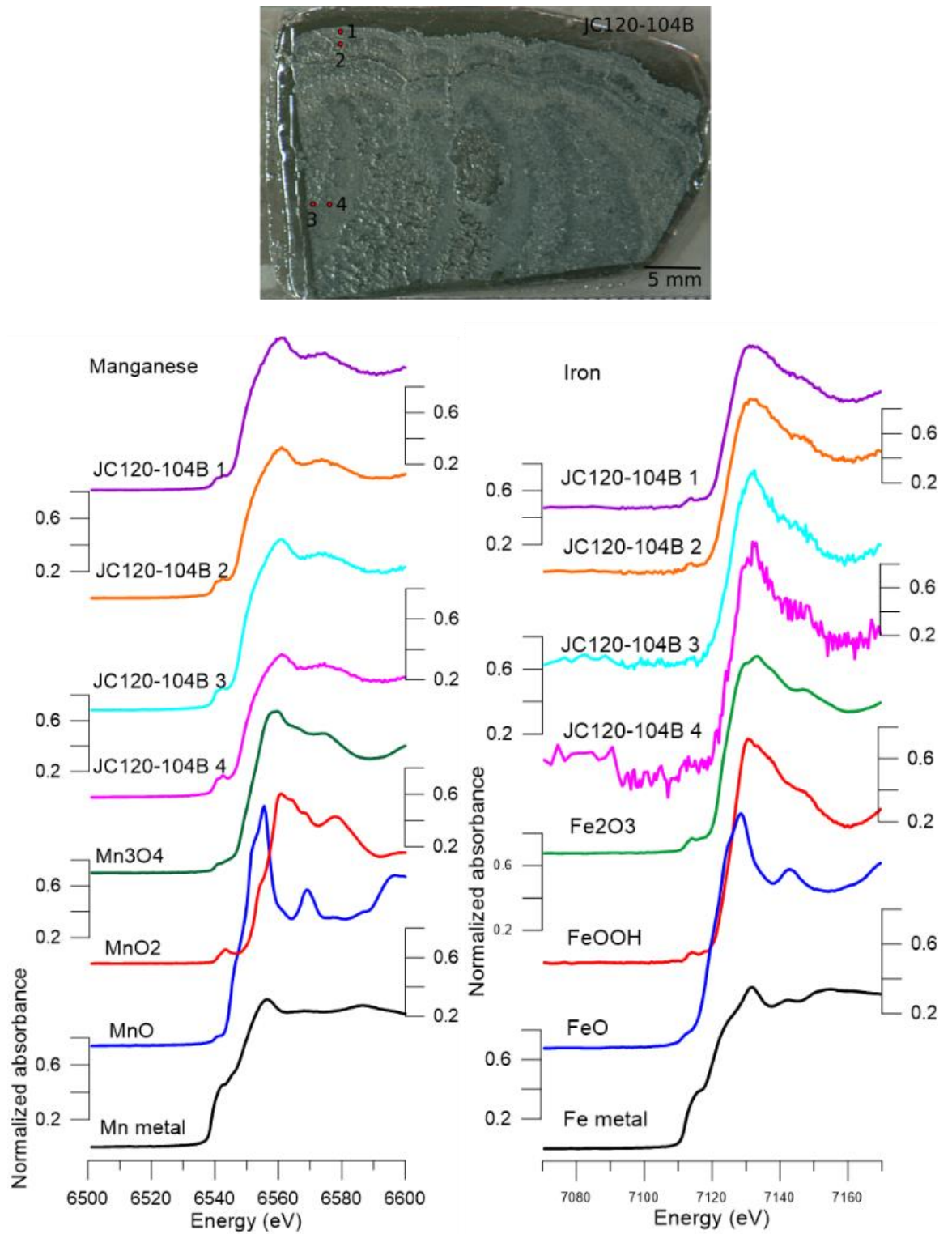


Figure 10 XANES measurements of Mn and Fe in standards and in four points in nodule JC120-104B (the points analyzed are numbered from 1 to 4). The dashed line marks the absorption edge for the four points.

5.2. Central Indian Basin

Nodules from the Central Indian Ocean (AAS40, AAS21-17, AAS21-19, SS4-280 and F8-398) are 3-6 cm long (figure 11) with spheroidal to elongate shape, except for nodule F8-398a that is faceted. These nodules present a rough to smooth surface texture all over their surfaces as exemplified by AAS21-19 (figures 12), with the exception of nodule F8-398a which is smooth. Biological structures, like hard worm tubes, are also found upon the nodules surface, but to a lesser degree relative to the CCZ nodules.

Three of the four nodules from the Central Indian Basin are polynucleated (figure 13), which results from oxides growth around more than one nucleus. In these nodules, the nuclei correspond to 40-50% of the nodules volume. Nodule SS4-280, on the other hand, is mononucleated and exhibits a small nucleus relative to its size (10%). Layer texture varies between dendritic and botryoidal, with a high-density contrast between the two textures (figure 14). The dendritic layers present the highest porosity. The morphological aspects of the nodules from the CIB are summarized in table 5.

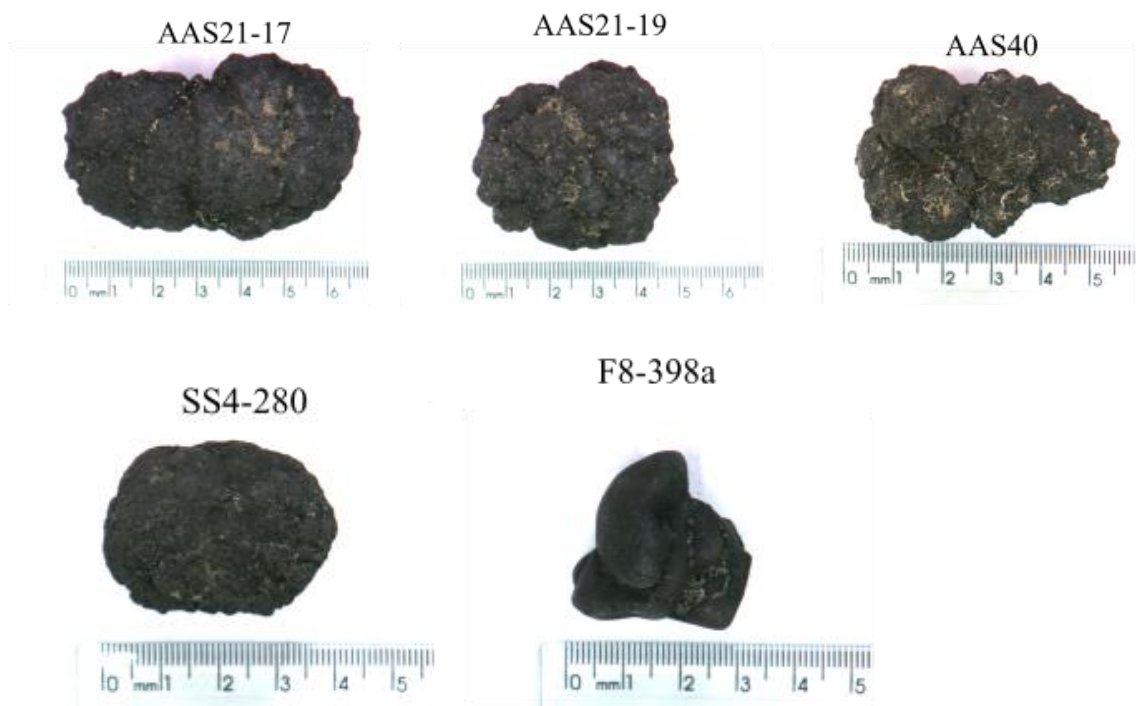


Figure 11 Nodules from the Central Indian Basin.

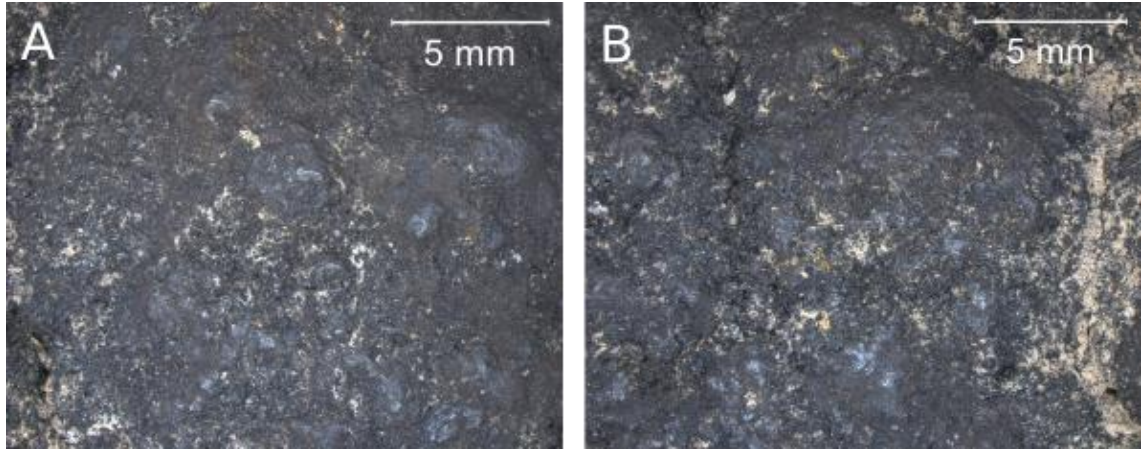


Figure 12 Surface texture of nodule AAS21-17 from the Central Indian Basin.

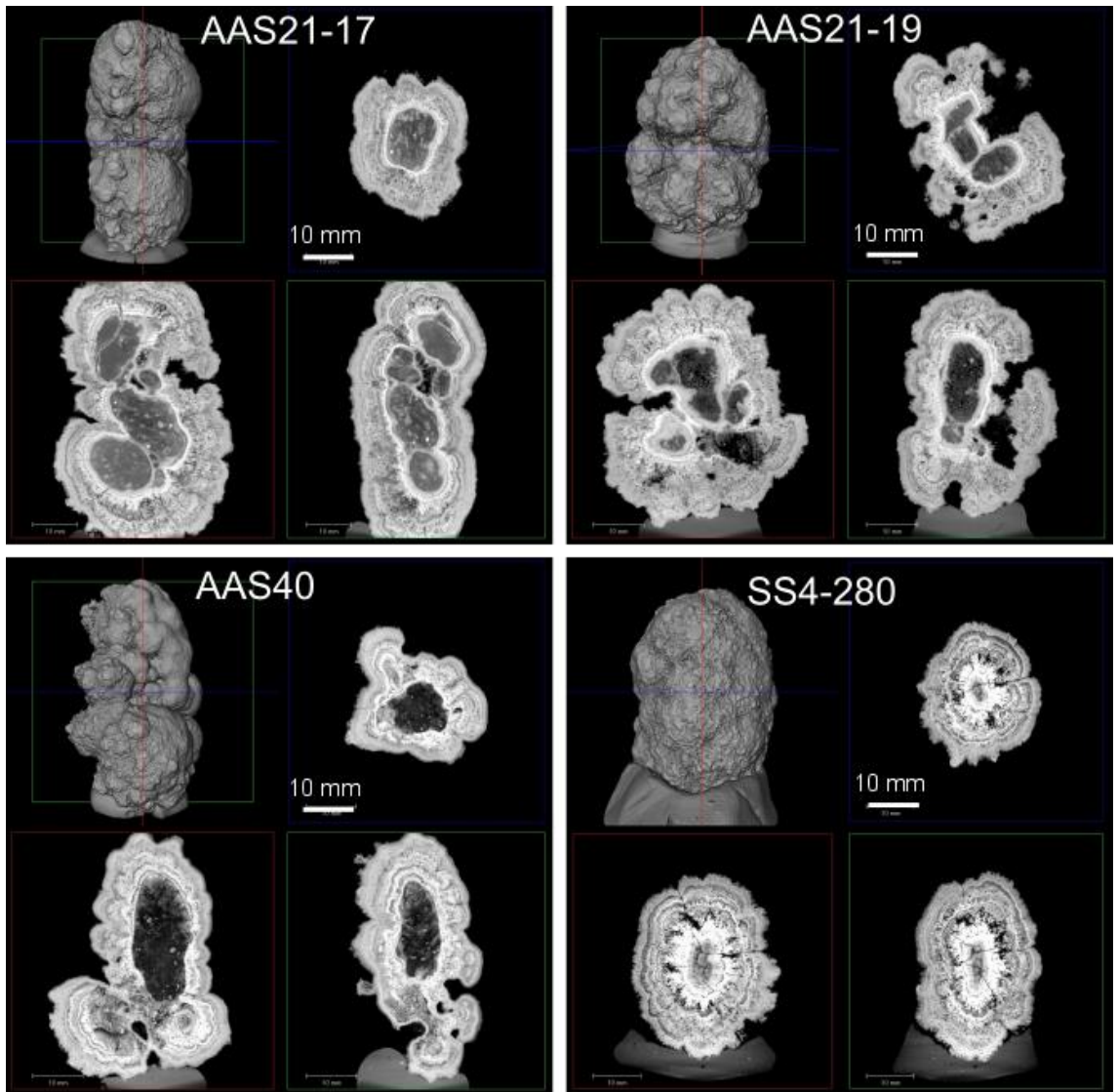


Figure 13 CT tomography of nodules from the Central Indian Basin.

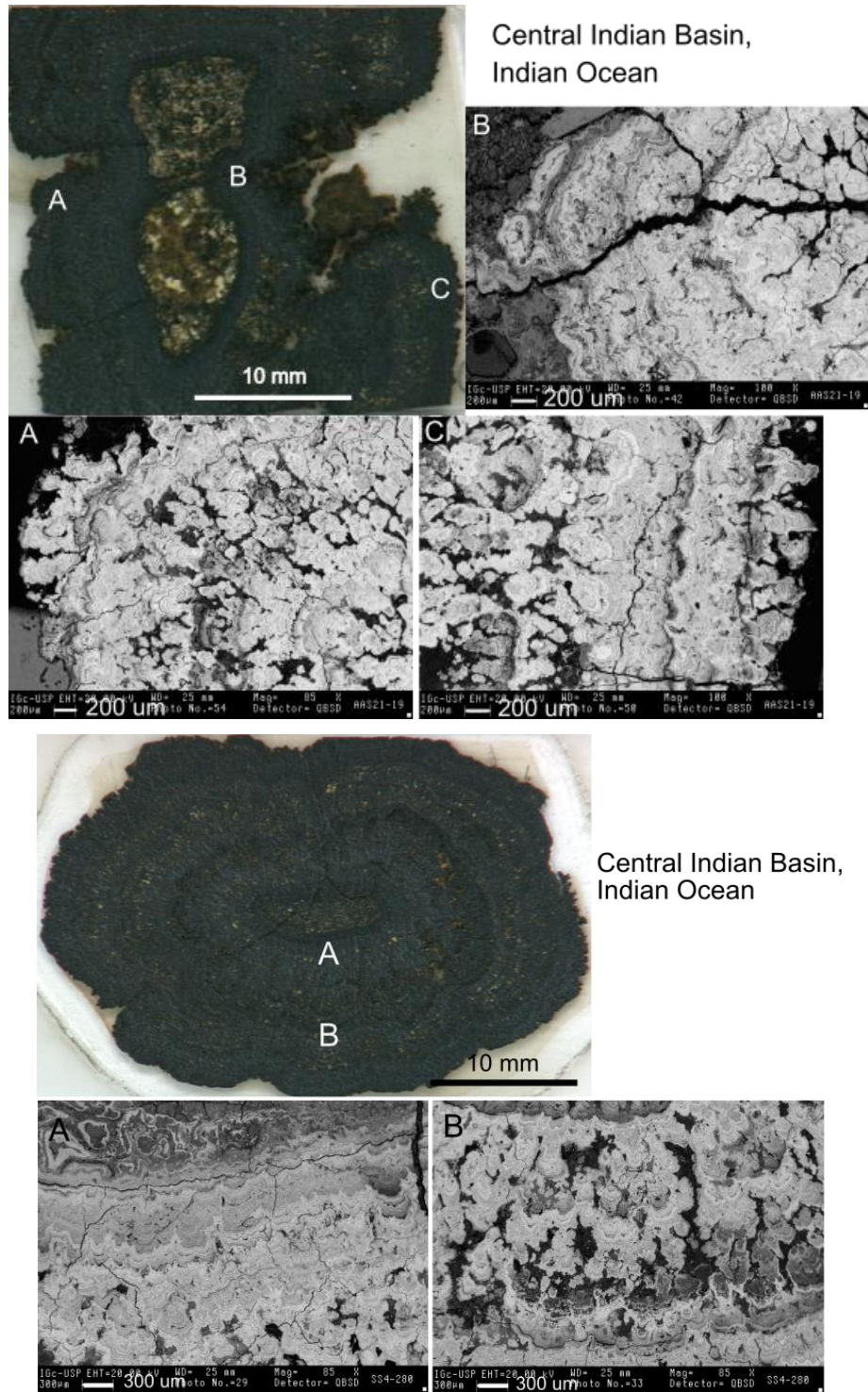


Figure 14 Polished sections of nodules AAS21-19 and SS4-280 with their layer textures viewed under SEM – Secondary Electron.

Table 5 Summary of the morphological features of nodules from the Central Indian Basin, Indian Ocean.

	AAS21-17	AAS21-19	AAS40	SS4-280	F8
Nodule size (cm)	6.5 x 4 x 3.5	4.5 x 4 x 3	5 x 3.5 x 3	4 x 3 x 3	3 x 3 x 2.5
Shape	ellipsoidal	spheroidal	ellipsoidal	spheroidal	faceted
Surface texture	rough	rough	rough	rough-smooth	smooth
Nucleus	polinucleated	polinucleated	polinucleated	mononucleated	-
Nucleus/Nodules ratio	50%	40%	50%	10%	-
Internal layering	yes, highly variable	yes, highly variable	yes, highly variable	yes, highly variable	-
Layer thickness					
Layer Texture	alternated between dendritic, massive and botryoidal	-			

Nodules from the CIB are composed mainly by Mn, Fe, Cu, Ni, Co, Zn, Ca, Ti, Ce, K and Sr and show similar chemical characteristics (table 6 and 7). Both nodules AAS21-19 (figure 15) and SS4-280 (figure 16) show very variable Mn/Fe ratios, between 0.5 and 10, with the lowest values measured in nuclei and in the layers around them. Cu and Ni are the more abundant metals after Mn and Fe and vary similarly to Mn. Co and Ti are generally close to detection limit, which results in very noisy signals. However, the signals get stronger where Fe abundance is higher.

Table 6 Mean and standard deviation of chemical elements measured by μ -XRF in counts and LA-ICP-MS in % and ppm in sample AAS21-19.

μ -XRF	Mean	Std deviation	LA-ICP-MS	n=124	Mean	Std deviation
Mn	23903.72	15164	Mn	%	42.68	19.23
Fe	2795.14	1638.99	Si	%	5	2.79
Cu	665.64	354.78	Ca	%	1.58	0.75
Ni	542.24	282.6	K	%	1.31	0.46
Zn	186.22	179.78	Ni	ppm	12298.91	7654.93
Ce	87.57	54.32	Cu	ppm	11658.03	6731.24
Ca	37.9	38.26	Zn	ppm	3578.35	2687.49
Ti	30.9	34.99	Ti	ppm	2542.8	2599.83
Co	25.42	46	Co	ppm	1395.26	1693.19
Sr	3.14	4.58	Sr	ppm	595.47	405.06
K	2.16	7.52	REY	ppm	521.39	473.7
Mn/Fe	10.68	8.86	Ce	ppm	289.55	372.47

Table 7 Mean and standard deviation of chemical elements measured by μ -XRF in counts and LA-ICP-MS in % and ppm in sample SS4-280.

μ -XRF	Mean	Std deviation	LA-ICP-MS	n=102	Mean	Std deviation
Mn	11361.45	2019.03	Mn	%	38.2	16.5
Fe	2486.87	823.92	Si	%	6.14	3.57
Cu	757.08	233.57	Ca	%	1.84	0.67
Ni	498.79	121.28	K	%	1.1	0.29
Zn	34.35	19.05	Cu	ppm	22839.21	11124.88
Ca	27.5	31.02	Ni	ppm	17314.7	8631.43
Ti	14.81	42.19	Zn	ppm	2490.52	1334.74
Co	14.09	21.56	Ti	ppm	2155.31	1301.48
Sr	1.34	1.26	Co	ppm	1248.95	519.33
Ce	0.6	1.11	Sr	ppm	652.15	265.6
K	0	0	REY	ppm	476.93	240.48
Mn/Fe	5.13	2.04	Ce	ppm	404.94	233.6

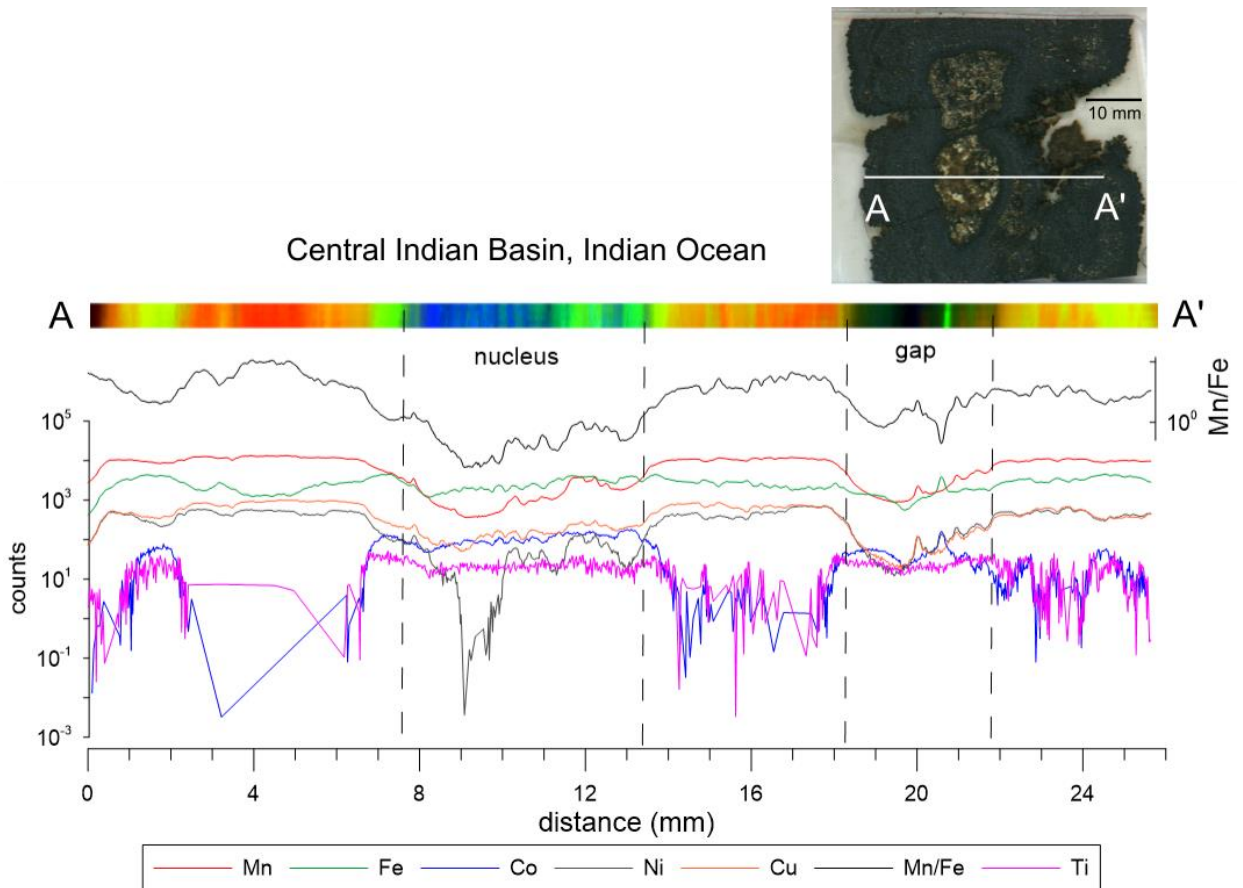


Figure 15 (a) Sample AAS21-19 from the Central Indian Ocean, (b) μ -XRF measurements of elemental composition along the transect (A-A'). (c) Color map of Mn (red), Fe (green) and K (blue).

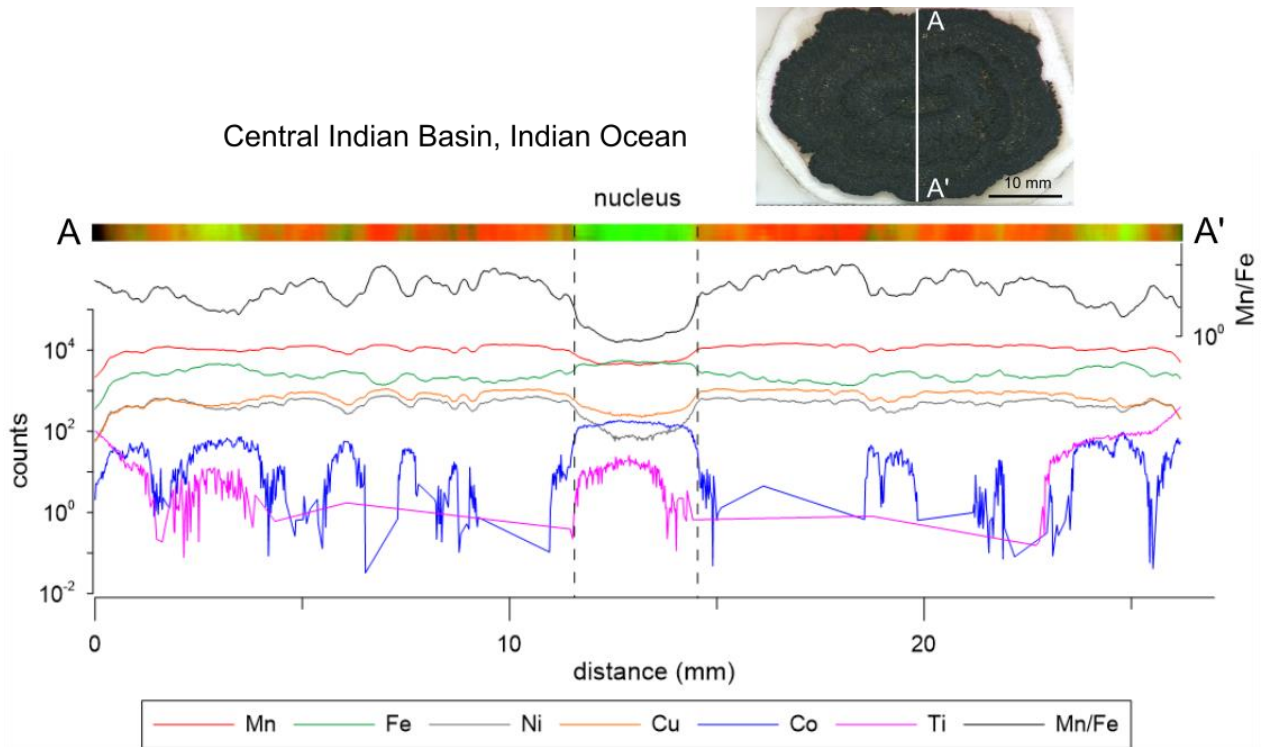


Figure 16 (a) Sample SS4-280 from the Central Indian Ocean, (b) μ -XRF measurements of elemental composition along the transect (A-A'). (c) Color map of Mn (red) and Fe (green).

LA-ICP-MS data shows that Mn varies across both nodules in concert with Cu (figures 17 and 18). Nodule SS4-280, however, presents a higher variability for all the elements. Si shows a behavior opposite to Mn in both nodules, while Ti and REE are neither concordant nor opposite to Mn.

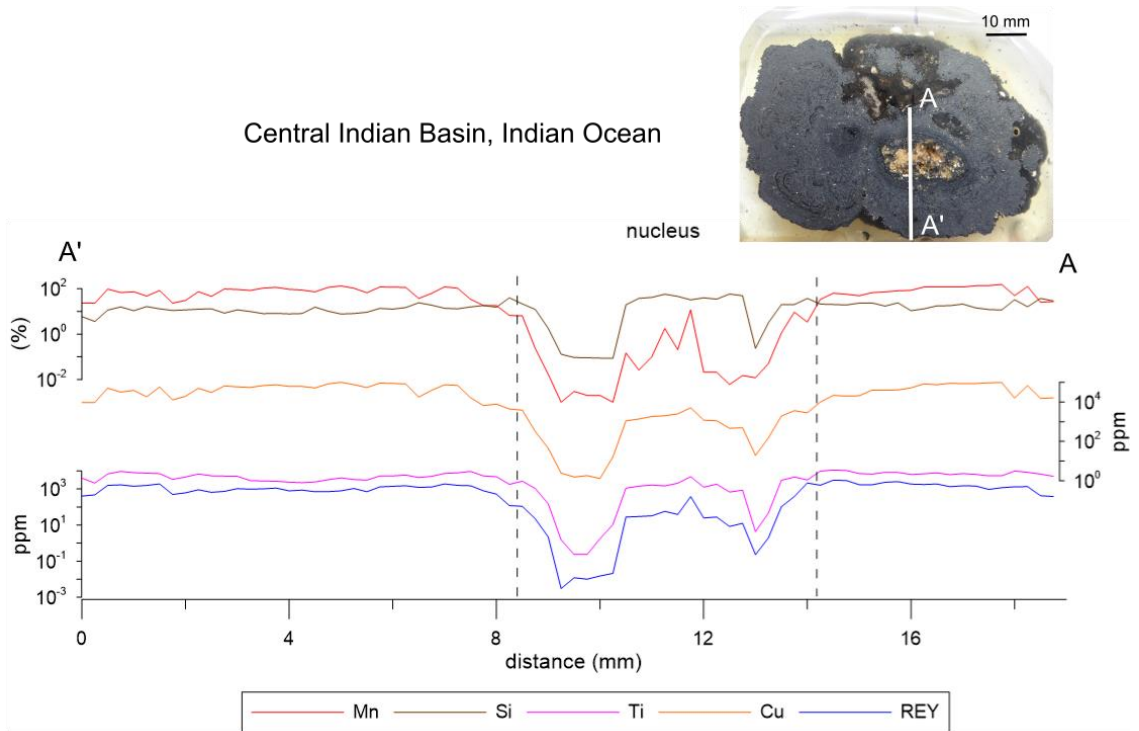


Figure 17 LA-ICP-MS elemental composition along the transect (A-A') in nodule AAS21-19 (Central Indian Basin, Indian Ocean).

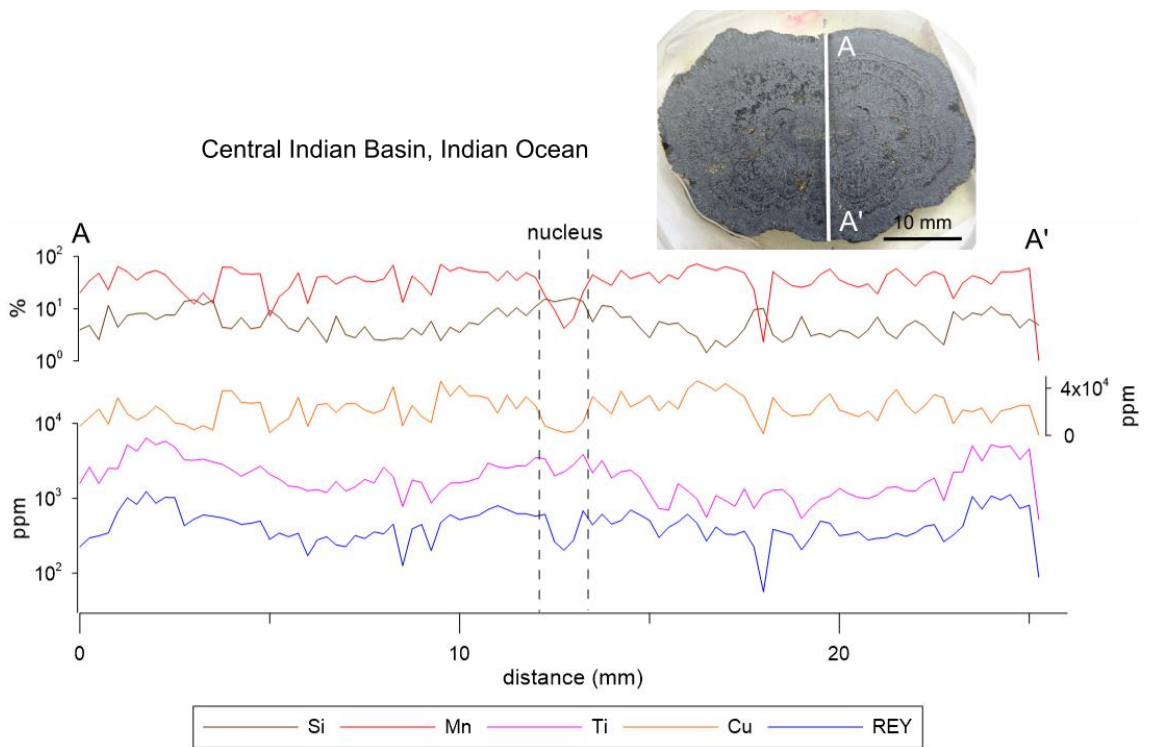


Figure 18 LA-ICP-MS elemental composition along the transect (A-A') in nodule SS4-280 (Central Indian Basin, Indian Ocean).

Finally, XANES spectra for nodule SS4-280 from the Central Indian Basin present the highest similarity (first derivative position at the energy axis) with the standard Mn_3O_4 and $FeOOH$ at the three points measured (figure 19).

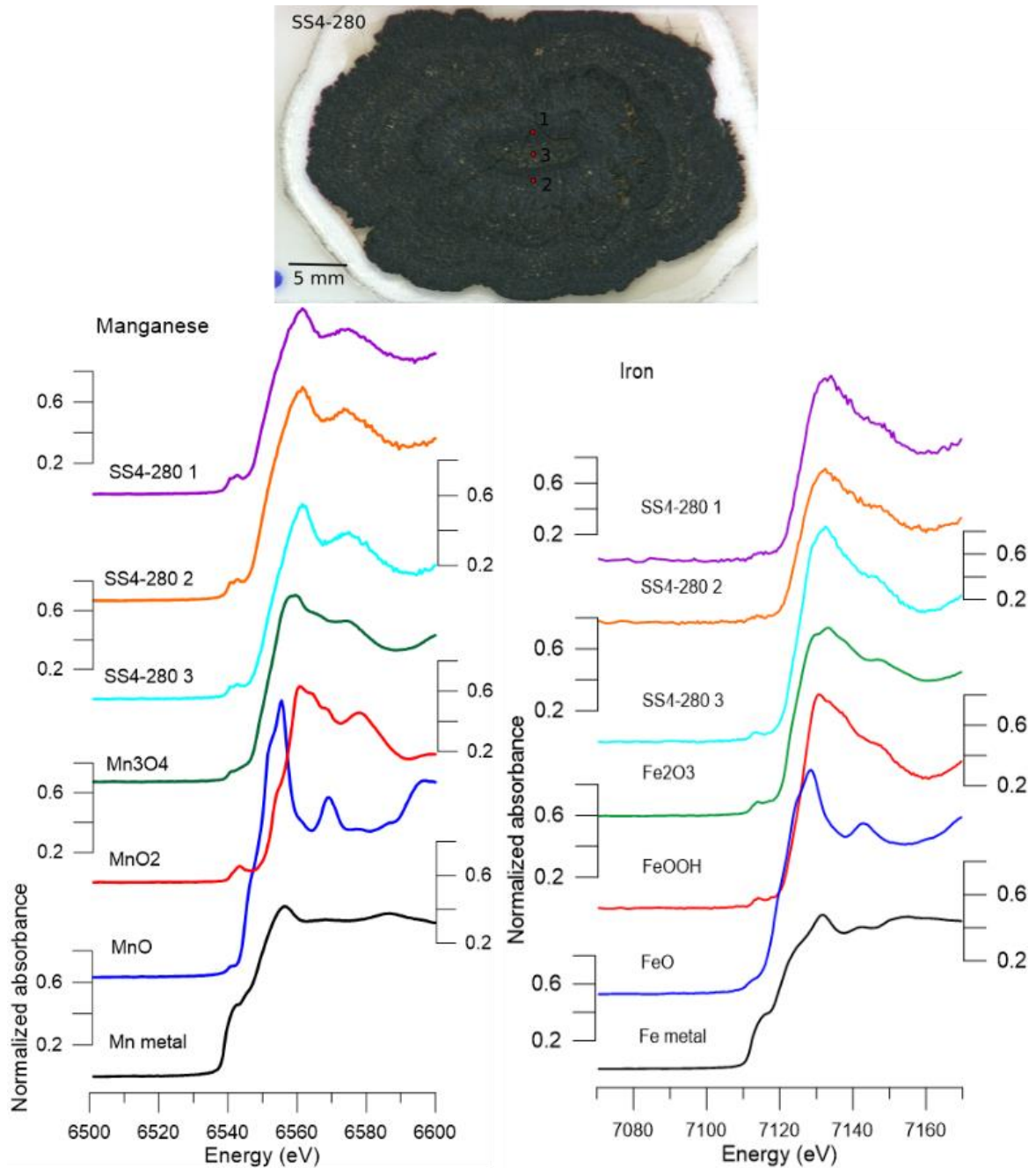


Figure 19 Location of the X-ray Absorption Near Edge Spectroscopy (XANES) measurements on sample SS4-280 and the curves for standards and sample SS4-280 points for (A) Mn and (B) Fe.

5.3. Mascarene Basin

Nodules from the Mascarene Basin are, on average, 4 cm long and strongly spheroidal (SK35-26 and SK35-27) or elongate (SK35-24) (figures 20). Their surface texture is smooth and homogeneous on all sides (figure 21). Some of them results from clustering of two or more smaller nodules (SK35-26 and SK35-27), the surface of which is also characterized by micro botryoides. Biological structures are absent on the spheroidal specimens.

CT tomography revealed that nodule SK35-24 comprehends an elongated nucleus which occupies most of the nodule volume (up to 80%), with a thin oxide layer (figure 22). In contrast, nodules SK35-26 and SK35-27 present small nuclei (22 to 40% of the total volume) and thick ferromanganese layers. Both are the result of the clustering of two or more nodules, and it is possible to identify the layer grown after the clustering. CT tomography shows that the MB nodules are internally homogeneous, with no density contrast between the layers.



Figure 20 Nodules from the Mascarene Basin.

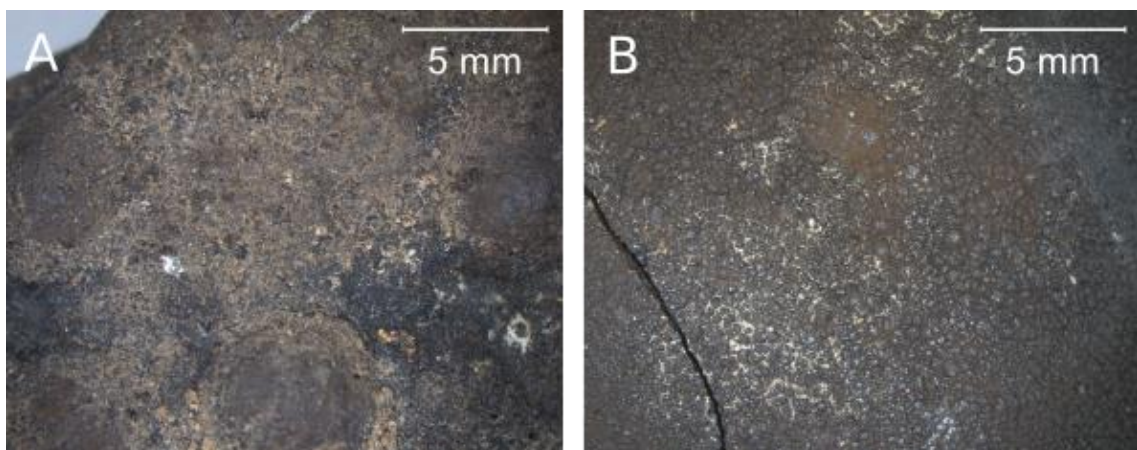


Figure 21 Surface texture of nodules SK35-24 and SK35-26 from the Mascarene Basin.

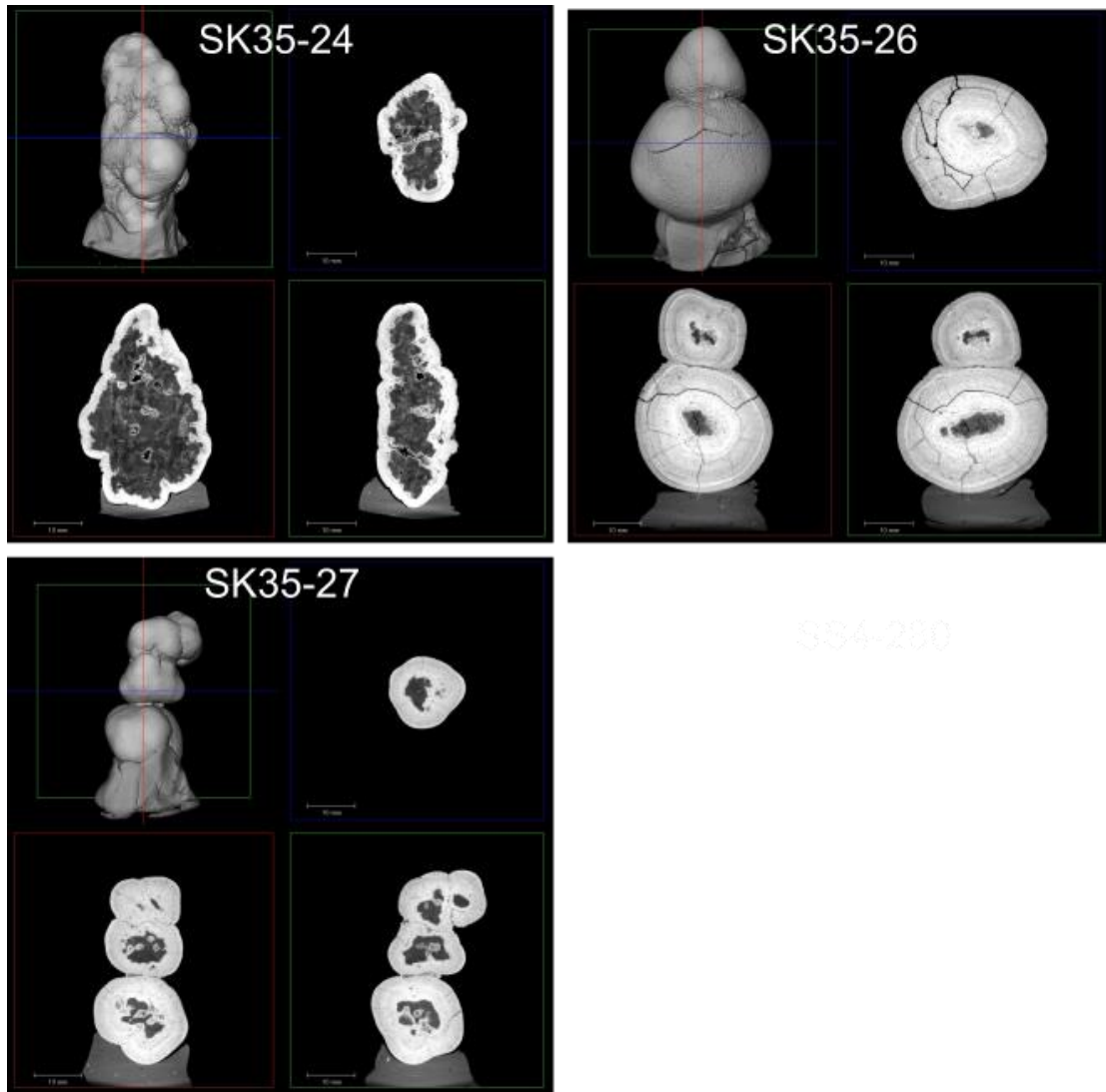
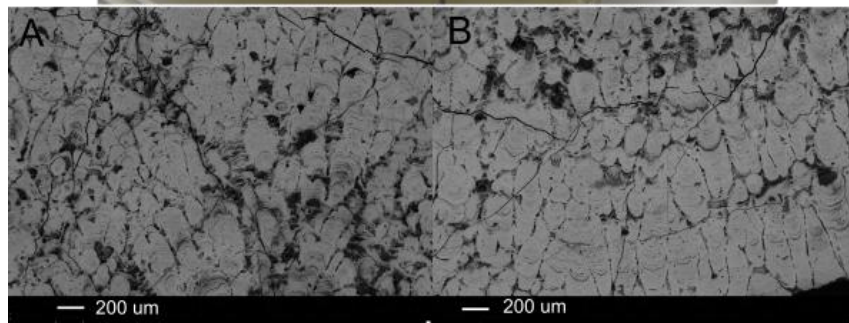
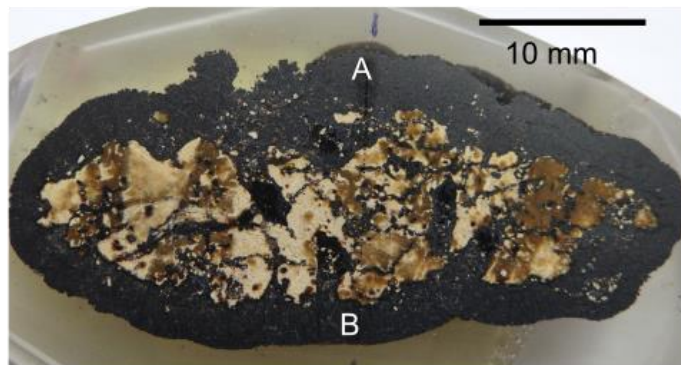


Figure 22 CT Tomography of the exterior and internal parts of nodules from the Mascarene Basin.

SEM micrographs enabled the classification of the layers texture as columnar across the entire nodule (figure 23), following the description of HALBACH et al. (1981). Based on the variability of the grey tones, layer thickness varies between 0.2 and 0.5 mm. A summary of the morphological features of the nodules from MB are presented in table 8.

Mascarene Basin, western Indian Ocean



Mascarene Basin, western Indian Ocean

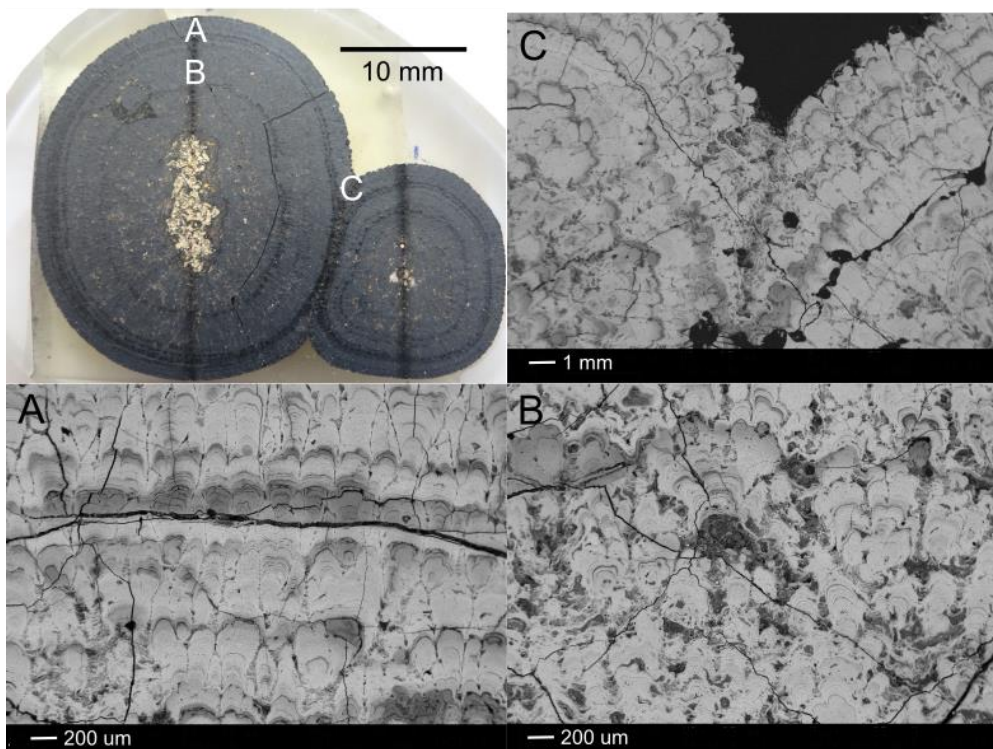


Figure 23 Polished section of nodules SK35-24 and SK35-26 and layers texture viewed by SEM – Secondary Electron.

Table 8 Morphological features of nodules from the Mascarene Basin, western Indian Ocean.

	SK35-24	SK35-26	SK35-27
Nodule size (cm)	two nodules of 5 x 3 x 3 and 4 x 3 x 3	4 x 3 x 3	two nodules of 4 x 2 x 2 and 2 x 1.5 x 1.5
Shape	ellipsoidal	cluster of two spheroidal nodules	cluster of up to 4 spheroidal nodules
Surface texture	smooth	smooth	smooth
Nucleus	mononucleated	binucleated	up to 4 nuclei
Nodule/Nucleus ratio	80%	20%	40%
Internal layering	absent	weak	weak
Thickness of layers	no layering	0.2 - 0.5 mm	-
Texture of layers	columnar	columnar	-

The chemical composition of the nodules from the MB is also very variable within each nodule, as indicated by the high standard deviations of most of the chemical elements measured by both μ -XRF and LA-ICP-MS (tables 9 and 10). However, the nodules from the MB differ clearly from the CCZ and CIB because they exhibit Mn/Fe ratios closer to 1 over most of their length (figures 24 and 25). They also differ from the CCZ and the CIB nodules in that they are significantly enriched in Ti and Co which, instead of Cu and Ni, are the most abundant elements after Mn and Fe.

Table 9 Mean and standard deviation of chemical elements measured by μ -XRF in counts and LA-ICP-MS in % and ppm in sample SK35-24.

μ -XRF	Mean	Std deviation	LA-ICP-MS	n=68	Mean	Std deviation
Fe	13507.74	3296.47	Si	%	31.85	15.2
Mn	10876.3	3531.45	Mn	%	30.8	39.22
Co	447.94	100.11	Ca	%	3.75	3.65
Ti	281.6	62.95	K	%	3.44	2.38
Ca	174.93	52.04	Ti	ppm	21512.13	19932.88
Ni	20.41	24.33	Co	ppm	6419.2	8718.44
K	6.58	18.36	Ni	ppm	4419.8	5162.82
Cu	5.14	9.34	Ce	ppm	3394.87	4160.74
Ce	1.58	4.63	Cu	ppm	2670.02	2288.27
Sr	0.42	1.8	Sr	ppm	2206.23	2761.69
Zn	0	0	REY	ppm	1502.35	1659.14
Mn/Fe	0.83	0.24				

Table 10 Mean and standard deviation of chemical elements measured by μ -XRF in counts and LA-ICP-MS in % and ppm in sample SK35-26.

μ -XRF	Mean	Std deviation	LA-ICP-MS	n=126	Mean	Std deviation
Fe	9263.96	4605.37	Mn	%	19.01	13.67
Mn	8402.64	4416.71	Si	%	10.06	2.98
Ti	386.89	223.37	Ca	%	2.62	1.3
Co	354.63	163.68	K	%	1.03	0.45
Ca	148.94	68	Ti	ppm	19826.22	14383.95
Ni	48.12	44.92	Co	ppm	3883.38	3274.52
Ce	22.95	22.92	Ni	ppm	3021.61	2247.8
Cu	2.54	7.58	Ce	ppm	2407.49	1775.41
K	0.68	5.35	Cu	ppm	1620.15	958.89
Sr	0.3	1.11	Sr	ppm	1449.22	919.17
Zn	0.27	1.77	REY	ppm	1129.66	766.13
Mn/Fe	0.93	0.26	Zn	ppm	945.59	562.84

LA-ICP-MS analysis shows that Ti concentration is higher than that of Cu (figures 26 and 27). REE are twice or three times more abundant than in nodules from the CCZ and CIB. The curves of abundance of Mn, Ti, Cu, Co and REE are relatively similar. Si is the only element that presents a different pattern, sometimes even opposite to the other elements.

The elemental composition obtained by both μ -XRF and LA-ICP-MS resulted in an apparent internal symmetry in the nodules from the MB.

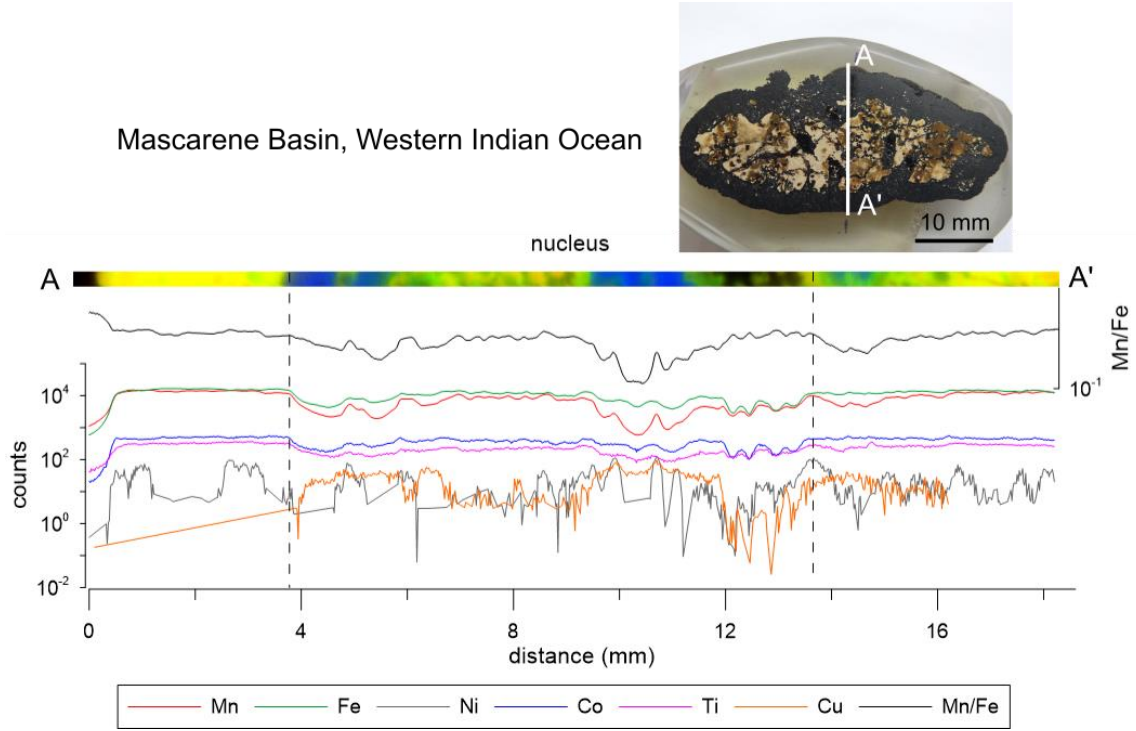


Figure 24 Sample SK35-24 from the Mascarene Basin, western Indian Ocean. (b) μ -XRF measurements of elemental composition along the transect (A-A'). (c) Color map of Mn (red), Fe (green) and K (blue).

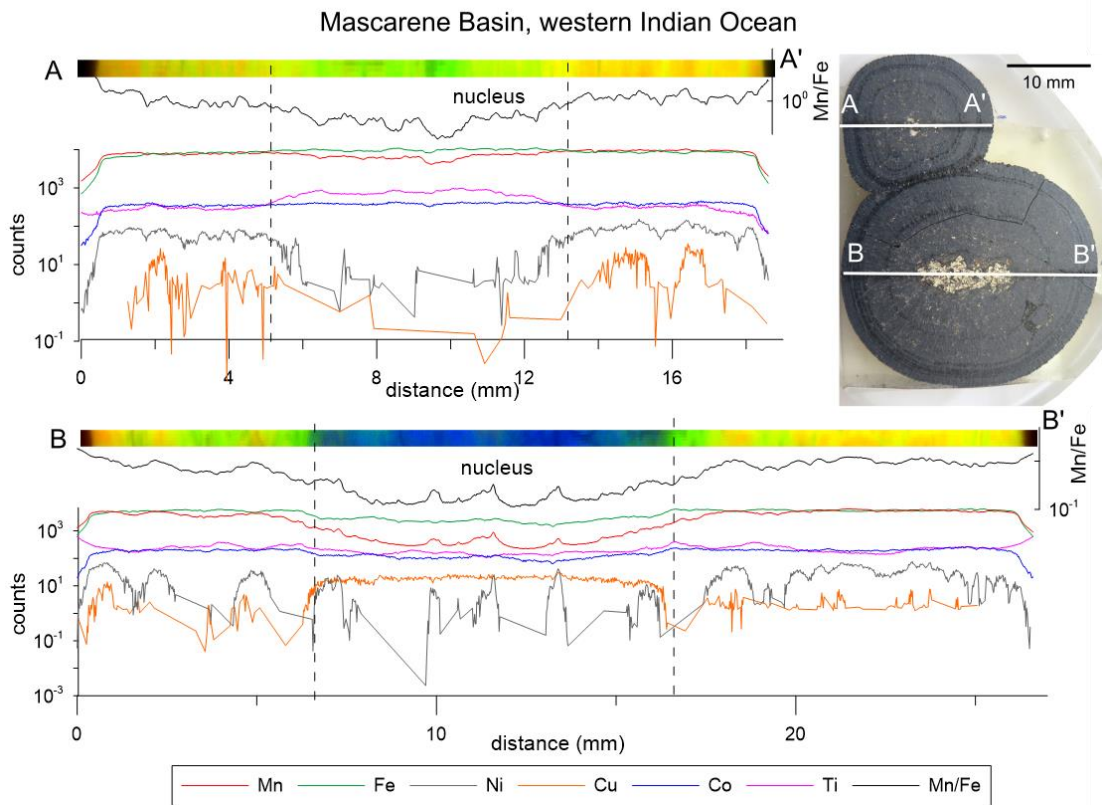


Figure 25 Sample SK35-26 from the Mascarene Basin, western Indian Ocean. (b) μ -XRF measurements of elemental composition along the transect (A-A' and B-B'). (c) Color map of Mn (red), Fe (green) and K (blue).

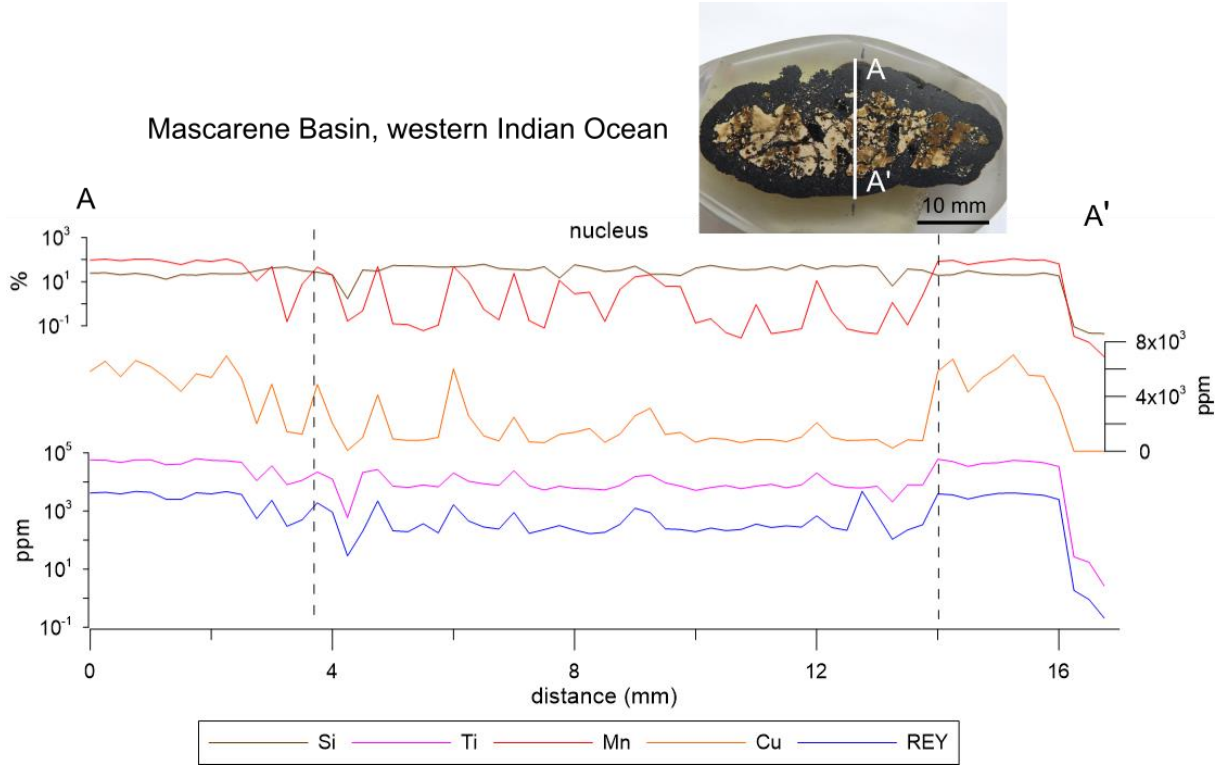


Figure 26 LA-ICP-MS elemental composition along the transect (A-A') in nodule SK35-24 from the Mascarene Basin, western Indian Ocean.

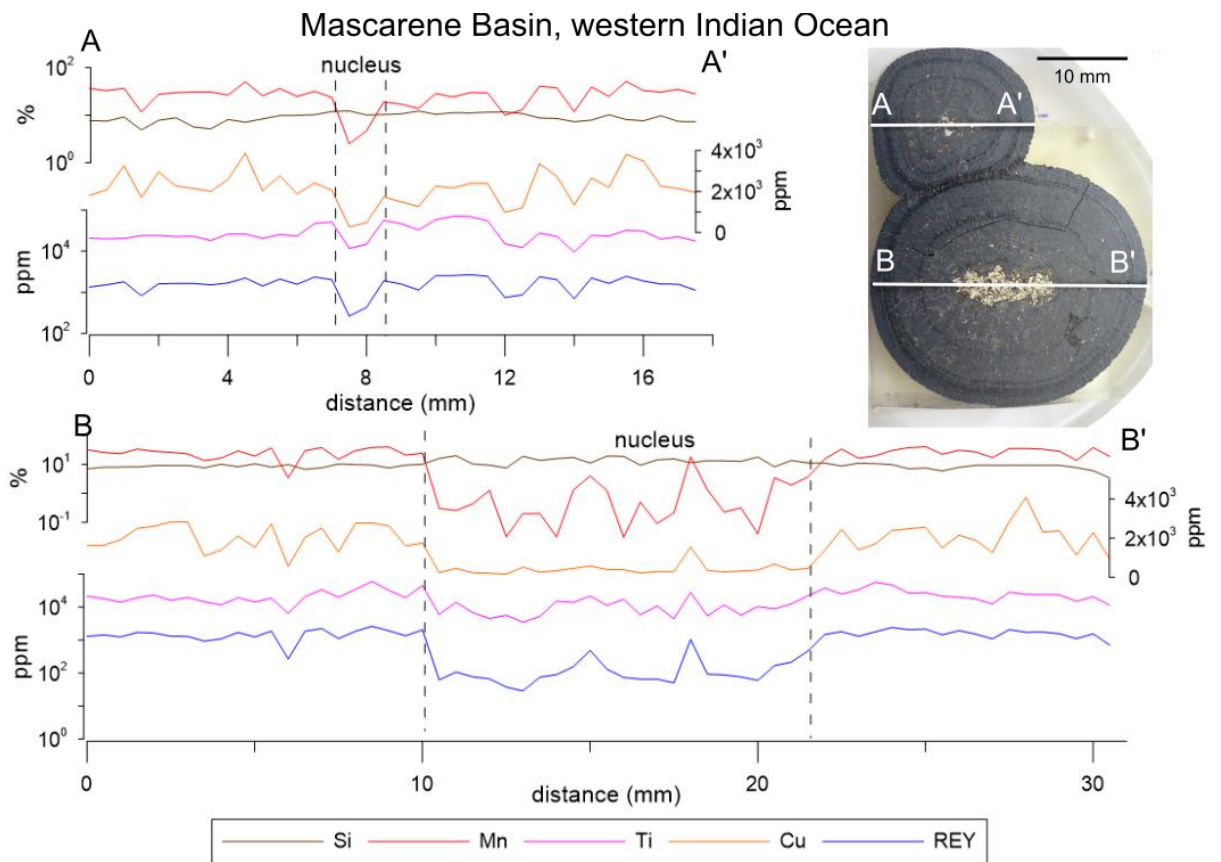


Figure 27 LA-ICP-MS elemental composition along the transects (A-A' and B-B') in nodule SK35-26 from the Mascarene Basin, western Indian Ocean.

XANES spectra measured in points 1, 2 and 3 in nodule SK35-26 (figure 28) showed the highest similarity with the spectrum of the standards Mn_3O_4 and MnO_2 and, for Fe, with the standards FeOOH and Fe_2O_3 .

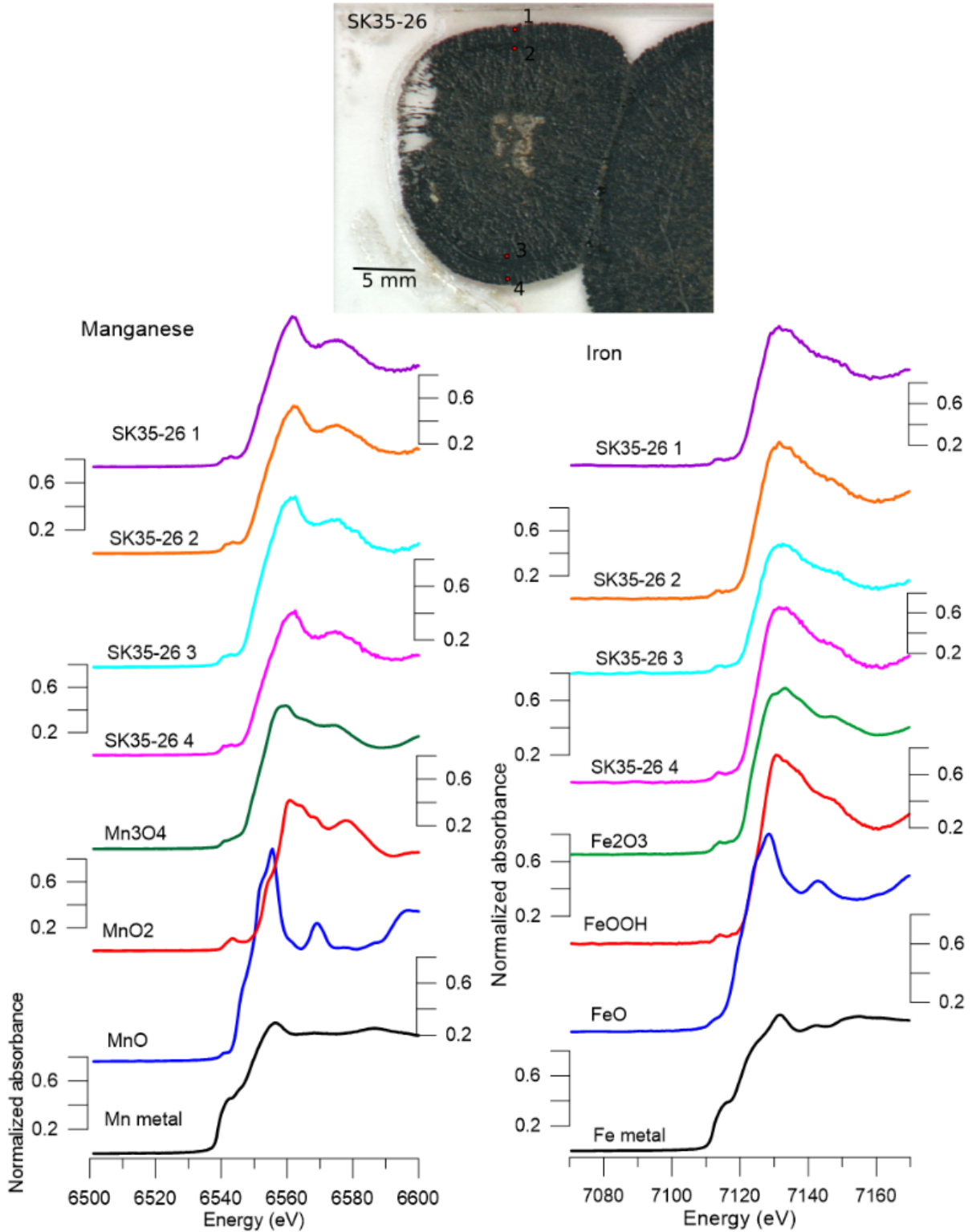


Figure 28 Location of the X-ray Absorption Near Edge Spectroscopy (XANES) measurements and the curves for Mn and Fe standards and points on sample SK35-26.

5.4. Rio Grande Rise

The nodule from the Rio Grande Rise is 2 cm long, spheroidal, with a micro botryoidal surface texture surrounded by orange material (figure 29). One of its sides is covered by fine calcareous tests (figure 29D).

The RGR coated pebble is made up by a thin oxide layer formed around the nucleus, which represents almost 90% of the nodule's volume (figure 30). Changes in the grey scale suggest that the oxide layer is generally 0.2 mm thick, reaching 0.7 mm on one side (figure 31). A single layer of variable thickness – 0.5 to 0.3 mm – surrounds the nucleus.

The texture of the thicker portion of the layers is laminated to botryoidal, while in the thinner portion it is dendritic (figure 31). The morphological features of the RGR coated pebble are summarized in table 11.

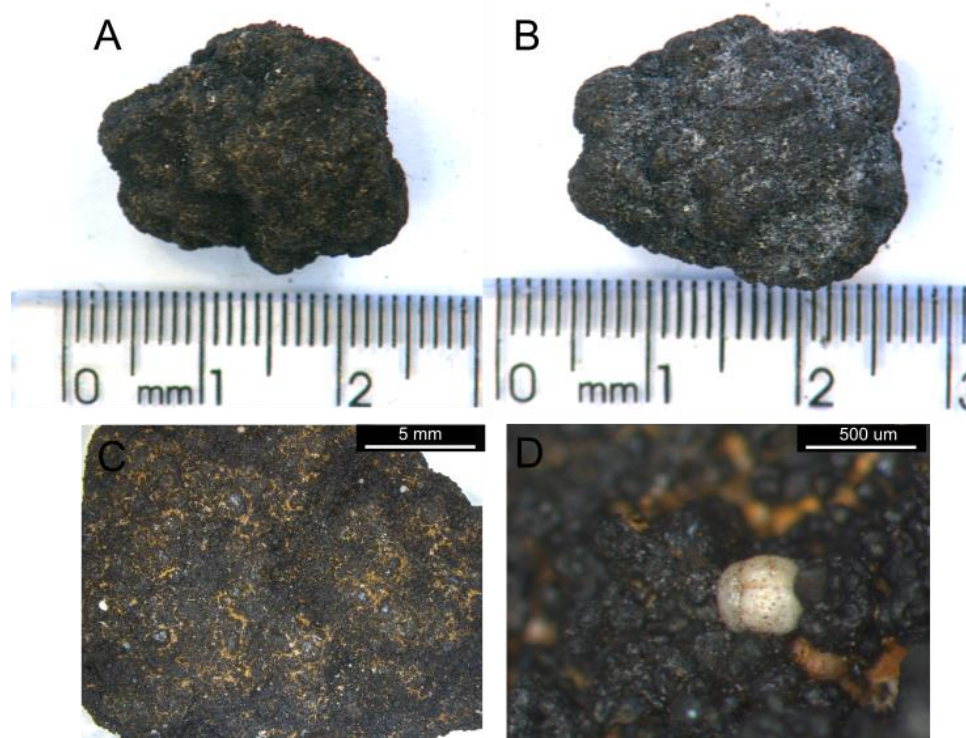


Figure 29 Coated pebble from Rio Grande Rise (RGR); (A) bottom side and (B) top side; (C) surface texture on opposite sides; (D) foraminifer attached to the nodule surface.

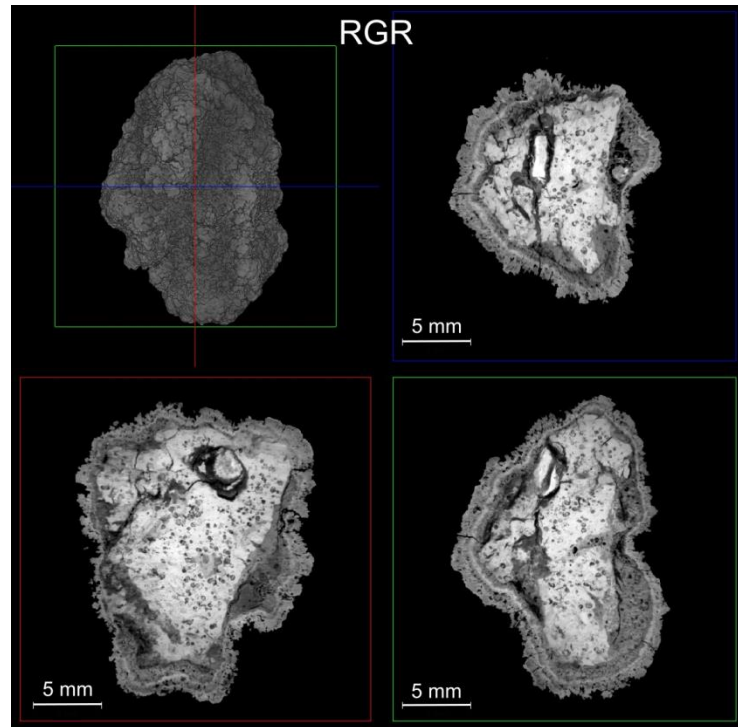


Figure 30 Tomography of nodules from the Mascarene Basin from the exterior and slices on three dimensions.

Rio Grande Rise, south Atlantic

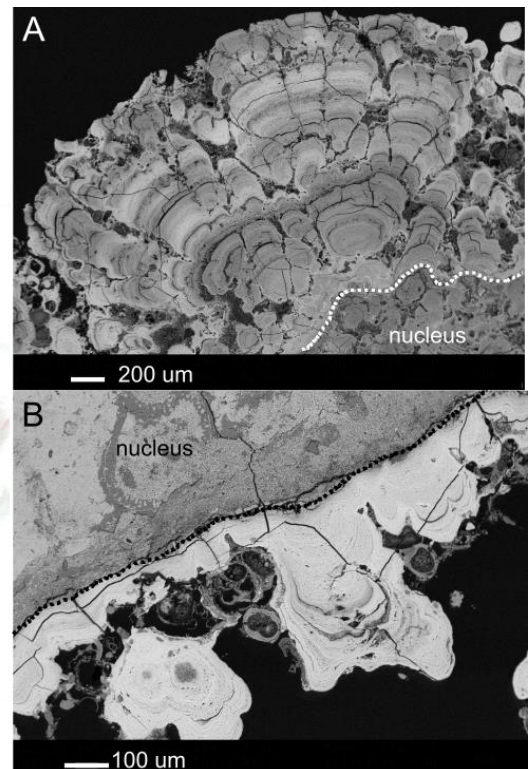
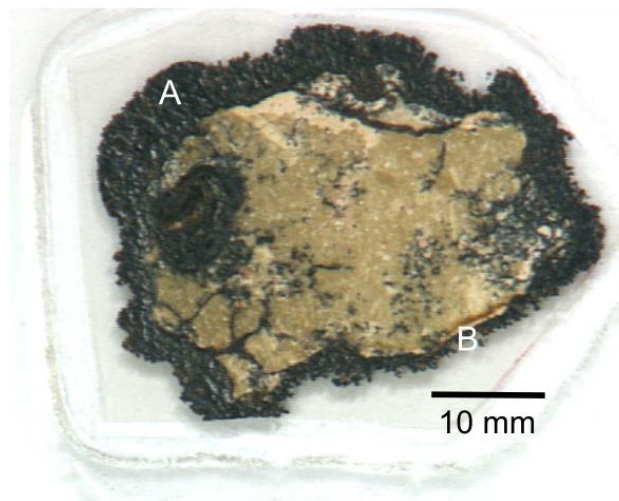


Figure 31 Polished section of RGR and micrographs of Scanning Electron Microscopy – Secondary Electron showing the layers texture. The Dashed lines mark the nucleus – oxides transition.

Table 11 Morphological features of coated pebble from the Rio Grande Rise, South Atlantic.

RGR	
Nodule dimensions	2 x 2 x 1 cm
Shape	spheroidal
Surface texture	microbotryoidal
Nucleus	one nucleus
Nodule/Nucleus ratio	90%
Internal layering	little variable
Thickness of layers	0.2 mm
Texture of layers	columnar - laminated

Several aspects previously described for the nodules from the others ocean basin are observed also in the RGR coated pebble. For example, the standard deviations of the concentrations of most of the chemical elements is high (table 12), often higher than the average concentration.

μ -XRF data show an average Fe concentration higher than those of Mn, while Co and Ti are the most abundant metals after Fe and Mn, like in the nodules from the Mascarene Basin. In order of abundance, the RGR coated pebble is composed of Fe, Mn, Ca, Co, Ti, Ni, K, Sr, Cu and Zn. The elemental abundance across a transect from the nodule's external surface to the nucleus show Mn/Fe ratio < 1 , as well as constant Fe, Mn, Ti and Co values (figure 32). Ni presents a noisy signal because of low concentration. The nucleus is enriched in Ca, as indicated by the color map, due to the presence of a high number of foraminiferal tests.

Table 12 Mean and standard deviation of chemical elements measured by μ -XRF in counts and LA-ICP-MS in % or ppm for RGR.

μ -XRF	Mean	Std deviation	LA-ICP-MS	n=24	Mean	Std deviation
Fe	937.48	1226.71	Ca	%	42.68	41.56
Mn	640.08	738.72	Mn	%	18.96	24.45
Ca	525.91	306.4	Si	%	13.66	7.56
Co	41.81	55.64	K	%	2.19	1.56
Ti	15.36	21.13	Ti	ppm	15345.92	15817.27
Ni	15.12	25.12	Co	ppm	7054.63	8710.1
K	14.57	9.56	Ni	ppm	4394.14	5896.1
Sr	3.17	2.03	REY	ppm	2894.46	1592.26
Cu	2.95	5.74	Sr	ppm	2873.4	1289.27
Zn	1.43	2.49	Ce	ppm	2034.59	2278.72
Ce	0	0.05	Cu	ppm	1449.62	1420.84
Mn/Fe	0.82	0.59	Zn	ppm	1091.54	1149.51

LA-ICP-MS results reveal that the coated pebble from RGR has the lowest Mn content of all the nodules studied (table 10). In contrast, the REE content is up to five times higher than in the nodules from the CCZ and CIB, and twice to three times higher than in the MB nodules. Transects 1 and 2, from the nodule's edge to the nucleus, present opposite behavior for the curves of Mn and Si concentrations, and similar behavior for the curves of Ti, Co, Cu and REE, even though in the first 0.4 mm of transect 1 the Ti curve diverges from the others (figure 33). Also, REE concentrations in transect 1 are higher than in transect 2.

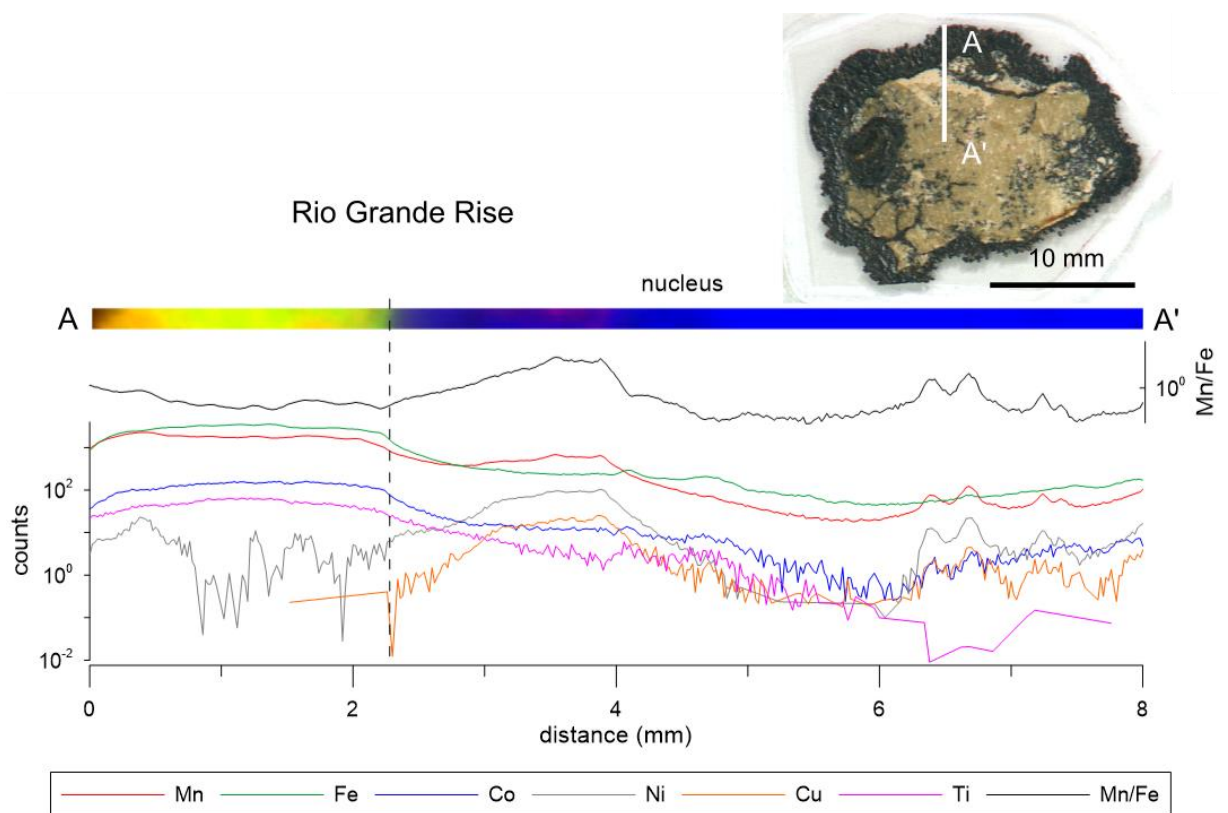


Figure 32 (a) Sample RGR from the Rio Grande Rise, southwest Atlantic Ocean. (b) μ -XRF measurements of elemental composition along the transect (A-A'). (c) Color map of Mn (red), Fe (green) and K (blue).

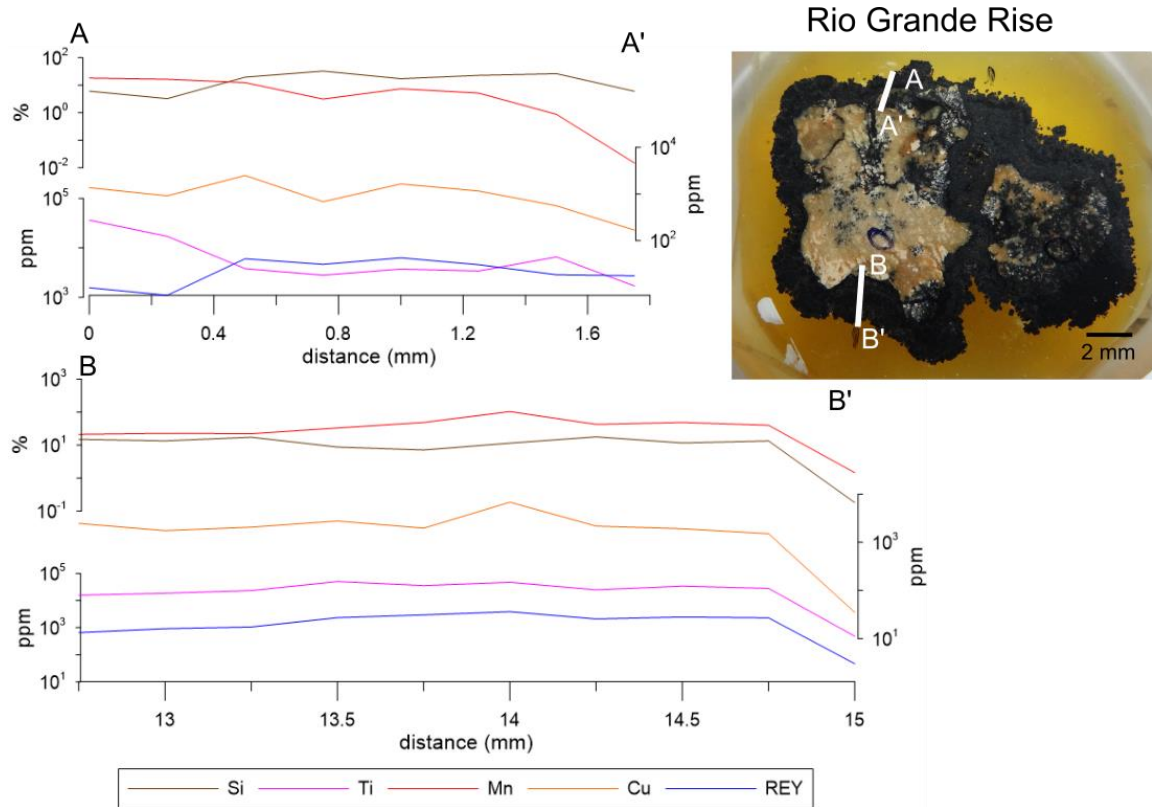


Figure 33 LA-ICP-MS elemental composition along the transects (A-A' and B-B') in coated pebble RGR from the Rio Grande Rise, southwest Atlantic Ocean.

XANES spectra for Mn in the coated pebble RGR show the highest similarity with the standard Mn_3O_4 at the three points measured. In the case of Fe, point 1 and 2 are similar to the $FeOOH$, while point 3 is more similar to Fe_2O_3 (figure 34).

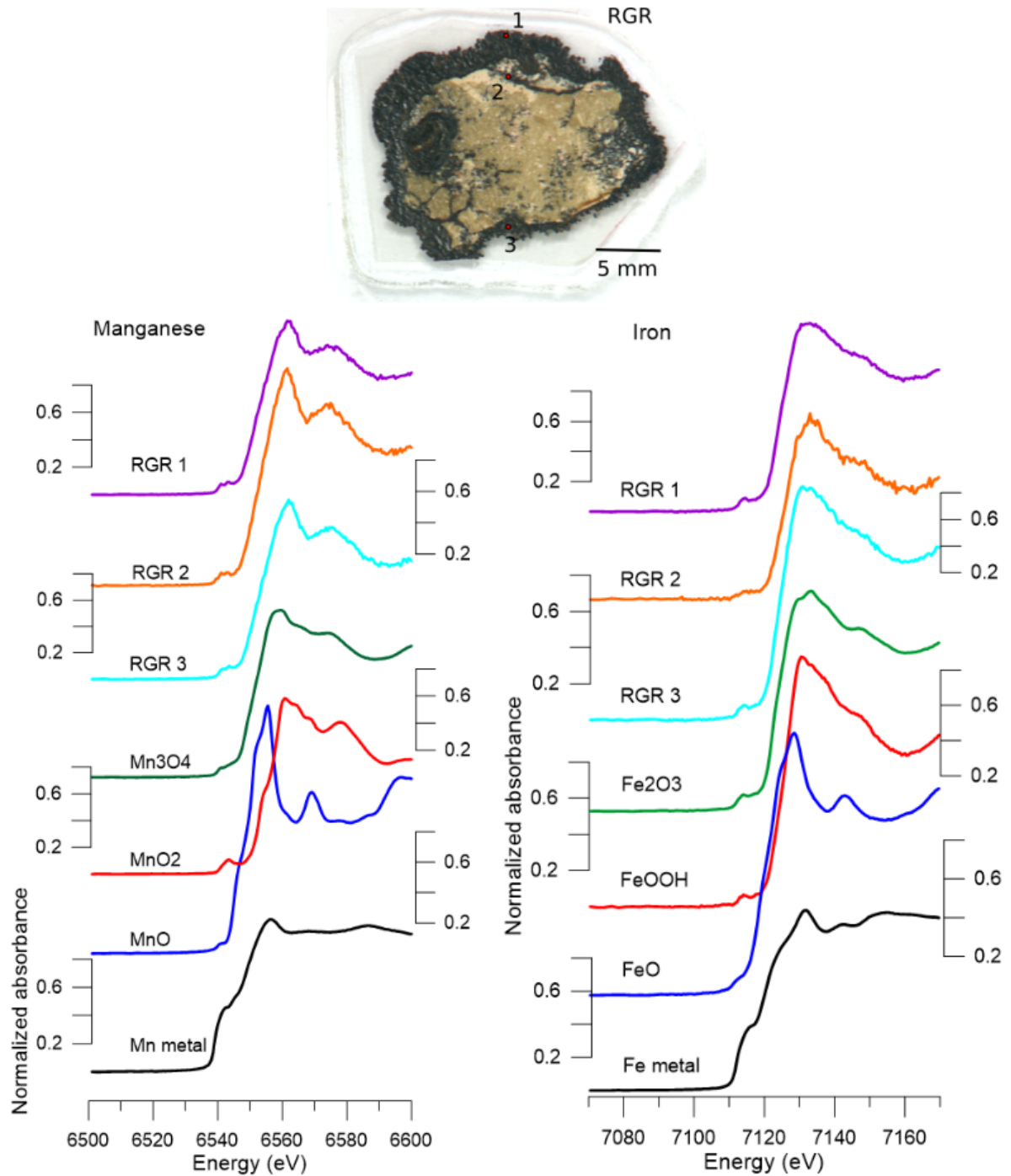


Figure 34 Location of the X-ray Absorption Near Edge Spectroscopy (XANES) measurements and the curves for Mn and Fe standards and points on sample RGR.

5.5. Statistical analysis

The Principal Component Analysis performed using the μ -XRF average concentrations of chemical elements shows that most of the chemical elements group together, excepting for Mn and Fe that are separated (figure 35). The two Principal

Components (PC1 and PC2) together explain 97.8% of the total variance of the data. The samples from the CCZ and the CIB are more influenced by Mn, Cu and Ni. On the other hand, the samples from the MB and the RGR are more influenced by Fe, Ca, Co and Ti.

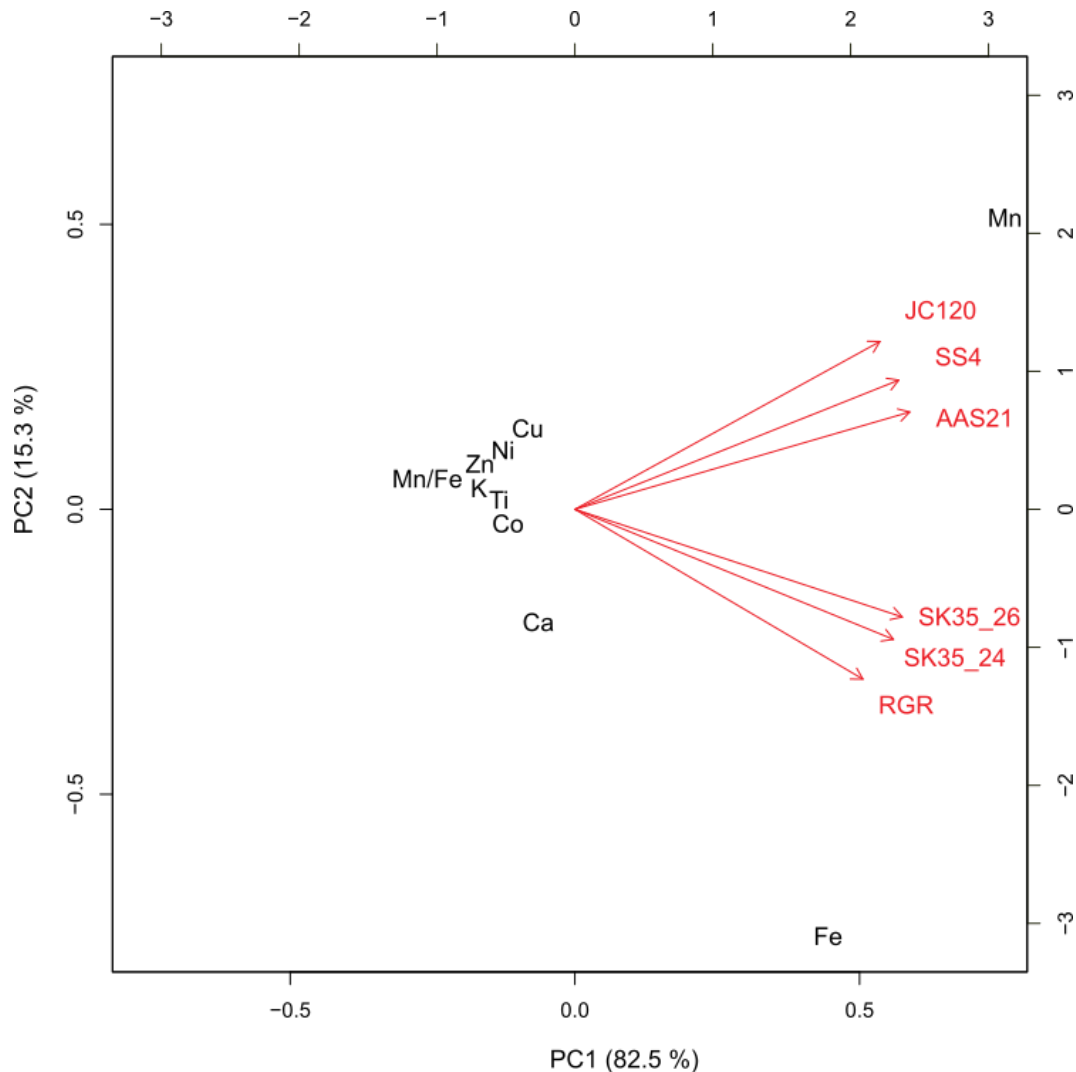


Figure 35 Principal Component Analysis calculated for the average values of the chemical elements for the μ -XRF data with the scores of each Principal Component. Total variance explained by the two components together is 97.8%.

The same analysis was applied for the LA-ICP-MS data and the Principal Components encountered were similar (figure 36). The nodules are segregated between those which are more influenced by Cu and Ni (nodules from the CCZ and CIB) and the ones which are more influenced by Ti and Co (nodules from the MB and RGR coated pebble). Mn appears as a non-influent element, however its measurement unit is % while Ni and Cu is expressed in ppm, which in absolute value Mn is minor than the values of Ni and Cu (for example, 10% of Mn compared to 10000 ppm of Ni).

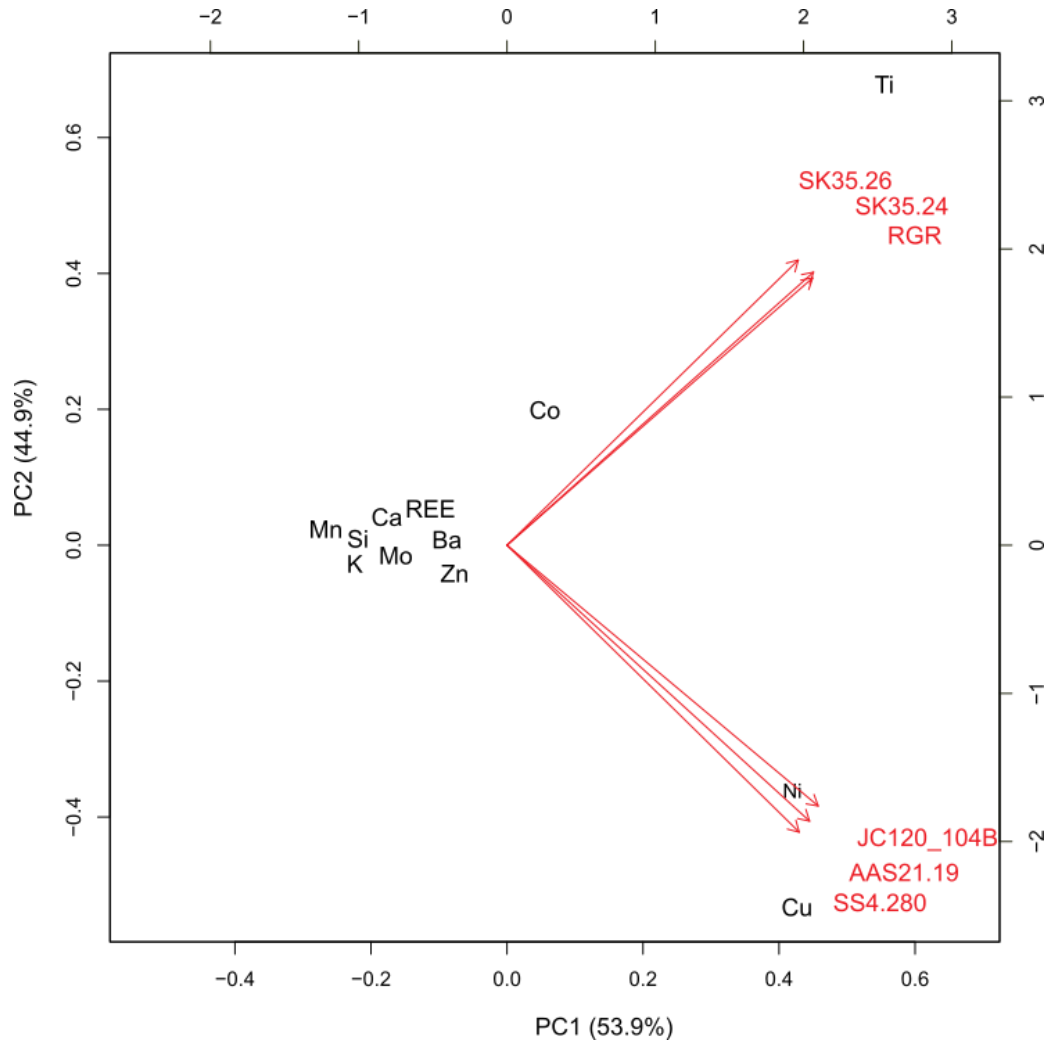


Figure 36 Principal Component Analysis calculated for the average values of the chemical elements for the LA-ICP-MS data with the scores of each Principal Component. Total variance explained by the two components together is 98.8%.

The statistical analyses reflect the pattern observed in the chemical composition of nodules studied, in which Mn, Ni and Cu are enriched in the nodules from the CCZ and CIB, whereas Fe, Co and Ti are enriched in nodules from the MB and coated pebble from the RGR.

6. DISCUSSION

6.1. Mechanisms of formation of polymetallic nodules

The nodules studied present similarities regarding their morphology and geochemistry, which give insights into the mechanisms of formation common to all the nodules.

Distinguishable concentric layers and high standard deviation of the elements concentration reveal that the accretion process does not happen always in the same way and at the same rate. The Mn/Fe ratio high variance indicates that the conditions of formation of nodules changed many times. Dymond et al. (1984) first evinced that the accretion process in nodules from the Equatorial Pacific Ocean is characterized by non-steady-state process.

The chemical composition is basically the same in all the nodules and is represented by 41 chemical elements from the dataset in this work, from Si to U (see Supplementary Material) recognized with a combination of different analytical techniques.

Mn and Fe are the dominant elements as usually occurs in nodules, once Mn and Fe oxides are the matrix material (HEIN; KOSCHINSKY, 2014). This seems to be true for the global ocean, including the recently recovered nodule from the Rio Grande Rise (this work).

Si, Ca and K are also found in high abundance in the nodules studied. However, Principal Component Analysis shows these elements are associated neither to the Mn mineral phase nor to Fe one. Si and K are known to come from detrital aluminosilicates, while Ca, Ba and Sr come from pelagic biogenic material. Both groups make up a detrital mineral phase incorporated during the nodules accretion (GLASBY; LI; SUN, 2013; HEIN; KOSCHINSKY, 2014). Finally, most of the trace metals (Cu, Ni, Co and Ti) can be split into those associated to the Mn mineral phase and those that are associated to the Fe one (see the PCA results, figure 35 and 36). This segregation is in agreement with many previous findings which show that some metals are preferably incorporated into the Mn oxide while others are incorporated into the Fe oxyhydroxide structure. Strong positive correlation between Mn and Ni, Cu and Zn was found in nodules from the CIB (PATTAN; PARTHIBAN, 2011). Mn oxides have the tendency to incorporate divalent cations like Ni^{2+} , Cu^{2+} and Zn^{2+} , whereas Fe oxyhydroxide tend to

incorporate anionic species like HPO_4^{2-} , HAsO_4^{2-} , HVO_4^{2-} , MoO_4^{2-} and WO_4^{2-} , as well as REE and Co^{3+} (GLASBY; LI; SUN, 2013).

It was not possible to evaluate the association between Fe and the REE because of the limitation on the LA-ICP-MS technique in not distinguishing Fe. Nevertheless, the most REE-enriched nodules correspond to the ones with higher Fe content and low Mn/Fe ratio, which are the ones from the Mascarene Basin and the Rio Grande Rise. These nodules are comparable to the hydrogenetic nodules of Cook Islands, which present high REE content (HEIN et al., 2015).

Most of the Mn oxide present in the nodules from the basins studied are composed of a mixture of Mn^{4+} and Mn^{3+} , revealing a high oxidation state for Mn. Glasby (2006) estimated that 98% of the Mn in deep sea nodules is Mn^{4+} . This is in agreement with the oxidation state of Mn in the three main Mn oxides present in nodules, namely vernadite, todorokite and birnessite (BURNS; BURNS, 1977). Mn^{2+} has also been found incorporated to lattice vacancies of phylломanganates when the Mn^{2+} upwards diffusion across the redox front is too high, but this chemical species was not found to be relevant in none of the samples measured in this study.

The presence of Mn species in the sediments comes from the organic matter diagenesis, in which Mn is reduced to Mn^{2+} and is released to the pore water in the suboxic sediment layer, together with Ni^{2+} , Cu^{2+} and Zn^{2+} (CHESTER, 2003). Mn^{2+} then migrates to the oxic layer by diffusion and is oxidized to Mn^{3+} and Mn^{4+} , precipitating as phylломanganates, which incorporate Ni^{2+} , Cu^{2+} and Zn^{2+} in their lattice vacancies (GLASBY, 2006). Suboxic diagenesis precipitation of Mn may happen and results on a high flux of Mn^{2+} into the Mn oxide structure (DYMOND et al., 1984; WEGORZEWSKI; KUHN, 2014). The suboxic diagenesis nodules accretion occurs when the redox front is closer to the sediment-water interface, where the nodules are generally found. Suboxic diagenesis results Mn/Fe ratios up to 500 and low Ni and Cu contents (BLÖTTE et al., 2015). Such conditions were not observed in the nodules studied, thus this process seems to be not relevant for the formation of the nodules considered in this study.

Fe is present in nodules generally as oxyhydroxides FeOOH (MARCUS et al., 2015). However, hematite (Fe_2O_3) was found in small content in nodules (SHIRAISHI et al., 2016). Also, oxyhydroxides can change into hematite by dissolution and re-precipitation, or by solid state transformation (LU et al., 2011). Therefore, the presence of Fe_2O_3 in some of the nodules may be explained by transformation of oxyhydroxides into hematite.

Based on the above considerations, oxic diagenesis and hydrogenetic accretion are possibly the dominant processes of formation for the nodules studied.

6.2. Characterization of the formation process in the different ocean basins

The morphological and geochemical features of the nodules from the CCZ are similar to those of the nodules from the CIB, while the nodules from the MB are similar to the coated pebble from the RGR (table 13 and figure 37).

The relative elemental abundance is different for each ocean region. Cu and Ni are enriched in nodules from the CCZ and the CIB. On the other hand, Co and Ti are enriched in nodules from the MB and coated pebble from the RGR. It is not coincidence that this happens where the Mn/Fe is < 1 . This information corroborates the idea that diagenetic deposits are enriched in Mn, Cu, Ni, Zn and Mo, while hydrogenetic deposits are enriched in Fe, Co, Ti and REE (HEIN; KOSCHINSKY, 2014).

Table 13 Polymetallic nodules morphological aspects summary.

	CCZ	CIB	MB	RGR
Nodule dimensions				
1-5 cm		X	x	x
5-10 cm	x			
Shape				
Discoidal	x			
Subrounded		X		x
Rounded			x	
Surface texture				
Rough	x	X		
Botryoidal	x	X		
Microbotryoidal – smooth			x	x
Nucleus				
Ancient deposit	x			
One sedimentary rock			x	x
Many sedimentary rocks		X		
Nucleus/Nodules ratio				
0-50%		X	x	
50-100%	not applied		x	x
Internal layering				

highly variable	x	X		
little variable			x	x
Thickness of layers				
0.2 mm			x	x
2 mm	x			
Texture of layers				
Massive	x	X		
Dendritic	x	X		
Botryoidal	x	X		
Columnar			x	x
Laminated				x

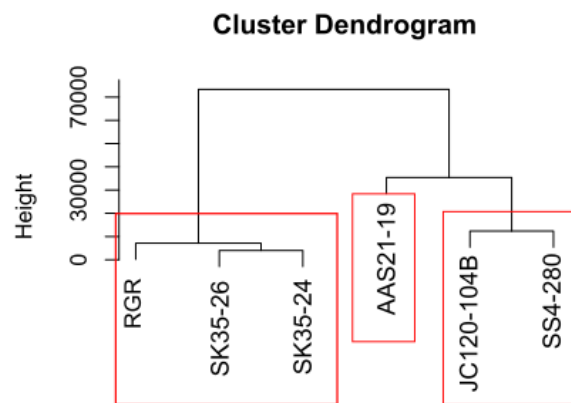


Figure 37 Hierarchical clustering of the nodules studied using the LA-ICP-MS data mean of chemical elements for each nodule.

Nodules from the CCZ fall into the mixed type category, according to the classification of Halbach et al., (1981). The discoidal shape and different surface texture on the top and bottom sides are in agreement with the model of growth by which diagenetic formation occurs in the buried side of the nodule, while hydrogenetic formation occurs at the exposed side. Besides, the thicker recent oxide layer corresponds to the rough side and the thinner to the smooth one. The diagenetic accretion process is known to happen at least one order of magnitude faster relative to hydrogenetic accretion (DYMOND et al., 1984), resulting in thicker layers in the buried side of nodules.

The chemical composition reflects some asymmetry between the top and the bottom side of the CCZ nodules too. It is possible to observe slight differences regarding the profiles of the Mn-Cu and Ti-REE pairs, which clearly vary in opposite ways in the bottom side of the nodule and are not observed in the top side.

Wegorzewski and Kuhn (2014) describe the Mn – Fe fractionation as a result of metals release due to the decomposition of organic matter within the sediments into the oxic pore water.

Ti and REE abundances occur with the same order of magnitude at both the top and the bottom side of the nodules from the CCZ, which can be explained by diffusion of the seawater into the first centimeters of sediment pore water. The metals released during Mn reduction in the suboxic layer, however, may not reach the seawater when migrating upward, or, if they do so, the dilution effect will be higher comparatively to the one expected for metals diffusing downward as the seawater penetrates into surficial sediment pore water. This mechanism explains why the Mn/Fe ratio variation occurs in the bottom side but not in the top side of the nodule exposed to seawater.

Thus, we can assume that the bottom side of the nodules- in contact with the sediment – undergoes metal precipitation under oxic diagenesis, while the top side – in contact with the seawater – is undergoes hydrogenetic metal precipitation, as illustrated by figure 38.

The overall geochemical composition of the CCZ nodules is characterized by higher Ni and Cu contents in comparison to Co and Ti, as well as a higher Mn content relative to Fe. Also, the REE concentration is < 500 ppm, much lower than the one in nodules from the MB and coated pebble from RGR. This geochemical fingerprint of nodules indicates a weak hydrogenetic component.

The existence of nodules with no apparent nucleus was reported by Halbach et al. (1981), for what they give the explanation that the internal part of these nodules is a former nodule functioning as adsorption surface for more recent concretions. They associate these occurrences to the mixed type nodules in which nuclei are predominately composed of broken fragments of old nodules, mainly nodule debris of hydrogenetic nodules, which seems to be the case for the nodules from the CCZ studied. However, the inner portion of the CCZ nodules is much more likely to result from diagenetic accretion, which can be deduced by both chemical and morphological aspects. In these layers, the Mn/Fe ratio varies from 3 to 40 but it is never < 1, Ni and Cu are highly abundant and bright, thick Mn-rich layers alternate with dendritic, Mn-poorer layers. Fragments of marine plankton are very common inside of the diagenetic massive layers and are not observed in the other layers, as also reported by Halbach et al. (1981).

In fact, the Mn/Fe ratio generally greater 10 (as high as 70) of the nodular nuclei from the CCZ nodules is characteristic of the suboxic diagenesis accretion described by Dymond et al. (1984). However, these authors associate the high Mn content to high flux of Mn^{2+} from organic matter regeneration within the sediment, so that Ni^{2+} and Cu^{2+} would not be incorporated into the Mn oxide structure, resulting in a low Ni and Cu content. This is not found in the study, because high Ni and Cu contents are associated to high Mn/Fe ratios. Still, the Mn specie prevailing is Mn^{4+} and Mn^{3+} and not Mn^{2+} . Therefore, oxic diagenesis is more likely to have occurred.

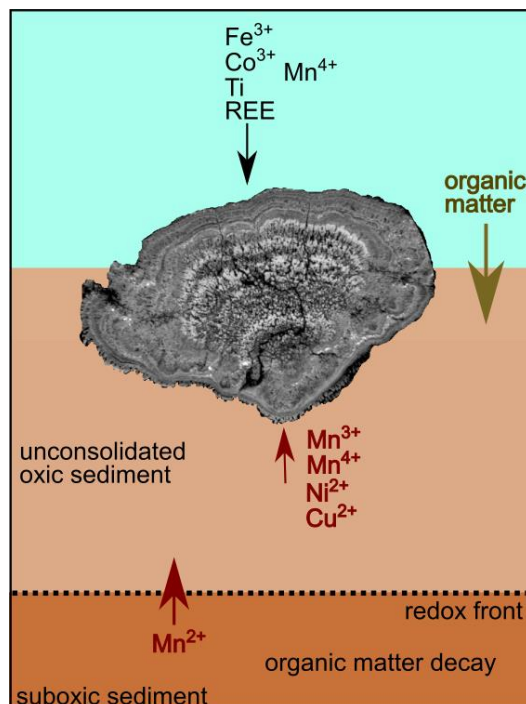


Figure 38 scheme of the mixed-type nodules from the Clarion-Clipperton Zone environment of formation.

The nodules from the CIB do not present the same external asymmetry observed for the nodules from CCZ. They are not discoidal, nor do they present a rim separating two different surface textures between exposed and buried sides.

Massive and dendritic layers are the main textures observed in the CIB nodules, which together with their spherical and spheroidal shapes and rough surface texture indicate a common diagenetic origin (HALBACH et al., 1981). Besides, Mn/Fe ratios > 5 and high Ni and Cu abundances relatively to Co and Ti confirm that they belong to the diagenetic type category (HALBACH et al., 1981). Still, the REE content in these nodules is < 500 ppm, low in comparison to the MB nodules and RGR coated pebble and close to the CCZ ones.

The strong alternation of layer textures and variable Mn/Fe ratio indicates high environmental variability. Similarly to the CCZ nodules, the Mn-rich layers are enriched in Ni and Cu, while the few layers where Mn/Fe is lower (< 5) are poorer in these two elements and a slight rise in Co and Ti is noticed. Layers like this second case may represent a period of time when the nodules were subject to more oxic conditions.

Hydrogenetic accretion is not likely to have occurred in the CIB nodules, since Mn/Fe ratios do not reach 1 in the oxide layer. Also, the columnar layer texture that is typical of this type of accretion (HALBACH et al., 1981) is not present. So the presence of low Mn/Fe layers is explained by exposure to oxic pore water rather than by direct exposure to seawater (hydrogenetic accretion), resulting on oxic-diagenetic precipitated Fe-rich Mn layers (DYMOND et al., 1984). The oxic pore water entrains metals from the seawater (Fe, Co, Ti, REE) but still contains high content of Mn cations because of the reaction with sediment particles (oxic diagenesis). In another stage of growth, however, this Mn flux from diagenesis was possibly higher, resulting in the high Mn/Fe, Ni and Cu, and in massive layers, as illustrated by figure 39. This seems to have happened more than once in all the studied nodules from the CIB.

Nevertheless, this process seems to have happened differently between the two nodules (AAS21-19 and SS4-280) because of their level of internal symmetry. Nodule AAS21-19 is asymmetric internally, while SS4-280 is highly symmetric. Nodule SS4-280 high symmetry indicates that despite the accretion process varied during the nodule growth, it happened in the same way and velocity all around the nodule. Much of the asymmetry of AAS21-19 can be explained by the presence of multiple nucleation centers.

This work suggests that the nodules from the CIB were formed buried within the first centimeters of oxic sediment where, moment of higher flux of metals from the seawater diffused to the pore water, alternated with moments when higher organic matter input released more diagenetic-sourced metals (figure 39).

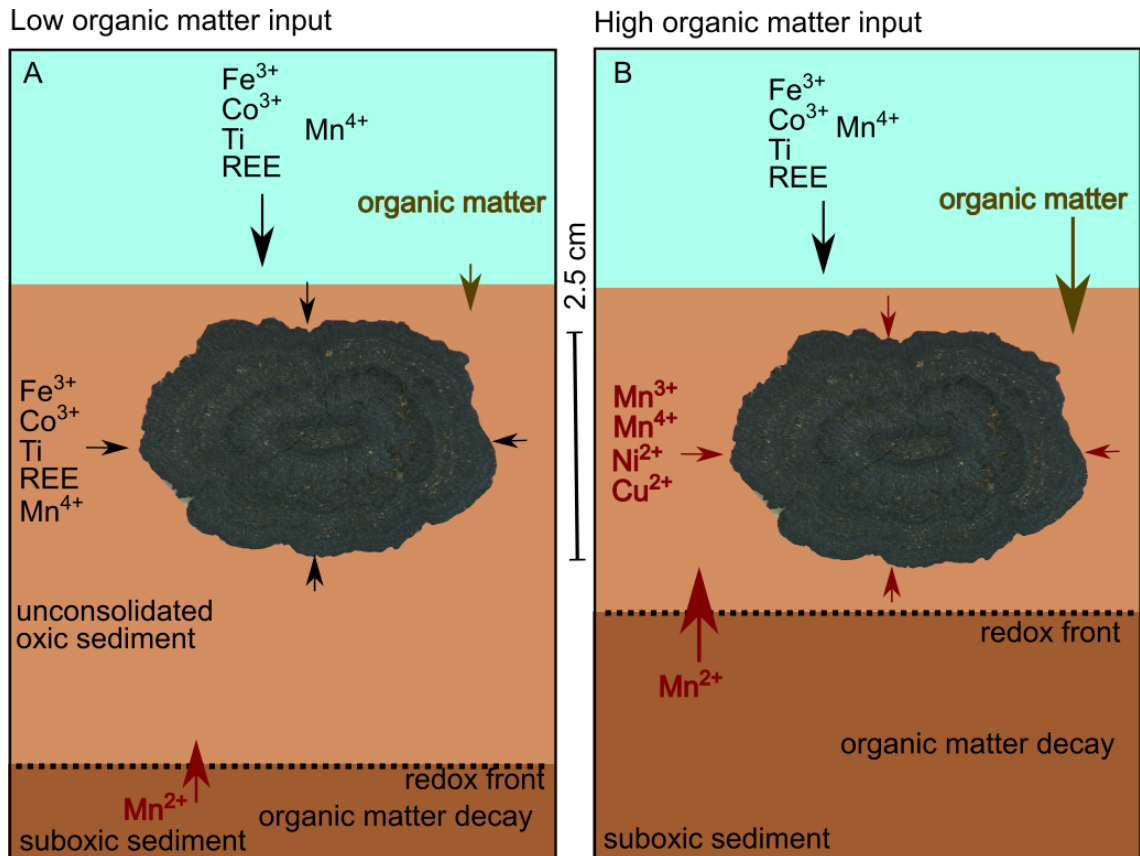


Figure 39 Condition of formation of oxic-diagenetic nodules from the Central Indian Basin conditions of formation. (A) in the case of low sedimentation of organic matter and (B) in the case of high sedimentation of organic matter.

The nodules from the Mascarene Basin are very different from the ones discussed until now. Their morphology is very consistent with those of the nodules ruled solely by hydrogenetic concretion described by Halbach et al. (1981).

Looking into the interior of the nodules, the microstructures also seem to be compatible with the Halbach et al. (1981) classification. The nodules from the MB, hydrogenetically formed, present regular and closely packed fabric with columnar patterns, which reflects the exterior surface causing the finely grained smooth texture. The variable degree of reflectiveness power is due to variable abundance of Mn in the hydrogenetic material.

The geochemical aspects of the nodules from the Mascarene Basin are very distinct from the CCZ and CIB. They are typical polynodules from slopes and seamounts vicinity (HEIN et al., 2015). The relative elemental composition also reflects the hydrogenetic formation, as the Fe content of these nodules is higher and the Mn/Fe is generally < 1. The low Ni and Cu content and higher Co and Ti content are in agreement with those expected for hydrogenetic accretion. Also, the Rare Earth

Elements content is > 1000 ppm, twice higher than the previous nodules. Despite the hydrogenetic signature of nodule SK35-24, its shape is not spheroidal because of its nucleus shape.

Nodules from the MB have been studied before by Nath and Prasad (1991), who also reported spheroidal 2 - 4 cm nodules with smooth surface texture, δ -MnO₂ dominant mineral, enriched in Fe, Co and REE and depleted in Mn, Ni and Cu. Two main mineral groups were found: (1) Ca, Fe, Mn, Co and Ti (hydrogenetic); and (2) Al, Si, K, Mg, Na and Cu (detrital) (NATH; PRASAD, 1991). Top-bottom fractionation was obliterated to what Nath et. al 1992 explained by the nodules turn-over. They observed more REE-enriched and δ -MnO₂-rich nodules in the western Indian Ocean and shallower depth in Central Indian Basin. They found strong correlation between Ca, Fe and REE and attributed the REE to be incorporated by the Fe oxyhydroxide phase. However, neither of the two studies investigated the chemical composition with spatial resolution as the present study does.

The high similarity all around the nodules indicates that the accretion did not vary much over the time, i.e. metal source and the rate of accretion. The fractionation between Mn-rich and Fe-rich layers does not occur in the MB nodules, or it occurs in such a small scale that it is not possible to identify. Their geochemical composition is more homogenous regarding all the chemical elements.

The small size may be related to their general lower growth rate in comparison to the other types, which explains also the low thickness of the internal layering. Their roundness is still little understood, as some authors hypothesize about a rolling movement because of bottom currents but no evidence exists that the bottom current would be able to move the nodules constantly. Also, the rolling movement would be expected to occur in the entire nodule accretion time in order to give those perfect concentric layers over the time. But from our observation, nodules attach together and this would have required an interval of no movement long enough to the attachment to happen (figure 40).

Nodules from red clay sediments have been found to be hydrogenetically in origin (PATTAN; PARTHIBAN, 2011). However, the shape of the nodules from the MB points to an exposed growth environmental set where they can eventually roll.

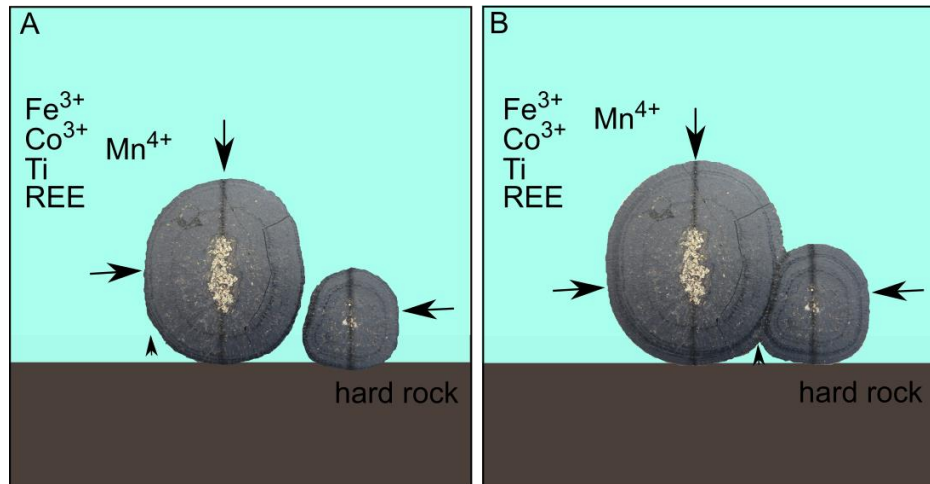


Figure 40 scheme of the hydrogenetic nodules from the Mascarene Basin environment of formation. (A) before and (B) after the nodules become attached.

Finally, the investigation of the coated pebble from the RGR, even though it is only one, reveals interesting facts about the environmental conditions from that region. Relying on its morphological and geochemical aspects it is possible to predict environmental conditions closer to the MB instead of the CCZ and the CIB for the RGR.

In fact, it has been mentioned above already that small and spheroidal smooth surface texture nodules are typical from slopes and seamounts vicinity and into the hydrogenetic genetic type. The abundance of well-preserved carbonate microfossils upon the nodules surface is a reliable hint that it is from a rise indeed, as carbonate shells would not be found well-preserved below the Carbonate Compensation Depth. The planktonic foraminiferal lysocline – the depth below which the tests began to suffer dissolution - is around 4050 m in the RGR (MELGUEN; THIEDE, 1974).

The RGR fits into the environmental set expected for this type of nodules. Besides, the sole nodule studied reflects a hydrogenetic ruled accretion type also geochemically. Its Mn/Fe ratio value is < 1 and the Ni and Cu abundance is low in comparison to Co and Ti. Also, the REE is the highest found among the nodules studied, being > 2800 ppm.

The morpho-geochemical fingerprint of the RGR coated pebble is compatible with what is expected to the environmental set, comparable to the figure 40. Besides, nodules from the Brazilian Basin and the western South Atlantic Ocean as whole have been showed to be dominantly hydrogenetic in comparison with the eastern South Atlantic and even the Walvis Ridge system, which is also a seamount (XAVIER, 1982; KASTEN et al., 1998).

The presence of highly contrasting layers with inverse correlation between Mn and Fe - as well as their companion elements Cu-Ni and Co-Ti-REE respectively - within the diagenetic and mixed type nodules from the CCZ and CIB in comparison to more homogenous layers with absent inverse correlations within the hydrogenetic Fe-Mn oxides from the MB and RGR is the important question.

It is suggested to be the result of the redox front close to the nodules location in the sediment. Slight changes in the redox front up or downward define the availability of metals for the nodules. Namely, it defines if exist a strong diffusion from the seawater to the sediment or if exist a strong influence of metals coming from enhanced organic matter diagenetic reaction in the suboxic layer. The redox front dictates the location of the main geochemical reactions within the sediments, mainly the ones responsible for the organic matter diagenesis.

The hydrogenetic Fe-Mn oxides from the MB and RGR, in the other hand, are entirely columnar and the inverse correlation between Mn and Fe is absent, as well as between the other elements. Variation of Cu solely occurs in the nodules from the MB, but it is not followed by Mn neither by Ti, which means that Cu varies for some other reason that is not the redox potential. This class of nodules form upon hard substrate entirely expose to the seawater in oxic environment. In this case there is no sediment pore water, thus no diagenetic reaction occurs.

As final consideration of the discussion section, this work reached its objectives. The nodules studied are in agreement with previous characterizations of the deposits already described (CCZ, CIB and MB). Also, further aspects were studied in this work adding to the previous description. A first characterization of a Fe-Mn oxides coated pebble from the RGR is presented.

The variable Mn/Fe ratio previously observed in the nodules from the CCZ was found to happen also in the CIB but not in the MB and RGR. This enables for a generalization that this process happens only in the diagenetic and mixed-type nodules and is not detected in the hydrogenetic nodules. Since both diagenetic and mixed-type nodules form at unconsolidated sediments basins, the presence of the redox front seems to play the major role in the existence of the fractionation process, whereas the redox front is not present in the environment of formation of the hydrogenetic nodules. Those nodules in which the Mn – Fe fractionation happens correspond to the ones with the most complex layer texture alternation (dendritic, massive and botryoidal), so the morphology is a good indicator of the nodules genesis.

7. CONCLUSIONS

The polymetallic nodules from the four ocean regions studied exhibit common characteristics and are formed fundamentally by the same two processes, the oxic diagenetic and the hydrogenetic accretion of Mn and Fe oxides. However, the nodules differ regarding which of these processes rule the growth processes, revealed by the morphological and geochemical. Polymetallic nodules from the Clarion-Clippertone Zone and the Central Indian Basin are dominantly formed by oxic diagenesis, whereas the ones from the Mascarene Basin and Rio Grande Rise are hydrogenetic.

Also, the accretion process was not constant during the nodule growth, as revealed by heterogeneous morphology and geochemistry of layers mainly in the diagenetic and mixed-type nodules. In these nodules, the Mn/Fe ratio is highly variable, as well as the metals which are associated to them. The redox front influences unconsolidated sediments, where this type of nodules form, and variances on its depth is suggested as the main responsible. Hydrogenetic nodules form over hard rock or oxic unconsolidated sediment and the metals come from the water column solely.

The morphology itself reflects the Mn and Fe fractionation and may be used as an indicative of the environment of nodule formation, whether within the sediment layer or exposed to seawater.

REFERENCES

- BANAKAR, V. K.; GUPTA, S. M.; PADMAVATHI, V. K. Abyssal Sediment Erosion in the Central Indian Basin: Evidence from Radiochemical and Radiolarian Studies. **Marine Geology**, v. 96, n. 1–2, p. 167–173, Jan. 1991.
- BANERJEE, R.; MIURA, H. Distribution Pattern and Morphochemical Relationships of Manganese Nodules from the Central Indian Basin. **Geo-Marine Letters**, v. 21, n. 1, p. 34–41, 2001.
- BATURIN, G. N. **The geochemistry of manganese and manganese nodules in the ocean**. Dordrecht: D. Reidel, 1988.
- BLÖTHE, M.; WEGORZEWSKI, A.; MÜLLER, C.; SIMON, F.; KUHN, T.; SCHIPPERS, A. Manganese-Cycling Microbial Communities Inside Deep-Sea Manganese Nodules. **Environmental Science & Technology**, v. 49, n. 13, p. 7692–7700, 7 Jul. 2015.
- BONATTI, E.; KRAEMER, T.; RYDELL, H. Classification and genesis of submarine iron-manganese deposits. In: HORN, D. R. (Ed.). **Ferromanganese Deposits on the Ocean Floor**. Washington D.C.: NSF, 1972. p. 149–166.
- BURNS, R. G.; BURNS, V. M. The Mineralogy and Crystal Chemistry of Deep-Sea Manganese Nodules, a Polymetallic Resource of the Twenty-First Century. **Philosophical Transactions, Royal Society of London**, v. 286, p. 283–301, 1977.
- CRONAN, D. S. Deep-sea nodules: distribution and geochemistry. In: GLASBY, G. P. (Ed.). **Marine Manganese Deposits**. Amsterdam: Elsevier, 1977. p. 11–44.
- CRONAN, D. S. Manganese Nodules: Controversy upon Controversy. **Endeavour**, v. 2, n. 2, p. 80–84, 1978.
- CRONAN, D. S.; TOOMS, J. S. The Geochemistry of Manganese Nodules and Associated Pelagic Deposits from the Pacific and Indian Oceans. **Deep Sea Research and Oceanographic Abstracts**, v. 16, n. 4, p. 335–359, 1969.
- DUBININ, A. V.; RIMSKAYA-KORSAKOVA, M. N. Geochemistry of Rare Earth Elements in Bottom Sediments of the Brazil Basin, Atlantic Ocean. **Lithology and Mineral Resources**, v. 46, n. 1, p. 1–16, 2011.
- DYMOND, J.; LYLE, M.; FINNEY, B.; PIPER, D. Z.; MURPHY, K.; CONARD, R.; PISIAS, N. Ferromanganese Nodules from MANOP Sites H, S, and R-Control of Mineralogical and Chemical Composition by Multiple Accretionary Processes.

Geochimica et Cosmochimica Acta, v. 48, p. 931–949, 1984.

EMELYANOV, E. M. Bottom Sediments and near-Bottom Currents in the Southwestern Atlantic. **Russian Geology and Geophysics**, v. 56, p. 996–1015, 2015.

FLORINDO, F.; GENNARI, R.; PERSICO, D.; TURCO, E.; VILLA, G.; LURCOCK, P. C.; ROBERTS, A. P.; WINKLER, A.; CARTER, L.; PEKAR, S. F. New Magnetobiostratigraphic Chronology and Paleoceanography Changes across the Oligocene-Miocene Boundary at DSDP Site 516 (Rio Grande Rise, SW Atlantic). **Paleoceanography**, v. 30, p. 659–681, 2015.

GLASBY, G. P. **Marine manganese deposits**. Amsterdam: Elsevier, 1977.

GLASBY, G. P. Deep Seabed Mining: Past Failures and Future Prospects. **Marine Georesources & Geotechnology**, v. 20, p. 161–176, 2002.

GLASBY, G. P. Manganese: Predominant Role of Nodules and Crusts. **Marine Geochemistry**, p. 371–427, 2006.

GLASBY, G. P.; LI, J.; SUN, Z. Deep-Sea Nodules and Co-Rich Mn Crusts. **Marine Georesources & Geotechnology**, v. 33, n. 1, p. 72–78, 2013.

GONZÁLEZ, F. J.; SOMOZA, L.; LUNAR, R.; MARTÍNEZ-FRÍAS, J.; RUBÍ, J. A. M.; TORRES, T. Internal Features, Mineralogy and Geochemistry of Ferromanganese Nodules from the Gulf of Cadiz: The Role of the Mediterranean Out Flow Water Undercurrent. **Journal of Marine Systems**, v. 80, n. 3–4, p. 203–218, 2010.

HALBACH, P. Processes Controlling the Heavy Metal Distribution in Pacific Ferromanganese Nodules and Crusts. **Geologische Rundschau**, v. 75, n. 1, p. 235–247, Feb. 1986.

HALBACH, P.; MARCHIG, V.; SCHERHAG, C. Regional Variations in Mn, Ni, Cu and Co of Ferromanganese Nodules from a Basin in the Southeast Pacific. **Marine Geology**, v. 38, n. 4, p. 1–9, 1980.

HALBACH, P.; SCHERHAG, C.; HEBISCH, U.; MARCHIG, V. Geochemical and Mineralogical Control of Different Genetic Types of Deep-Sea Nodules from the Pacific Ocean. **Mineralium Deposita**, v. 16, n. 1, p. 59–84, 1981.

HEIN, J. R.; KOSCHINSKY, A. Deep-Ocean Ferromanganese Crusts and Nodules. In: SCOTT, S. (Ed.). **Treatise on Geochemistry**. 2. ed. Amsterdam: Elsevier, 2014. p. 273–291.

HEIN, J. R.; KOSCHINSKY, A.; HALBACH, P.; MANHEIM, F. T.; BAU, M.; KANG, J.; LUBICK, N. Iron and Manganese Oxide Mineralization in the Pacific. **Manganese**

Mineralisation: Geochemistry and Mineralogy of Terrestrial and Marine Deposits, v. 119, p. 123–138, 1997.

HEIN, J. R.; MIZELL, K.; KOSCHINSKY, A.; CONRAD, T. A. Deep-Ocean Mineral Deposits as a Source of Critical Metals for High- and Green-Technology Applications: Comparison with Land-Based Resources. **Ore Geology Reviews**, v. 51, p. 1–14, 2013.

HEIN, J. R.; PETERSEN, S. The Geology of Manganese Nodules. In: BAKER, E.; BEAUDOIN, Y. (Ed.). **Manganese Nodules: A physical, biological, environmental, and technical review**. [s.l.] Secretariat of the Pacific Community, 2013. p. 7–18.

HEIN, J. R.; SPINARDI, F.; OKAMOTO, N.; MIZELL, K. Critical Metals in Manganese Nodules from the Cook Islands EEZ, Abundances and Distributions. **Ore Geology Reviews**, v. 68, p. 97–116, 2015.

INTERNATIONAL SEABED AUTHORITY (ISA). **A geological model of polymetallic nodule deposits in the Clarion Clipperton Fracture Zone**: ISA technical Studies. Kingston, Jamaica, 2010. .

JOHNSON, D. A. Eastward-Flowing Bottom Currents along the Clipperton Fracture Zone. **Deep Sea Research and Oceanographic Abstracts**, v. 19, n. 3, p. 253–257, Mar. 1972.

KASTEN, S.; GLASBY, G. .; SCHULZ, H. .; FRIEDRICH, G.; ANDREEV, S. . Rare Earth Elements in Manganese Nodules from the South Atlantic Ocean as Indicators of Oceanic Bottom Water Flow. **Marine Geology**, v. 146, n. 1–4, p. 33–52, Apr. 1998.

LU, B.; GUO, H.; LI, P.; LIU, H.; WEI, Y.; HOU, D. Comparison Study on Transformation of Iron Oxyhydroxides: Based on Theoretical and Experimental Data. **Journal of Solid State Chemistry**, v. 184, n. 8, p. 2139–2144, 2011.

MARCUS, M.; EDWARDS, K.; GUEGUEN, B.; FAKRA, S.; HORN, G.; JELINSKI, N.; ROUXEL, O.; SORENSEN, J.; TONER, B. Iron Mineral Structure, Reactivity, and Isotopic Composition in a South Pacific Gyre Ferromanganese Nodule over 4 Ma. **Geochimica et Cosmochimica Acta**, v. 171, p. 61–79, 2015.

MAYUMY AMPARO, C.-R.; ARTURO, C.; MARLENE, O.; REZ MAYUMY AMPARO, C.; ARTURO, C.; MARLENE, O. Marine Georesources & Geotechnology Morphology and Texture of Polymetallic Nodules and Their Association with Sediments of the Mexican Pacific Morphology and Texture of Polymetallic Nodules and Their

- Association with Sediments of the Mexican Pacific. **Marine Georesources & Geotechnology**, v. 31, n. 2, p. 154–175, 2013.
- MELGUEN, M.; THIEDE, J. Facies Distribution and Dissolution Depths of Surface Sediment Components from the Vema Channel and the Rio Grande Rise (Southwest Atlantic Ocean). **Marine Geology**, v. 17, n. 5, p. 341–353, 1974.
- MEWES, K.; MOGOLLÓN, J. M.; PICARD, A.; RÜHLEMANN, C.; KUHN, T.; NOTHEN, K.; KASTEN, S. Impact of Depositional and Biogeochemical Processes on Small Scale Variations in Nodule Abundance in the Clarion-Clipperton Fracture Zone. **Deep-Sea Research Part I**, v. 91, p. 125–141, 2014.
- MILLIMAN, J. D.; AMARAL, C. A. B. Economic Potential of Brazilian Continental Margin Sediments. **Anais do Congresso Brasileiro de Geologia**, v. 28, p. 335–344, 1974.
- MURRAY, J.; IRVINE, R. XXXII.—On the Manganese Oxides and Manganese Nodules in Marine Deposits. **Earth and Environmental Science Transactions of the Royal Society of Edinburgh**, v. 37, n. 4, p. 721–742, 1895.
- NATH, B. N.; PRASAD, M. S. Manganese Nodules in the Exclusive Economic Zone of Mauritius. **Marine Mining**, v. 10, p. 303–355, 1991.
- PATTAN, J. N.; PARTHIBAN, G. Geochemistry of Ferromanganese Nodule-Sediment Pairs from Central Indian Ocean Basin. **Journal of Asian Earth Sciences**, v. 40, n. 2, p. 569–580, 2011.
- PUTEANUS, D.; HALBACH, P. Correlation of Co Concentration and Growth Rate--A Method for Age Determination of Ferromanganese Crusts. **Chemical Geology**, v. 69, n. 1–2, p. 73–85, 1988.
- RÜHLEMANN, C.; KUHN, T.; WIEDICKE, M.; KASTEN, S.; MEWES, K.; PICARD, A. Current status of manganese nodule exploration in the German license area. In: ISOPE OCEAN MINING SYMPOSIUM, Maui, HI; United States. **Anais...** Maui, HI; United States: International Society of Offshore and Polar Engineers, 2011.
- SHIRAIISHI, F.; MITSUNOBU, S.; SUZUKI, K.; HOSHINO, T. Dense Microbial Community on a Ferromanganese Nodule from the Ultra-Oligotrophic South Pacific Gyre: Implications for Biogeochemical Cycles. **Earth and Planetary Science Letters**, v. 447, p. 10–20, 2016.
- STRAMMA, L.; JOHNSON, G. C.; SPRINTALL, J.; MOHRHOLZ, V. Expanding Oxygen-Minimum Zones in the Tropical Oceans. **Science**, v. 320, p. 655–659, 2008.
- VALSANGKAR, A. B.; REBELLO, J. M. S. Significance of Size in Occurrence,

- Distribution, Morphological Characteristics, Abundance, and Resource Evaluation of Polymetallic Nodules. **Marine Georesources & Geotechnology**, v. 33, p. 135–149, 2015.
- VERLAAN, P. A.; CRONAN, D. S.; MORGAN, C. L. A Comparative Analysis of Compositional Variations in and between Marine Ferromanganese Nodules and Crusts in the South Pacific and Their Environmental Controls. **Progress in Oceanography**, v. 63, p. 125–158, 2004.
- VINEESH, T.; NAGENDER NATH, B.; BANERJEE, R.; JAISANKAR, S.; LEKSHMI, V. Manganese Nodule Morphology as Indicators for Oceanic Processes in the Central Indian Basin. **International Geology Review**, v. 51, n. 1, p. 27–44, 2009.
- WANG, X.; GAN, L.; MÜLLER, W. E. G. Contribution of Biomineralization during Growth of Polymetallic Nodules and Ferromanganese Crusts from the Pacific Ocean. **Frontiers of Materials Science in China**, v. 3, n. 2, p. 109–123, 2009.
- WANG, X.; SCHLOSSMACHER, U.; WIENS, M.; SCHRÖDER, H. C.; MÜLLER, W. E. G. Biogenic Origin of Polymetallic Nodules from the Clarion-Clipperton Zone in the Eastern Pacific Ocean: Electron Microscopic and EDX Evidence. **Marine biotechnology (New York, N.Y.)**, v. 11, n. 1, p. 99–108, 2009.
- WEGORZEWSKI, A. V.; KUHN, T. The Influence of Suboxic Diagenesis on the Formation of Manganese Nodules in the Clarion Clipperton Nodule Belt of the Pacific Ocean. **Marine Geology**, v. 357, p. 123–138, 2014.
- XAVIER, A. Ferromanganese Deposits off Northeast Brazil (S. Atlantic). **Marine Geology**, v. 47, p. 87–99, 1982.
- ZHENG, Y.; VAN GEEN, A.; ANDERSON, R. F.; GARDNER, J. V.; DEAN, W. E. Intensification of the Northeast Pacific Oxygen Minimum Zone during the Bolling-Allerod Warm Period. **Paleoceanography**, v. 15, n. 5, p. 528–536, 2000.

APPENDIX A – Tables of LA-ICP-MS average concentration values of chemical elements in the polymetallic nodules.

Table 1 Polymetallic nodule JC120-104B.

LA-ICP-MS	n=124	Mean	Std deviation
Mn	%	42.68	19.23
Si	%	5.00	2.79
Ca	%	1.58	0.75
K	%	1.31	0.46
Ni	ppm	12298.91	7654.93
Cu	Ppm	11658.03	6731.24
Zn	ppm	3578.35	2687.49
Ti	ppm	2542.80	2599.83
Ba	ppm	2284.79	1329.72
Co	ppm	1395.26	1693.19
Mo	ppm	991.51	521.37
V	ppm	622.31	383.53
Sr	ppm	595.47	405.06
REY	ppm	521.39	473.70
Pb	ppm	315.78	473.21
Ce	ppm	289.55	372.47
Zr	ppm	287.53	352.11
Nd	ppm	145.09	132.05
La	ppm	115.60	116.23
Y	ppm	82.67	71.10
Sm	ppm	35.76	30.98
Pr	ppm	34.68	32.48
Gd	ppm	31.20	27.04
Dy	ppm	28.17	24.80
Nb	ppm	17.23	19.70
Cr	ppm	17.20	7.79
Er	ppm	13.68	11.98
Yb	ppm	13.03	11.40
Th	ppm	12.79	15.51
Sc	ppm	11.19	5.83
Eu	ppm	8.11	7.23
U	ppm	5.42	4.81
Tb	ppm	4.54	3.98
Ho	ppm	4.99	4.39
Hf	ppm	3.86	4.95
Cs	ppm	2.27	1.31
Tm	ppm	1.94	1.70
Lu	ppm	1.94	1.70

Ta	ppm	0.30	0.20
Pt	ppm	0.08	0.07

Table 2 Polymetallic nodule AAS21-19.

LA-ICP-MS	n=96	Mean	Std deviation
Mn	%	65.54	52.26
Si	%	18.10	12.10
Ca	%	3.51	2.39
K	%	2.72	1.97
Cu	Ppm	40727.01	35631.09
Ni	Ppm	32304.39	28942.97
Ti	Ppm	5425.02	3328.09
Zn	Ppm	3295.12	2800.07
Ba	Ppm	3232.63	2596.03
Co	Ppm	2722.16	1892.99
Pb	Ppm	2319.20	1787.02
Sr	Ppm	1466.40	1058.30
Mo	Ppm	1260.42	1111.98
REY	Ppm	1105.55	800.81
Ce	Ppm	896.85	654.37
Zr	Ppm	796.22	582.17
V	Ppm	770.22	544.08
Nd	Ppm	302.29	218.64
La	Ppm	258.50	189.54
Y	Ppm	180.22	132.47
Pr	Ppm	68.33	49.46
Sm	Ppm	73.31	52.88
Gd	Ppm	63.79	46.87
Dy	Ppm	59.37	43.15
Th	Ppm	50.15	37.93
Nb	Ppm	40.74	26.19
Sc	Ppm	31.97	18.74
Cr	Ppm	30.15	13.92
Er	Ppm	28.57	20.77
Yb	Ppm	27.16	19.80
Eu	Ppm	16.76	12.17
Hf	Ppm	12.94	9.30
Ho	Ppm	10.16	7.38
Tb	Ppm	9.43	6.85
U	Ppm	8.27	6.02
Tm	Ppm	3.86	2.81
Lu	Ppm	3.79	2.78
Cs	Ppm	2.28	1.49

Ta	Ppm	0.75	0.44
Pt	Ppm	0.49	0.43

Table 3 Polymetallic nodule SS4-280.

LA-ICP-MS	n=102	Mean	Std deviation
Mn	%	38.20	16.50
Si	%	6.14	3.57
Ca	%	1.84	0.67
K	%	1.10	0.29
Sc	Ppm	11.60	5.60
Cu	Ppm	22839.21	11124.88
Ni	Ppm	17314.70	8631.43
Zn	Ppm	2490.52	1334.74
Ti	Ppm	2155.31	1301.48
Ba	Ppm	1900.20	990.47
Co	Ppm	1248.95	519.33
Pb	Ppm	828.64	496.62
Mo	Ppm	777.53	421.30
Sr	Ppm	652.15	265.60
REY	Ppm	476.93	240.48
V	Ppm	439.50	198.28
Ce	Ppm	404.94	233.60
Zr	Ppm	293.23	161.24
Nd	Ppm	132.31	67.57
La	Ppm	107.51	56.38
Y	Ppm	74.18	36.39
Pr	Ppm	33.79	17.60
Sm	Ppm	33.17	16.29
Th	Ppm	27.76	20.19
Gd	Ppm	26.88	13.25
Dy	Ppm	25.74	12.68
Nb	Ppm	18.67	8.14
Cr	Ppm	12.48	3.53
Er	Ppm	12.13	5.90
Yb	Ppm	11.55	5.54
Eu	Ppm	7.55	3.85
Hf	Ppm	4.56	2.69
U	Ppm	4.52	2.56
Ho	Ppm	4.42	2.16
Tb	Ppm	4.21	2.06
Tm	Ppm	1.78	0.85
Lu	Ppm	1.72	0.83

Cs	Ppm	0.96	0.37
Ta	Ppm	0.30	0.16
Pt	Ppm	0.20	0.13

Table 4 Polymetallic nodule SK35-24.

LA-ICP-MS	n=68	Mean	Std deviation
Si	%	31.85	15.20
Mn	%	30.80	39.22
Ca	%	3.75	3.65
K	%	3.44	2.38
Ti	ppm	21512.13	19932.88
Co	ppm	6419.20	8718.44
Ni	ppm	4419.80	5162.82
Ce	ppm	3394.87	4160.74
Pb	ppm	2876.34	3693.57
Cu	ppm	2670.02	2288.27
Sr	ppm	2206.23	2761.69
Ba	ppm	2143.27	2559.07
REY	ppm	1502.35	1659.14
Zr	ppm	1312.33	1218.06
Zn	ppm	1291.40	1372.80
V	ppm	981.47	1127.27
Mo	ppm	470.01	608.31
La	ppm	404.17	458.10
Nd	ppm	388.07	433.44
Y	ppm	274.73	307.96
Nb	ppm	139.01	124.89
Th	ppm	112.97	121.92
Pr	ppm	89.63	100.40
Sm	ppm	86.41	96.06
Cr	ppm	75.92	32.79
Dy	ppm	72.87	80.76
Gd	ppm	63.00	70.13
Sc	ppm	47.45	17.79
Er	ppm	36.74	40.56
Yb	ppm	33.86	37.54
Hf	ppm	25.75	17.67
Eu	ppm	19.21	21.54
U	ppm	15.94	19.15
Tb	ppm	11.17	12.38
Ho	ppm	12.87	14.22
Tm	ppm	4.86	5.37

Lu	ppm	4.76	5.26
Ta	ppm	4.04	2.52
Cs	ppm	2.19	1.37
Pt	ppm	0.26	0.32

Table 5 Polymetallic nodule SK35-26.

LA-ICP-MS	n=126	Mean	Std deviation
Mn	%	19.01	13.67
Si	%	10.06	2.98
Ca	%	2.62	1.30
K	%	1.03	0.45
Ti	Ppm	19826.22	14383.95
Co	Ppm	3883.38	3274.52
Ni	Ppm	3021.61	2247.80
Ce	Ppm	2407.49	1775.41
Ba	Ppm	1797.03	1226.86
Pb	Ppm	1650.08	1100.68
Cu	Ppm	1620.15	958.89
Sr	Ppm	1449.22	919.17
REY	Ppm	1129.66	766.13
Zn	Ppm	945.59	562.84
Zr	Ppm	920.81	463.27
V	Ppm	599.96	355.56
La	Ppm	307.57	210.07
Nd	Ppm	294.64	203.09
Mo	Ppm	277.09	228.02
Y	Ppm	188.70	124.20
Nb	Ppm	128.01	75.20
Th	Ppm	87.05	62.72
Pr	Ppm	75.17	52.17
Sm	Ppm	64.33	43.86
Dy	Ppm	55.81	37.58
Gd	Ppm	46.25	30.95
Cr	Ppm	31.54	31.12
Er	Ppm	28.76	19.36
Yb	Ppm	27.10	18.50
Sc	Ppm	20.70	6.40
Hf	Ppm	18.97	10.02
Eu	Ppm	14.38	9.78
U	Ppm	14.07	9.40
Ho	Ppm	10.02	6.74
Tb	Ppm	8.53	5.75

Tm	Ppm	4.21	2.85
Lu	Ppm	4.19	2.86
Ta	Ppm	3.95	3.17
Cs	Ppm	0.56	0.54
Pt	Ppm	0.19	0.15

Table 6 Polymetallic coated pebble RGR.

LA-ICP-MS	n=24	Mean	Std deviation
Ca	%	42.68	41.56
Mn	%	18.96	24.45
Si	%	13.66	7.56
K	%	2.19	1.56
Ti	ppm	15345.92	15817.27
Co	ppm	7054.63	8710.10
Ni	ppm	4394.14	5896.10
REY	ppm	2894.46	1592.26
Sr	ppm	2873.40	1289.27
Ce	ppm	2034.59	2278.72
Pb	ppm	1883.81	2429.32
Cu	ppm	1449.62	1420.84
Ba	ppm	1233.10	1335.40
Zn	ppm	1091.54	1149.51
V	ppm	1069.37	1256.88
Y	ppm	808.85	514.48
La	ppm	772.67	397.32
Zr	ppm	715.37	727.54
Nd	ppm	612.64	354.33
Mo	ppm	303.23	424.03
Pr	ppm	141.98	85.38
Nb	ppm	139.91	150.87
Gd	ppm	120.70	72.17
Sm	ppm	120.22	71.47
Dy	ppm	114.65	56.10
Th	ppm	74.54	77.25
Er	ppm	64.93	29.49
Yb	ppm	54.03	22.96
Cr	ppm	49.93	51.97
Sc	ppm	45.81	14.77
Eu	ppm	28.99	18.00
Ho	ppm	22.30	10.58
U	ppm	17.16	11.20
Tb	ppm	16.61	8.51

Hf	ppm	16.55	17.44
Tm	ppm	8.11	3.52
Lu	ppm	7.79	3.23
Cs	ppm	2.87	1.50
Ta	ppm	1.68	1.64
Pt	ppm	0.44	0.46
